DISSERTATION

METAL OXIDES AS BUFFER LAYERS IN POLYCRYSTALLINE CdTe THIN-FILM SOLAR CELLS

Submitted by

Ramesh Pandey

Department of Physics

In partial fulfillment of the requirements

For the Degree of Doctor of Philosophy

Colorado State University

Fort Collins, Colorado

Fall 2021

Doctoral Committee:

Advisor: James Sites

W. S. Sampath
Kate Ross
John Harton

ABSTRACT

METAL OXIDES AS BUFFER LAYERS IN POLYCRYSTALLINE CdTe THIN-FILM SOLAR CELLS

The optical band-gap of 1.5 eV and absorption coefficient the order of 10^5 cm^{-1} makes CdTe a very attractive absorber for thin-film solar cells. This dissertation explores methods to improve both the front, or emitter, part of the cell and the back contact to the CdTe-based thin-film solar cells.

The choice of an n-type emitter partner for CdTe based solar cells is crucial to the overall power conversion efficiency. In comparison to the traditional CdS emitter, metal oxides such as ZnO, MgO, and the ternary alloy $Mg_xZn_{1-x}O$ have large optical band-gaps making them transparent to most of the solar spectrum and an ideal emitter layer adjacent to light-facing side of the absorber in a superstrate configuration. The optical and electrical properties of $Mg_xZn_{1-x}O$ emitters can be modulated by varying the elemental ratio of x = Mg:(Mg + Zn) in the ternary alloy. Tracing the variation of the conversion efficiency as a function of Mg fraction in $Mg_xZn_{1-x}O$ emitter, an optimal Mg fraction of x = 0.15 was found to produce highest efficiency for the CdTe-based thin-film solar cells. Photoelectron spectroscopy demonstrated the conduction band offset at the emitter/absorber interface transitions from a cliff like -0.1 eV for x = 0.00 to a spike like 0.2 eV at the optimal x = 0.15. Photoluminescence and low-temperature current-voltage measurements showed that the interface between MgZnO and the CdSeTe is well passivated for x =0.15. Further increase in the Mg fraction however increases the band offset between the emitter/absorber leading to distortions of J-V curves under various illumination conditions. Light soaking experiments and numerical simulations show that an insufficient density of carriers in the MgZnO due to the compensating defects causes these distortions: a failure of superposition of light and dark curves referred to as cross over, and distortion from normal current voltage behavior under spectra filtered illumination. An extrinsic doping of the emitter is critical to rectify

these distortions and Ga-doped MgZnO was employed to experimentally demonstrate a cure to these J-V distortions characteristic of an undoped MgZnO emitter. It paves pathway to increase the n-type carrier density in the MgZnO emitter. The group-V doping of CdTe has shown potential to improve open circuit voltage, with level of doping in absorber the order of 10^{16} cm^{-3} and lifetimes of hundreds of ns. Numerical device simulations demonstrate that doping the emitter layer is essential and a particular challenge if the doping in the absorber is high. The results find the carrier concentration in emitter should be higher than the doping in the absorber to attain high open-circuit voltage in the highly doped CdTe-absorbers possible with arsenic doping.

Various back contact metals like Ag, Co, Pt and metalloids like Te, and Se with different work functions were used to make an ohmic contact with the CdTe back surface. The use of a buffer layer behind the bare CdTe surface is found to be critical to the device performance. A thin 30-nm layer of Te have become the preferred choice of back buffer layer. Metal oxides like TeO_x has been introduced as back buffer between the CdTe absorber and Te back contact to study their effect in device performance. The study finds that a double $CdCl_2$ passivation procedure before and after the deposition of oxides is critical to the performance of these solar cells. Devices with the TeO_x and the Te layer as back buffer demonstrated a power conversion efficiency in excess of 17 % without the incorporation of dopant in the absorber. Such a result is significant, as extrinsic dopants in CdTe-based absorbers often introduce defects in the absorber leading to increased recombination and degradation of cell performance particularly if the absorber is doped with Cu. Spectral and time resolved photoluminescence measurements carried out with illumination from front glass side show such cells have improved minority carrier lifetimes. The rear TRPL illumination to probe a $CdTe/TeO_x$ surface measured lifetimes of few ns indicative of the TeO_x as a back buffer layer to mitigate the effects of large defects on a free CdTe surface. These results demonstrate metal oxides as a promising candidates for back buffer layers, and passivating back contact for hole selectivity in the CdTe-based solar cells.

ACKNOWLEDGMENTS

I acknowledge the patience, trust and guidance of Prof. James R. Sites, which made the work presented in this dissertation possible. His mentorship instilled the confidence in me to think critically, to analyze, and correlate the results from different experiments to deduce meaningful conclusions. I learned to communicate and present my results, ideas and discussions in effective ways, both in verbal and written form.

I express my sincere respect and gratefulness towards my mother Basanta Kumari Thapa, father Om Bahadur Pandey, and my sister Dr. Rosheela Pandey for their unparalleled love, support and inspiration that has been instrumental in my journey. Without your patience, encouragement and guidance I would not be who I am today.

I would like to thank my seniors Jen Drayton, John Raguse, Andrew Moore and Tao Song for guiding me and teaching me the techniques of device characterization and numerical simulations during the early years of my graduate school. I am in debt to Prof. Walajabad Sampath and his lab members Amit Munshi, Jason Kephart, Tushar Shimpi and Kevan Cameroon for providing a wonderful opportunity to work in a device fabrication laboratory that gave me a hands on experience of the semiconductor deposition via various deposition techniques, various vacuum systems and deposition tools. I will remember the fruitful discussion, constructive criticism, and valuable inputs from my friends Alexandra Bothwell, Pascal Jundt, Akash Shah, Anthony Nicholson, Carey Reich and Adam Danielson.

I am grateful to my brother-in-law Sujan Kandel for his friendship, support and encouragement. Lastly, I am in debt forever to my loving wife Sajani Kandel for sharing my beliefs and being there for me, during my highs and lows.

TABLE OF CONTENTS

ABSTRACT. ii

ACKNOWLEDGMENTS iv

LIST OF TABLES vii

LIST OF FIGURES viii

LIST OF SYMBOLS xiii

1 Introduction 1
1.1 Need for a clean source of energy 1
1.2 Solar energy 3

2 Background 4
2.1 Fundamentals of semiconductors 4
2.2 Fermi level and carrier density 5
2.3 Generation and recombination 7
2.4 P-N junction 10
2.5 CdTe thin-film solar cell 12
2.6 Numerical Simulations 16

3 Semiconductor Heterojunctions and Metal oxides as buffer for polycrystalline CdTe thin-film solar cells 19
3.1 Simple band alignment 19
3.2 Band bending at heterojunctions 20
3.3 Metal-Semiconductor contact 21
3.4 Metal-Insulator-Semiconductor structures 24

4 MgZnO as emitter for polycrystalline CdTe thin-film solar cells. 27
4.1 Choice of metal oxide as emitter 27
4.2 Optical band-gap engineering 29
4.2.1 Alloying of CdTe with Se 30
4.2.2 Alloying of MgO and ZnO to form $Mg_xZn_{1-x}O$ emitter 31
4.3 CdTe-based solar cells with $Mg_xZn_{1-x}O$ emitter 34
4.3.1 J-V and QE measurement for $Mg_xZn_{1-x}O$ emitters 35
4.3.2 Energy band-offset between emitter and absorber 37
4.3.3 Energy band bending and Interface passivation 41
4.4 J-V distortion in CdTe solar cells with $Mg_xZn_{1-x}O$ emitter 45
4.4.1 Effect of Mg fraction on J-V distortion 45
4.4.2 Cause of J-V distortion 49
4.4.3 Remedy for J-V distortions by Ga-doping of MgZnO 52
4.5 Emitter doping 56
4.5.1 Emitter and absorber carrier densities 57

4.5.2 Advantage of doping the emitter for highly doped absorbers 60
4.5.3 Mitigation of large S_{IF} 62
4.6 Summary 64

5 Alternative back contact approaches for polycrystalline CdTe thin-film solar cells 66
5.1 Background 67
5.2 CdTe-metal back contact with varied metal work function 68
5.3 Te as a buffer layer between CdTe and metal electrode 71
5.4 TeO_x as a back buffer and surface passivation oxide 74
5.4.1 TeO_x thickness, and sequence of $CdCl_2$ treatment 75
5.4.2 Effect of Oxygen during the TeO_x deposition 79
5.5 Se/ITO transparent back contact 82
5.6 Metal-oxide buffer layers 83
5.7 Summary 86

6 Conclusions and Discussion 88

Bibliography 94

List of Publications 105

List of Abbreviations 107

LIST OF TABLES

2.1 Critical parameters used for the numerical simulation using SCAPS-1D 18

4.1 J-V parameters for various emitters for CdTe-based TFSCs in Fig 4.2 28

4.2 J-V parameters of progressively improved devices from Fig 4.3 30

4.3 Critical parameters for linear fitting for Tauc plot in Fig. 4.4, calculated inter planar spacing and the lattice paramerers for XRD measurements from Fig. 4.5 . 34

4.4 J-V parameters of best devices with varying Mg fraction shown in Fig 4.6 34

4.5 Average J-V parameters and standard deviation of 25 devices with varying 'x'. . 36

4.6 ΔE_C between $Mg_xZn_{1-x}O$/CdSeTe for varied 'x' , and ratio of ΔE_C to ΔE_V in $Mg_xZn_{1-x}O$. 40

4.7 J-V parameters for CdTe-based solar cells in Fig. 4.16 measured under various illumination conditions. 47

4.8 J-V parameters for experimentally measured and simulated CdTe-based solar cells under various illumination conditions.. 50

5.1 Description of various back contacts for CdTe absorber 66

5.2 J-V parameters, depletion width (W_D) at 0 V and net carrier concentration (N_A) at bottom of belly from C-V measurement from Fig. 5.4(c) 71

5.3 J-V parameters, depletion width (W_D) at 0 V and net carrier concentration (N_A) at bottom of belly from C-V measurement from Fig. 5.7(c) 73

5.4 J-V parameters for varied TeO_x thickness and $CdCl_2$ sequence from Fig. 5.8 . . . 76

5.5 J-V parameters for best devices from Fig. 5.12. 80

5.6 C-V parameters for TeO_x deposited in different ambiance from 5.13(c)-(d). 82

5.7 J-V parameters for best devices from Fig. 5.15(b). 84

LIST OF FIGURES

1.1 Global energy demand since 1800 and contribution from renewable in 2019 [3].. . 1

1.2 Atmospheric CO_2 content over past several milennia measured from ice cores and a direct correlation with elevated earth's atmospheric temperature [7]. 2

2.1 The energy band structure and various potential energies.. 4

2.2 Various recombination mechanisms 1. Radiative recombination, 2. Non-radiative Auger recombination 3. Trap assisted recombination 4. Surface recombination . 8

2.3 A homojunction in thermal equilibrium (a) space-charge distribution (b) carrier density distribution (c) Electric field distribution (e) Energy band-diagram . . . 10

2.4 (a) Schematic of the different layers deposited with typical thicknesses (b) High resolution crossectional TEM image of a poly-crystalline CdTe thin-film solar cell [20].. 13

2.5 (a) Energy band diagram for CdTe thin-film solar cell at 0 V and AM 1.5G illumination typical to the device structure shown in figure 2.4.. 13

2.6 (a) Current-voltage curve with the critical parameters (b) Quantum efficiency and photoluminescence (c) Mott-Schottky plot (d) Carrier concentration and voltage bias a function of depletion width. 14

3.1 Different types of simplified heterojunctions 19

3.2 (a) Schematic of two semiconductors of different E_g and conductivity in isolation (b) Ideal anisotypic heterojunction formation at thermal equilibrium with respective band-bending in the semiconductors. 20

3.3 (a) Relative position of CdTe Valence band maxima with respect to the work function of various metals (b) Energy band-diagram at AM 1.5G illumination for typical CdTe solar cell at 0 V. Inset shows a back to back double diode model. 22

3.4 (a) Energy band diagram of p-type semiconductor and metal when in separated case, (b) formation of a back barrier, (c) when a forward voltage bias is applied, and (d) when a reverse voltage bias is applied. 23

3.5 Energy-band diagrams for ideal MIS capacitors for p-type semiconductor at different voltage bias conditions (a) equilibrium at V = 0, (b) accumulation at V < 0, (c) depletion at V > 0, (d) inversion at (b) accumulation at V > 0 than that for depletion case. 24

3.6 Relative energy band position of semiconductors in reference to CdTe. 25

4.1 Superstrate structure with variation in the emitter for CdTe-based solar cells. . . 27

4.2 J-V plot of CdTe-based TFSCs with various emitters of optimized thicknesses. . . 28

4.3 Improvement in CdTe TFSCs manufactured at CSU over the last 6 years [46]. . . 30

4.4 Improved optical transmission measurements with increasing Mg fraction in $Mg_xZn_{1-x}O$. The inset presents the optical band-gap measured using the Tauc method [46]. 32

4.5 Glancing-angle XRD measured for $Mg_xZn_{1-x}O$ for varied x [46].. 33

4.6 J-V plot of best performing cell with varying Mg fraction in $Mg_xZn_{1-x}O$. 35

4.7 Box plot of J-V parameters of 25 solar cells with varying 'x' in $Mg_xZn_{1-x}O$ [46]. . 36

4.8 Quantum efficiency of CdTe-based solar cells with variation in the Mg fraction in the $Mg_xZn_{1-x}O$ emitter with the normalized AM 1.5G solar spectrum [46].. . . 37

4.9 XPS spectra for various samples (a) VBM of ZnO bulk and binding energy of $Zn_{2p3/2}$ (b) VBM of CdSeTe bulk and binding energy of $Cd_{3d5/2}$ (c) Binding energy difference between the $Zn_{2p3/2}$ and $Cd_{3d5/2}$ at the ZnO/CdSeTe interface (d) VBM for $Mg_xZn_{1-x}O$ for x = 0.00, 0.10, 0.15 39

4.10 Relative energy band position of $Mg_xZn_{1-x}O$ with reference to CdSeTe. 41

4.11 Simulated E_C at the MgZnO/CdSeTe interface for varied 'x' at 0 V [46]. 42

4.12 PL measured for devices with various Mg fraction in MgZnO [46]. 43

4.13 TRPL decay for devices with various Mg fraction in $Mg_xZn_{1-x}O$. Fastest decays observed for x = 0 and 0.35. [46]. 43

4.14 Mott-Schottky plot from C-V measured for different Mg fraction. Inset shows the variation in depletion width at 0 V. 44

4.15 Low Temperature J-V curves for (a) x = 0.00 and (b) x = 0.15. (c) V_{OC} versus temperature with fitted parameters [46]. 45

4.16 (a) Transmission of two filters in reference to normalized AM 1.5G spectrum. (b)-(d) J-V measurements for various illumination conditions for CdS-CdTe, $Mg_{0.25}Zn_{0.75}O$-CdTe and $Mg_{0.25}Zn_{0.75}O$-CdSeTe/CdTe respectively [20]. 46

4.17 Cross over between the light and dark curves for MgZnO/CdSeTe/CdTe devices with different Mg fractions in MgZnO. 48

4.18 Distortion in the filtered light curves with different Mg fractions in MgZnO. . . . 48

4.19 (a) Schematic of the occupation and release of the electrons from the acceptor type defect states in dark and with blue photons in a wide band-gap emitter (b) Simulated J-V distortions under various illumination conditions [20]. 50

4.20 (a)-(b) Light and dark J-V curves measured at various interval during light soaking (c)-(d) Simulated light and dark J-V curves generated by varying the occupied acceptor defects (N_t) in MgZnO (x = 0.20). 51

4.21 Comparison of J-V curves measured under different illumination conditions for CdTe-based solar cells with (a) undoped MgZnO emitter (b) Ga-doped MgZnO [20]. (Both sets of cells had Mg fraction x = 0.25) 52

4.22 (a)High angle annular dark field STEM image of a MgZnO:Ga/CdSeTe interface. (b) Intensity profile of elemental distribution measured by energy-dispersive X-ray spectroscopy (XEDS) in direction of arrow in (a). (c) Expanded scale to highlight the Cl and Ga signals (d) XEDS signals for various elements [20]. (*measured at University of Illinois Chicago) 53

4.23 Comparison of undoped and Ga-doped MgZnO (a) QE and PL measurement (b) TRPL measurement (c) Mott-Schottky plots (d) Carrier-density vs. depletion-width plot. 54

4.24 Box plot of J-V parameters for 25 small area solar cells with 100-nm undoped MgZnO, bilayer of 100-nm undoped and 20-nm Ga-doped MgZnO, and 100-nm Ga-doped MgZnO emitter layer [20]. 55

4.25 Efficiency contour plot with varied carrier concentration in the MgZnO emitter and absorber, for recombination lifetimes of 2, 10, and 50 ns for $S_{IF} = 10^4$ and 10^6 cm/s [26]. 57

4.26 (a) Carrier concentration comparison for typical Cu-doped and As-doped absorbers derived from C-V measurement done at 100 kHz (b)Box plot comparison of efficiency of As-doped and Cu-doped absorbers with undoped MgZnO [26]. . . 58

4.27 A comparison of As-doped and Cu-doped absorbers between the experiment (solid lines) and simulations (dotted lines). The inset presents the simulation parameters [26]. 59
4.28 Energy band diagram at 700 mV for four points in Fig. 4.25(c) [26].. 60
4.29 Electron and hole densities at the MgZnO/CdSeTe interface for the four cases from Fig. 4.25(c) at 700 mV [26]. Band diagrams are illustrated in Fig. 4.28. . . 61
4.30 The deviations in device efficiency with varied S_{IF}, bulk carrier lifetimes with increasing carrier density in absorber [26]. 63

5.1 Schematic of the device structure for various back contact study.. 66
5.2 (a) Schematic of the device structure. (b) Relative position of VBM and work functions of various back contacts with respect to CdTe. 68
5.3 Box plot of J-V parameters for the 10 small area devices with various elements as a back electrode in direct contact with CdTe. 69
5.4 (a) J-V plots, (b) QE plots, (c) Carrier density vs. depletion width plots, and (d) Mott Schottky plot for the best devices from Fig. 5.3.. 70
5.5 Schematic of the device structure with 30 nm of Te as back buffer.. 72
5.6 Box plot of J-V parameters with Te back buffer and various back electrode. . . . 73
5.7 (a) J-V plots, (b) QE plots, (c) Carrier density vs. depletion width plots, and (d) Mott Schottky plot for the best devices from Fig. 5.6.. 74
5.8 (a)Schematic of the device structure with TeO_x as back buffer (b) J-V plots for typical devices with various thickness of TeO_x and $CdCl_2$ 76
5.9 Box plot of J-V parameters of 25 small area cells with varied TeO_x thickness (0 nm, 5 nm, 10 nm) and $CdCl_2$ sequence. Dashed boxes are for a single $CdCl_2$ step. 77
5.10 (a) PL spectra intensity and (b) TRPL decay of select devices from Fig. 5.8 . . . 78
5.11 (a) Relative position of energy bands for CdTe and TeO_x (b) TRPL decay from back illumination for TeO_x with a transparent back contact. 78

5.12 Box plot of the J-V parameters of 25 small area devices from each substrates with TeO_x deposited in a Ar/O_2 ambiance. 80

5.13 (a) J-V plots and (b) spectral PL intensity for best devices, (c)-(d) capacitance measurements of best devices with TeO_x deposited in Ar only and in Ar/O_2 = 95/5 ambiance.. 81

5.14 (a) Schematic of Se/ITO transparent back contact (b) Comparative J-V plot of Se/ITO and Se/C/Ni back contact (c) Transmission measurement for various structures (d) QE plot of Se/ITO transparent back contact with front and back illumination 83

5.15 (a) Schematic of the device structure (b) J-V plots for best devices. 84

5.16 (a) PL measurement, (b) TRPL measurement, and (c) QE measurements with illumination from front and back of the cell for combinations of MgO and NiO back buffers. 85

5.17 (a) High resolution TEM image of MgO/NiO bilayer metal oxide back contact for CdTe. (b) Zoomed region at the hole transport interface (* measured at University of Illinois Chicago) 85

6.1 (a) A passivated emitter and rear contact structure for a polycrystalline CdTe. (b) A hole selective back contact with a passivating oxide and proper band bending.. 92

LIST OF SYMBOLS

Symbol	Description	Unit
$\boldsymbol{A}$	Diode ideality factor	-
$\mathbf{A}^*$	Richardson constant	$A/cm^2\text{-}K^2$
$\mathbf{C_D}$	Depletion layer capacitance per unit Area	F/cm^2
$\mathbf{D_n}$	Diffusion coefficient for electrons	cm^2/s
$\mathbf{D_p}$	Diffusion coefficient for holes	cm^2/s
$\mathbf{E_c}$	Bottom edge of conduction band	eV
$\mathbf{E_D}$	Donor dopant energy level	eV
$\mathbf{E_F}$	Fermi level	eV
$\mathbf{E_{Fn}}$	Quasi-Fermi energy level for electrons	eV
$\mathbf{E_{Fp}}$	Quasi-Fermi energy level for holes	eV
$\mathbf{E_g}$	Energy band gap	eV
$\mathbf{E_i}$	Intrinsic Fermi level	eV
$\mathbf{E_t}$	Trap energy level	eV
$\mathbf{E_v}$	Top edge of valence band	eV
$\mathbf{G}$	Generation rate	$cm^{-3}s^{-1}$
$\boldsymbol{h}$	Planck constant, $= 6.62 \times 10^{-34}$ Js	Js
$\mathbf{J}$	Current density	A/cm^2
$\mathbf{J_n}$	Electron current density	A/cm^2
$\mathbf{J_o}$	Dark saturation current	A/cm^2
$\mathbf{J_p}$	Hole current density	A/cm^2
$\mathbf{J_L}$	Illumination circuit current density	A/cm^2
$\mathbf{J_{sc}}$	Short circuit current density	A/cm^2
$\boldsymbol{k}$	Boltzmann constant, $= 1.38 \times 10^{-23}$ J/K	J/K
$\mathbf{L_p}$	Diffusion length for holes	cm
$\mathbf{L_p}$	Diffusion length for holes	cm
$\mathbf{m_e}^*$	Electron effective mass	kg
$\boldsymbol{n}$	Concentration of free electron	cm^{-3}
$\boldsymbol{n_i}$	Intrinsic carrier concentration	cm^{-3}
$\boldsymbol{n_p}$	Electron density in p-type semiconductor	cm^{-3}
$\boldsymbol{n_{po}}$	n_p in thermal equilibrium	cm^{-3}
$\boldsymbol{n}^+$	Highly doped n-type semiconductor	cm^{-3}
$\mathbf{N_A}$	Acceptor concentration	cm^{-3}
$\mathbf{N_C}$	Effective density of states in conduction band	cm^{-3}
$\mathbf{N_D}$	Donor concentration	cm^{-3}
$\mathbf{N_A}^-$	Ionized acceptor concentration	cm^{-3}
$\mathbf{N_D}^+$	Ionized donor concentration	cm^{-3}
$\mathbf{N_t}$,	Volume defect density	cm^{-3}
$\mathbf{N_t}'$	Areal surface defect density	cm^{-2}
$\mathbf{N_V}$	Effective density of states in E_V	cm^{-3}
$\boldsymbol{p}$	Concentration of free holes	cm^{-3}
p_p	Hole concentration in p-type semiconductor	cm^{-3}
$\boldsymbol{p_{po}}$	p_p in thermal equilibrium	cm^{-3}
$\boldsymbol{p}^+$	Highly doped p-type semiconductor	cm^{-3}
$\boldsymbol{q}$	Elemental unit charge, $= 1.6 \times 10^{-19}$ C	C

Symbol	Description	Unit
$\mathbf{r_{sh}}$	Shunt resistance	Ωcm^2
$\mathbf{R}$	Recombination	$cm^{-3}s^{-1}$
$\mathbf{R_s}$	Series resistance	Ωcm^2
$\mathbf{R_{IF}}$	Interface recombination	$cm^{-2}s^{-1}$
$\mathbf{R_{SRH}}$	Shockley-Read-Hall recombination	$cm^{-3}s^{-1}$
$\mathbf{S_{IF}}$	Interface recombination velocity	cm/s
$\mathbf{S_n}$	Surface recombination velocity for electrons	cm/s
$\mathbf{T}$	Absolute temperature	K
$\mathbf{U}$	Net recombination/generation rate, U = R - G.	$cm^{-3}s^{-1}$
$\mathbf{V_{oc}}$	Open circuit voltage	mV
$\boldsymbol{v_{th}}$	Thermal velocity, = 10^7 cm/s	cm/s
$\mathbf{V_F}$	Forward voltage bias	V
$\mathbf{V_R}$	Reverse voltage bias	V
$\mathbf{W_D}$	Depletion width	μm
$\mathbf{W_{Dn}}$	Depletion width in n-type semiconductor	μm
$\mathbf{W_{Dp}}$	Depletion width in p-type semiconductor	μm
ϵ	Relative dielectric permittivity	F/cm
ν	Conversion efficiency	%
μ	Drift mobility	cm^2/V-s
$\sigma_\mathbf{h}$	Capture cross-section for holes	cm^{-2}
$\sigma_\mathbf{n}$	Capture cross-section for electrons	cm^{-2}
τ	Minority carrier lifetimes	ns
$\tau_\mathbf{n}$	Electron carrier lifetimes	ns
$\tau_\mathbf{p}$	Hole carrier lifetimes	ns
ϕ	Potential or work function	eV
$\phi_\mathbf{b}$	Back barrier height	eV
$\phi_\mathbf{m}$	Metal work function	eV
χ	Electron affinity	eV
$\psi_\mathbf{bi}$	Built-in potential at equilibrium	eV
$\mathbf{\Delta E_C}$	Conduction band offset	eV
$\mathbf{\Delta E_V}$	Valence band offset	eV
$\mathbf{\Delta n}$	Excess photogenerated electrons	cm^{-3}
$\mathbf{\Delta p}$	Excess photogenerated holes	cm^{-3}

Chapter 1

INTRODUCTION

1.1 Need for a clean source of energy

The human population over the last century has exploded. The current world population clocks over 7.5 billion [1] and is projected to reach 8.6 billion in 2030, 9.8 billion in 2050 and 11.2 billion at the turn of the century in 2100 [2]. Global energy consumption to meet the demands of ever growing population has grown exponentially as shown in Fig. 1.1 [3]. Majority of the global energy comes from the non-renewable source of energy, mostly from the fossil fuels. Combustion of fossil fuel emits CO_2 which is a major green house gases.

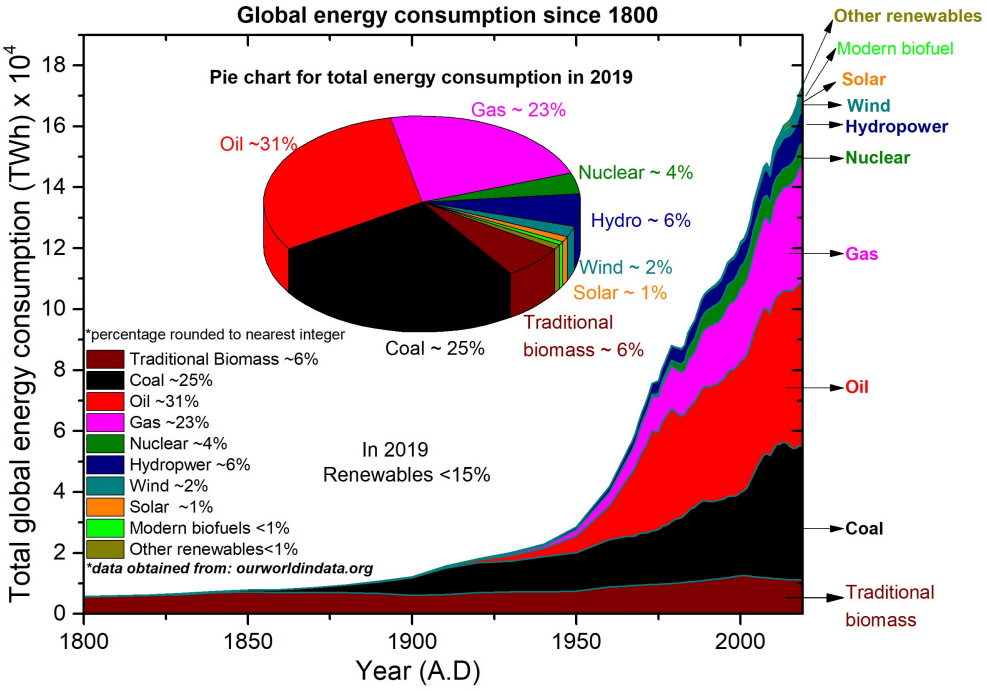

Figure 1.1: Global energy demand since 1800 and contribution from renewable in 2019 [3].

Green house gases like CO_2, methane, nitrous oxide and fluorinated gases act as heat traps to elevate the temperature of earth's atmosphere. A comparative study of CO_2 content in earths atmosphere measured from ice cores show that the CO_2 content in our earth's

atmosphere has increased since the industrial revolution [4, 5] as seen from Fig. 1.2(a). A direct co-relation between the earth's CO_2 content and average global temperature is seen in Fig. 1.2(b).

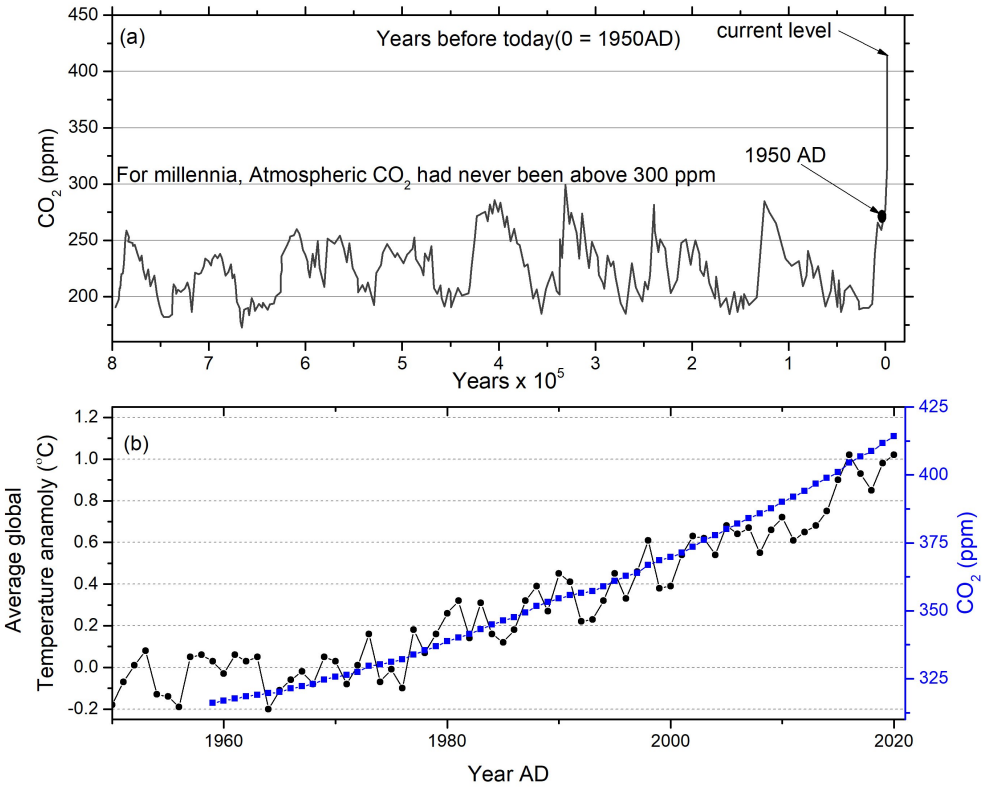

Figure 1.2: Atmospheric CO_2 content over past several milennia measured from ice cores and a direct correlation with elevated earth's atmospheric temperature [7].

The unprecedented amount of CO_2 in earth's atmosphere results in large shifts in weather patterns leading to global warming and climate change, that poses an existential threat to the beings of earth [6]. Nineteen of the warmest years have occurred since 2000, Arctic ice has receded at a rate of 13.1 % per decade, highest atmospheric CO_2 was measured above 400 ppm in 650,000 years, and sea level is rising at 3.3 millimeters/year [7]. On December 12^{th} of 2015, some 196 countries around the globe acknowledged the threat and committed to a legally binding international treaty on climate change to limit global warming of earth below 2 °C by curbing the green house gas emission, commonly known as the Paris Agreement.

1.2 Solar energy

Energy from the sun is nearly limitless. Photovoltaic (PV) methods generate electricity from the solar illumination which is safe, pollution free, and a clean source of energy. An unceasing solar power in excess of 120,000 Terawatts illuminates earth's surface, this energy accumulated for little over an hour will meet our present day annual energy demand projected in Fig. 1.1. Solar energy has the potential to be an answer to the global demand for energy. Over the years, various solar PV technologies have established themselves as one of the cheapest sources of energy. The levelized cost of electricity that gauges the cost of electricity generation of a power plant over it's lifespan is calculated to be the lowest for solar PV electricity. [8]. The global cumulative PV installation at the end of 2019 was above 600 GW and projected to add above 150 GW in 2020/21.

Cadmium telluride (CdTe) PV is a thin-film technology that has a near ideal optical band-gap of 1.5 eV, relatively fast deposition rate of few microns/min, low material usage , low cost of manufacturing and relatively short energy payback time [9]. This makes CdTe an ideal absorber material for thin-film PV. Device efficiency of 22.1 % for cells and 18.6 % for modules has been achieved for CdTe PV [10] that falls short of the theoretical Shockley-Queisser limit for a single junction CdTe solar cell is over 30 % [11]. This presents an ample room for improvement in efficiency to further reduce the cost making it attractive both commercially and economically, the key attributes to the advancement of any technology.

The thesis will focus on the strategy, methods and device physics that are of great importance in improving the device performance of thin-film solar cells, CdTe in particular. Experimental and numerical simulation methods are employed hand in hand to guide and demonstrate improvement in device performance. The work identifies optical band-gap engineering, energy band offset, doping of the absorber and emitter, reduced interface recombination, improved back contact, favourable band bending etc as critical parameters for the improvement of CdTe-based thin-film solar cells (TFSC).

Chapter 2

BACKGROUND

The chapter provides a brief insight to important principles, physics of photovoltaic devices, properties of semiconductors and solar cells, device architecture, various optical/electrical device characterization methods, and key parameters for device simulations. All of these are key to understanding of the fundamentals of how a solar cell works.

2.1 Fundamentals of semiconductors

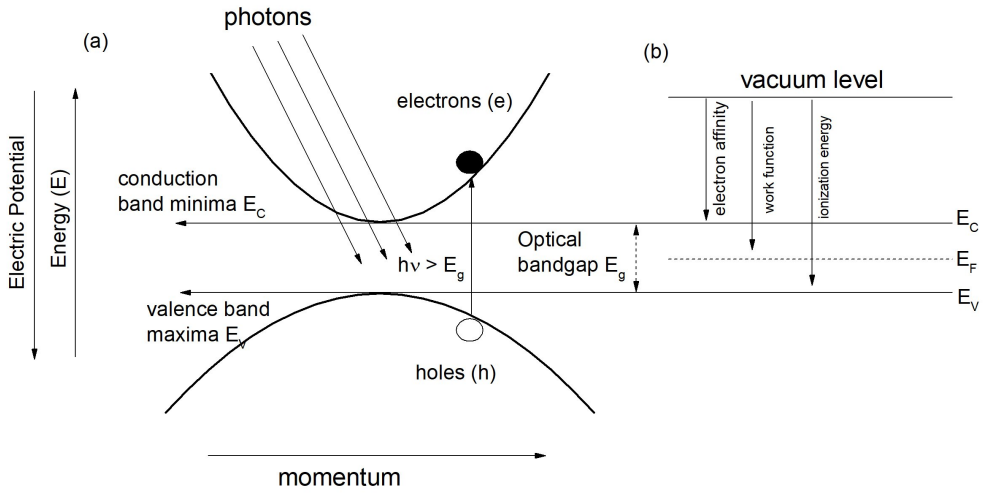

Figure 2.1: The energy band structure and various potential energies.

In most semiconductors, there is a well structured periodic placement of atoms. The smallest unique assembly is called a primitve cell, which corresponds to a crystal structure such as simple cubic, body centered cubic, zinc-blende, rock salt, wurtzite etc. The energy-momentum (E-k) relationship for carriers, the electrons and holes, and the interactions with photons and phonons in the lattice has to be conserved. The mathematical formulation of this criteria leads to a forbidden energy range in which allowed states donot exist for semiconductors as shown in Fig. 2.1 with the exception of defects and dopants [12]. The

upper band is called conduction band (E_C) and lower bands are the valence bands (E_V). The separation between the energy of the lowest E_C called conduction band minima (CBM) and highest E_V called valence band maxima (VBM) is the optical energy band-gap (E_g). Photons with energy greater than E_g will get absorbed, dislodging an electron from the E_V to E_C leaving behind a pseudo particle termed as a hole in E_V, the sub band-gap photons will not get absorbed but will be transmitted.

2.2 Fermi level and carrier density

Taking account of Pauli's exclusion principle which implies that each allowed energy state can be occupied at most by two electrons of opposite spin, the probability of occupation of an allowed state of energy E is given by *Fermi-Dirac distribution function f(E)* given by

$$f(E) = \frac{1}{1 + e^{\frac{(E-E_F)}{kT}}} \tag{2.1}$$

where k is Boltzmann's constant, T is absolute temperature and E_F is Fermi level. The Fermi level is defined as the highest energy level occupied by electrons at a given temperature. At T = 0 K all states below E_F are filled and above E_F are empty. At T > 0 K, the number of allowed states per unit volume *N(E)* in a semiconductor in the allowed energy bands is given by

$$n(E) = \frac{8\sqrt{2}\pi m_e^{*3/2}}{h^3}(E - E_C)^{3/2} \tag{2.2}$$

where h is Planck constant, m^*_e is effective mass of electrons. Now, the electron density (n) in the conduction energy band is given by

$$n = N_C e^{(E_F - E_C)/kT} \tag{2.3}$$

where N_C is effective density of states in conduction band. Similarly, the hole density (p) in the valence band is given by

$$p = N_V e^{(E_V - E_F)/kT} \tag{2.4}$$

For intrinsic semiconductors in thermal equilibrium, an electron in E_C leaves behind a hole in E_V, so the intrinsic carrier concentration (n_i) is equal to n ($= p$). This gives rise to an equilibrium condition

$$np = n_i^2 = N_C N_V e^{(E_V - E_C)/kT} = N_C N_V e^{E_g/kT} \tag{2.5}$$

$$E_F = \frac{E_C + E_V}{2} + kTln(\frac{N_V}{N_C}) \tag{2.6}$$

Equation 2.6 gives the relative position of the Fermi level. For intrinsic semiconductors, E_F is located near midgap of E_g. Doping of the semiconductors perturbs this intrinsic case. Semiconductors can be doped with a donor or with an *acceptor* atom. A donor atom will lose an electron and become a positively charged ion while acceptor will accept an electron and become negatively charged ion. When a semiconductor is doped with a donor type dopant with density N_D, it introduces dopant energy levels (E_D) closer to the E_C, making the transition of electrons from E_D to E_C much easier. The charge neutrality demands total number of electrons in E_C and holes in E_V to satisfy

$$p - n + N_D^+ = 0 \tag{2.7}$$

where, the $N_D{}^+$ is the density of ionized donors. For large N_D in a semiconductor, the semiconductor material is called n-type, This leads to the approximation

$$n \approx N_D^+ \approx N_D \Longrightarrow n \gg \frac{n_i^2}{N_D} \approx p \tag{2.8}$$

$$n = N_D = N_C e^{(E_F - E_C)/kT} \Longrightarrow E_F - E_C = kTln(\frac{N_D}{N_C}) \tag{2.9}$$

Similarly, materials doped with acceptor dopants will make *p-type* semiconductor with E_F given by,

$$p = N_A = N_V e^{(E_V - E_F)/kT} \Longrightarrow E_V - E_F = kTln(\frac{N_A}{N_V}) \tag{2.10}$$

From equations 2.9 and 2.10, it is clear that the E_F gets pushed closer to E_C for large N_D in n-type semiconductors while the E_F gets closer to E_V for p-type semiconductors.

2.3 Generation and recombination

When there is deviation from the thermal equilibrium condition of $pn = {n_i}^2$, different mechanisms come into play to restore the equilibrium. These processes are recombination (R) when $pn > {n_i}^2$ and generation (G) when $pn < {n_i}^2$. In thermal equilibrium, the net transition rate *U (= R-G)* is zero. Let us assume a p-type semiconductor, with acceptor dopant concentration of N_A with equilibrium electron and hole concentration of n_{po} and p_{po} $\approx {N_A}^-$ respectively at thermal equilibrium. The electrons are called minority carriers and holes are called majority carriers in a p-type semiconductor where $n_{po} \ll p_{po}$. When light with $h\nu > E_g$ is used for illumination, a low-level injection case occurs where the excess carriers $\Delta n = \Delta p$ are fewer than majority carriers p_p which satisfies following conditions

$$n_p = n_{po} + \Delta n \quad \& \quad p_p \approx p_{po} \quad \& \quad p_{po} \gg n_{po} \tag{2.11}$$

The purpose of a solar cell is to extract these excess photo-generated minority carrier Δn by applying appropriate voltage. This low-level injection violates the equilibrium condition, so the excess minority carriers decays via various recombination mechanisms to revert to equilibrium condition:

- ***Radiative recombination*** is opposite of absorption. An electron occupying higher energy state will transition to lower energy state by emitting photon of energy equal to the transition energy difference.

- ***Auger recombination*** is a non radiative recombination when an electron in E_C recombines with hole in E_V by giving excess energy to another electron in E_C. The second electron then relaxes back to it's initial state by releasing phonons.

- ***Bulk recombination*** via the trap states. The impurities in the semiconductor leads to presence of energy levels in the forbidden gap called the trap states. These trap states assist in an efficient recombination via a two step process where, an electron in E_C recombines with the hole at E_V via these trap states as a transit.

- ***Surface recombination*** A surface is a severe defect in a crystal due to lattice interruption, presence of dangling bonds, charge accumulations etc permitting trap states to exist in the forbidden energy gap making it the most efficient recombination mechanism in a semiconductor. This is of particular importance to the thesis as extraction of the photogenerated electron and hole pairs across such defective CdTe surface is critical to the performance of a CdTe-based solar cell.

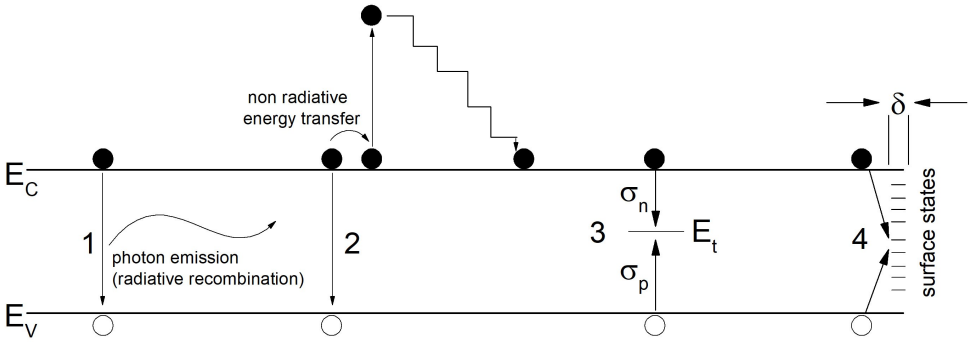

Figure 2.2: Various recombination mechanisms 1. Radiative recombination, 2. Non-radiative Auger recombination 3. Trap assisted recombination 4. Surface recombination

The net rate of recombination of electrons in E_C and holes in E_C via a trap at energy level E_t is given by Shockley-Read-Hall statistics [13, 14, 15].

$$R_{SRH} = \frac{\sigma_n \sigma_p v_{th} N_t (pn - n_i^2)}{\sigma_n [n + n_i e^{\frac{E_t - E_i}{kT}}] + \sigma_p [p + n_i e^{\frac{E_i - E_t}{kT}}]} \tag{2.12}$$

where, where σ_n and σ_p are the electron and hole capture cross sections respectively, n and p are electron and hole density, n_i is intrinsic carrier density, v_{th} is thermal velocity and E_i is intrinsic Fermi level. The recombination rate in equation 2.12 is maximum when $E_i = E_t$. This suggests that the mid-gap trap states near midgap are efficient bulk recombination

centers reducing equation 2.12 to

$$R = \frac{\sigma_n \sigma_p v_{th} N_t (pn - n_i^2)}{\sigma_n (n + n_i) + \sigma_p (p + n_i)} \tag{2.13}$$

For p-type semiconductor under low-level injection condition for equation 2.11, the total recombination rate is

$$R = \frac{\sigma_n \sigma_p v_{th} N_t [p_{po}(n_{po} + \Delta n) - n_i^2]}{\sigma_p p_{po}} \quad \approx \sigma_n v_{th} N_t \Delta n \approx \frac{\Delta n}{\tau_n} \tag{2.14}$$

where τ_n is electron lifetime or often referred to as minority carrier lifetime given by

$$\tau_n = \frac{1}{\sigma_n v_{th} N_t} \tag{2.15}$$

The expressions derived here help quantize the bulk quality of a semiconductor. A reduction in N_t or σ_n will increase the τ_n and reduce bulk recombination. Various methods are implemented during the solar cell device fabrication to achieve this and is key to improving photovoltaic characteristics of absorber materials used for solar cell fabrication.

A similar argument can be made for the recombination at the surfaces. Let us assume that the surface of area '*A*' with thickness 'δ' on the surface has defect density of N_t. On the surface of the semiconductor the *areal surface defect density* $N_t{}'$ is the key parameter that governs the recombination. The surface defect density $N_t{}'$ is related to volume defect density N_t by $N_t{}' = N_t \times \delta$. Feeding this to equation 2.15 will give

$$\tau_n = \frac{\delta}{\sigma_n v_{th} N_t} \quad \Longrightarrow S_n = \frac{\delta}{\tau_n} = \sigma_n v_{th} N_t^{'} \tag{2.16}$$

where S_n is electron surface recombination velocity which gauges the quality of the surface. In a solar cell, the semiconductor absorber material will have a contact (either a metal or another semiconductor) instead of a free surface to assist in extraction of the charges. The surface recombination velocity term S_n in such case becomes the interface recombination velocity

(S_{IF}). S_{IF} as we will discuss later is a key parameter to gauge the quality of an interface of solar cells that measures the selectivity of charge extraction from a semiconductor. The recombination in the grain boundaries of the poly-crystalline materials is also described by equation 2.16. Similar mathematical equations 2.15 and 2.16 hold true for holes.

2.4 P-N junction

A p-n junction is a two-terminal device formed by bringing a n-type and a p-type semiconductor together. The doping profile, device geometry, semiconductor deposition process and parameters can be altered to engineer and exploit the various optoelectronic properties by forming a junction between the semiconductors of different types.

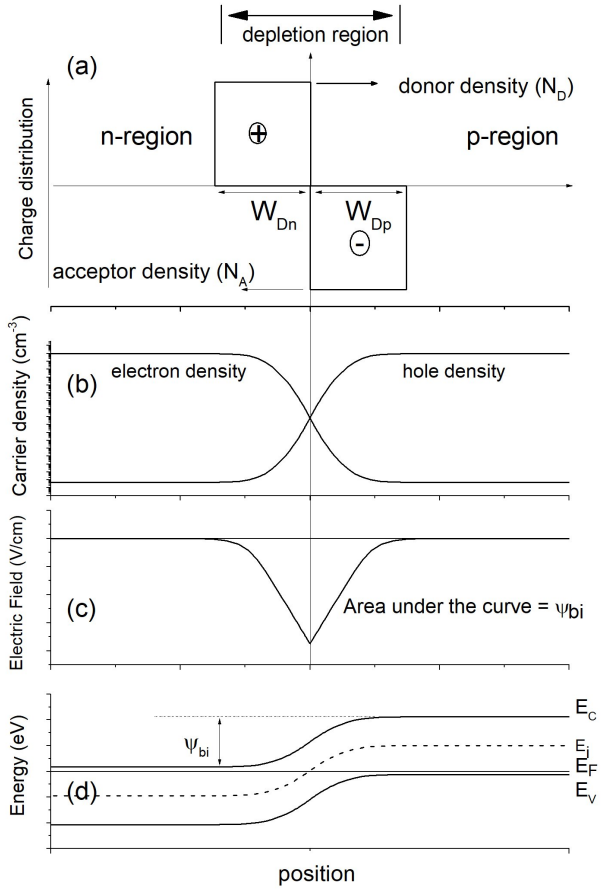

Figure 2.3: A homojunction in thermal equilibrium (a) space-charge distribution (b) carrier density distribution (c) Electric field distribution (e) Energy band-diagram

A homojunction is an intimate interface that appears between a n-type and a p-type semiconductor of similar material. This enables the diffusion of holes from p-type and electrons from n-type into the adjacent layer until an equilibrium is achieved. This exchange leaves behind ionized atom cores, a positive charge is built up in the n-type region and a negative charge in the p-type region referred to as depletion charge as shown in Fig. 2.3(a). Due to this, an electric field is created from the n-type to the p-type region that counters the diffusion by the drift current. At equilibrium, the drift and diffusion currents are equal and deplete the region adjacent to the p-n interface of any free charges. This region is called depletion region. In thermal equilibrium, the Fermi position is constant which governs the band-bending in the adjacent regions resulting in the energy band-diagrams as shown in Fig. 2.3(d). A built-in potential(ψ_{bi}) is created in the depletion region given by

$$\psi_{bi} \approx \frac{kT}{q} ln \frac{N_D N_A}{n_i^2} \tag{2.17}$$

The total negative charge per unit area in p-type must be equal to the total positive charge in n-type which leads to the condition

$$N_A D_p = N_D D_n, \quad W_D = W_{Dn} + W_{Dp} = \sqrt{\frac{2\epsilon}{q}\left(\frac{N_A + N_D}{N_A N_D}\right)\psi_{bi}} \tag{2.18}$$

where ϵ is relative permittivity of the semiconductor. $\mathrm{W_D}$, $\mathrm{W_{Dp}}$ and $\mathrm{W_{Dn}}$ are total depletion width and extended depletion width in p-type/n-type respectively. When an external voltage (V) is applied to the two terminals of the heterojunction, the electrostatic potential change is given by (ψ_{bi} - V), The junction capacitance per unit area ($\mathrm{C_D}$) is given by

$$C_D = \frac{\epsilon}{W_D} = \sqrt{\frac{qN_A N_D \epsilon}{2(N_A + N_D)(\psi_{bi} - V)}} \tag{2.19}$$

Solving the drift and diffusion equation for the charges the total diode current density (J) across the terminals of the junction is given by

$$J = J_n + J_p = J_o \left[e^{\frac{qV}{kT}} - 1 \right] \tag{2.20}$$

where J_o is dark saturation current which is a function of recombination lifetime (τ), diffusion lengths ($D_{n,p}$) that are determined the quality of semiconductor material and is given by

$$J_o = q n_i^2 \left(\frac{D_p}{L_p N_D} + \frac{D_n}{L_n N_A} \right), \quad L_{n,p} = \sqrt{D_{n,p} \tau_{n,p}} \tag{2.21}$$

2.5 CdTe thin-film solar cell

CdTe thin-film solar cells (TFSCs) are an one-sided, abrupt heterojunction. Typical CdTe TFSCs are fabricated on a glass substrate which provides both mechanical support and an optical transparency. Depending on whether the light enters the cell from a glass side or the film side, the device architecture is termed as superstrate configuration or a substrate configuration. The compatibility of semiconductor deposition sequence, and post deposition processes coupled with the industrial success has made the superstrate configuration a preferred choice and the one that we will discuss for reminder of the dissertaion.

A bilayer of CdSeTe/CdTe of combined thickness of around 4 μm followed by $CdCl_2$ treatment is performed in a single vacuum chamber with multiple deposition stations for colse space sublimation [16]. The $CdCl_2$ is critical to passivate the grain boundaries, passivate the interfaces, and grade the Se towards the front of the absorber [17, 18, 19, 20]. CuCl treatment is followed by deposition of 30 nm of Te [21, 22]. A bilayer of C/Ni paint in polymer binder is applied to finish the devices. The deposition of these different semiconductors is performed by various physical vapor deposition methods like sputtering, close space sublimation, evaporation etc.

A typical superstrate CdTe TFSC fabricated at Colorado State University (CSU) is as shown in Fig. 2.4. The substrate is usually a soda lime glass from Pilkington that has

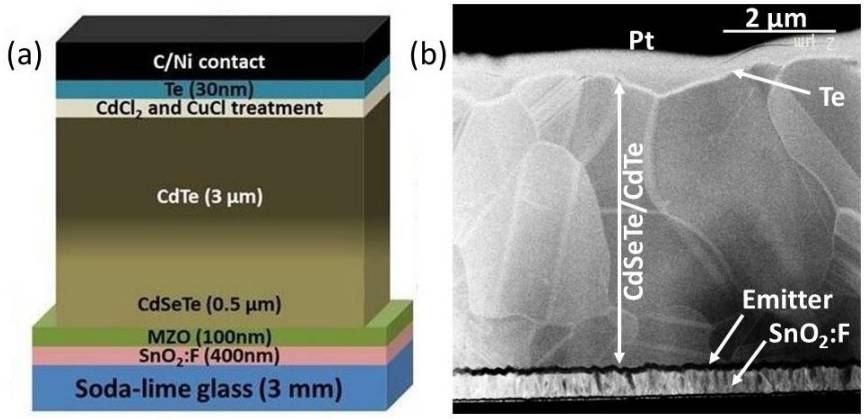

Figure 2.4: (a) Schematic of the different layers deposited with typical thicknesses (b) High resolution crossectional TEM image of a poly-crystalline CdTe thin-film solar cell [20].

a precoated 400 nm of SnO_2:F. A thin buffer layer like CdS, ZnO, MgO, MgZnO etc is deposited which will be the n-type partner, also referred to as an emitter is followed by deposition of the p-type absorber. Ideal emitter layer should have wide band-gap for optical transparency and highly resistive to avoid shunting between the front and the back electrode.

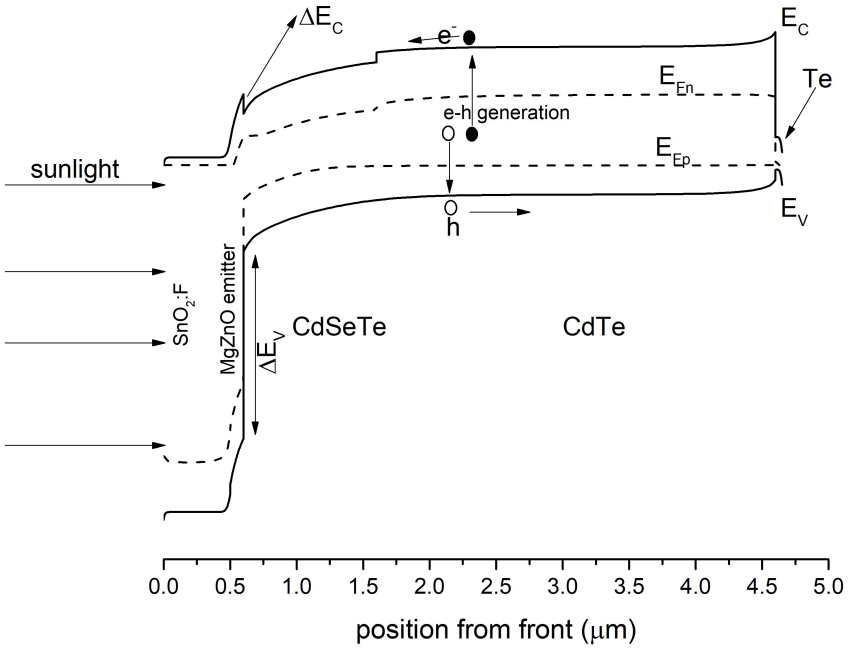

Figure 2.5: (a) Energy band diagram for CdTe thin-film solar cell at 0 V and AM 1.5G illumination typical to the device structure shown in figure 2.4.

The energy band-diagram for a typical MgZnO/CdSeTe/CdTe solar cell is as shown in Fig.2.5. The optical band-gap of SnO_2:F and MgZnO is near 3.7 eV, so photons with energy less than 3.7 eV will pass through the emitter layer and be absorbed in the CdTe absorber. These absorbed photons will then create electron-hole pairs in the region close to SCR. The internal electric field will assist in the collection of these photogenerated electron and hole pairs. The electrons get collected at the front SnO_2:F electrode and the holes at back C/Ni electrode. Various aspects of the CdTe TFSCs will be discussed with help of the energy band diagrams later in Chapter 4. After the device fabrication, various characterization methods such as current-voltage (J-V), quantum efficiency (QE), photoluminescence, capacitance-voltage (C-V) etc. are carried out.

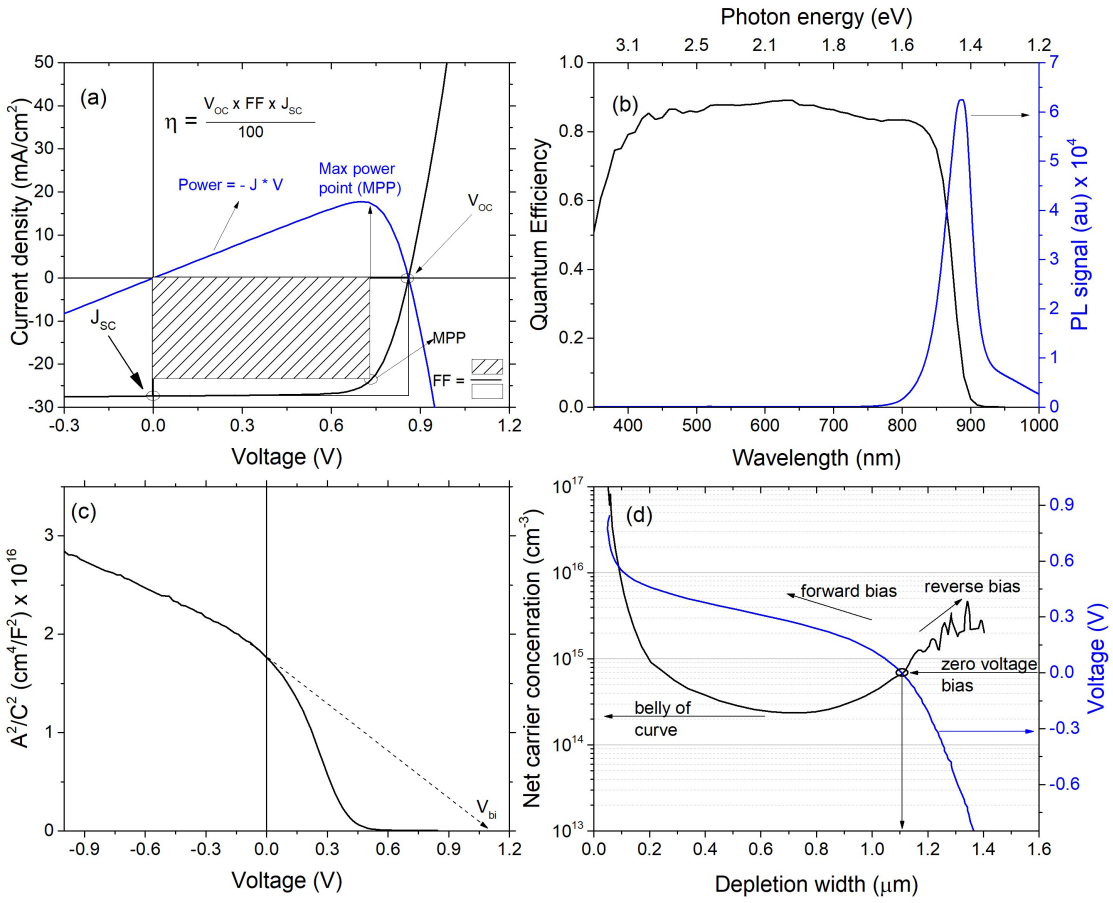

Figure 2.6: (a) Current-voltage curve with the critical parameters (b) Quantum efficiency and photoluminescence (c) Mott-Schottky plot (d) Carrier concentration and voltage bias a function of depletion width.

An example of a J-V curve is in Fig. 2.6(a). An ideal solar cell will have the J-V curve of the p-n junction diode shifted by the light generated current J_L. The key parameters are short-circuit current (J_{SC}), the current measured at 0 V, open-circuit voltage (V_{OC}) measured when the current across the terminals is zero, and fill factor (FF) which measures the squareness of the diode curve at maximum power point (MPP). The conversion efficiency of a solar cell is the product of these three terms divided by the incident power of a standard solar spectrum equal to 100 mW/cm^2. A typical diode equation for a solar cell with various parasitic losses is given by equation 2.22 [23], a slight modification to equation 2.20

$$J(V) = J_o \left[e^{\frac{q(V - R_S J)}{AkT}} - 1 \right] + \frac{V - R_S J}{r_{sh}} - J_L \tag{2.22}$$

where R_S is series resistance, r_{sh} is shunt resistance, and A is an ideality factor, J_L is illumination current density.

Quantum efficiency measures the spectral response of a solar cell at zero voltage, a measure of probability of number of carriers collected by a solar cell to the number of photons incident on the solar cell. The typical QE curve is shown in Fig. 2.6(b) and is given by

$$QE_\lambda = \frac{number\,of\,electron\,hole\,pairs\,collected}{number\,of\,photons\,incident}; \quad J_{SC} = q \int F_\lambda . QE_\lambda . d\lambda \tag{2.23}$$

where F_λ is photon flux density per unit wavelength. The integrated area under the QE curve gives a value that should be equal to the J_{SC}. Photoluminescence (PL) measures the quality of the absorber material used for solar cell. It measures the flux of light emission from absorber after the absorption of monochromatic photons from a laser. The PL emission photons correspond to the E_g for a good absorber material as shown in Fig. 2.6(b). An extension of a normal PL is a time-resolved PL (TRPL) where a short laser pulse is used for excitation and the decay of the PL emission as a function of time is measured to derive the carrier lifetimes [24].

The device architecture described in Fig. 2.4 is such that the p-type absorber is deposited on a degenerate highly doped n-type SnO_2:F with a thin 100 nm of MgZnO emitter sandwiched in between. The doping in the absorber is much smaller than that of SnO_2:F. Applying the condition $N_A \ll N_D$ to equation 2.18, we get $W_{Dp} \gg W_{Dn}$, meaning the depletion width is nearly entirely in the p-type absorber side. A voltage-dependent capacitance measurement can be performed and the depletion width and junction capacitance per unit area for a solar cell can be derived from equation 2.19 as

$$W_D = \frac{\epsilon}{C(V)} \quad ; \quad C(V) = \sqrt{\frac{q\epsilon N_A}{2(\psi_{bi} - V)}} \Longrightarrow N_A = \frac{C^3}{q\epsilon}\frac{\Delta V}{\Delta C} \tag{2.24}$$

A Mott-Schottky plot is obtained for a typical CdTe TFSC as shown in figure 2.6(c) using equations of 2.24. The y-intercept will give a measure of the depletion width at 0 V and x-intercept extrapolated near 0 V will give a measure of the built-in potential of the solar cell and the slope will give the net acceptor density in the absorber. The carrier density Vs. depletion width for varied voltages is as shown in Fig. 2.6(d) that has a shape, often referred to as a belly. The net carrier concentration in the CdTe absorber is measured at the bottom of the "belly".

2.6 Numerical Simulations

The device physics for a solar cell is obtained for the solution of Poisson's equations or Gauss's law and continuity equations for electrons and holes expressed by the equations [12]

$$\nabla.\epsilon\nabla\phi = -q(p - n + N_D^+ - N_A^-) \tag{2.25}$$

$$\nabla.\vec{J_n} = q(R - G) + q\frac{\partial n}{\partial t} \tag{2.26}$$

$$-\nabla.\vec{J_p} = q(R - G) + q\frac{\partial p}{\partial t} \tag{2.27}$$

where ϵ is dielectric constant, ϕ is electrostatic potential, n and p are carrier concentration, $N_D^+$and N_A^- are ionized donor and acceptor cores, J_p and J_n are hole and electron current densities, R and G is recombination and generation. The drift component caused by the electric field and the diffusion component caused by the carrier concentration gradient lead to the current density equations as [12]

$$\vec{J_n} = q\mu_n n\vec{E} + qD_n\nabla n \tag{2.28}$$

$$\vec{J_p} = q\mu_p p\vec{E} - qD_p\nabla p \tag{2.29}$$

where the μ_n and μ_p are electron and hole mobility, $\vec{E}$ is electric field. D's are carrier diffusion constants given by $D = (\frac{kT}{q}\mu)$. At steady state condition, $\frac{\partial p}{\partial t} = 0$ and $\frac{\partial n}{\partial t} = 0$, the above equations can be simplified to [12]

$$\vec{J_n} = q\mu_n n\vec{E} + qD_n\frac{dn}{dx} = q\mu_n\left(n\vec{E} + \frac{kT}{q}\frac{dn}{dx}\right) = \mu_n n\frac{dE_{Fn}}{dx} \tag{2.30}$$

$$\vec{J_p} = q\mu_p p\vec{E} - qD_p\frac{dp}{dx} = q\mu_p\left(p\vec{E} - \frac{kT}{q}\frac{dp}{dx}\right) = \mu_p p\frac{dE_{Fp}}{dx} \tag{2.31}$$

where E_{Fn} and E_{Fp} are quasi Fermi energy levels for electrons and holes, respectively. Most numerical simulation packages are equipped to solve these equations with the various parameters that define the solar cell. In this work we will be using Solar Cell Capacitance Simulator in 1 Dimension (SCAPS-1D) as our numerical simulation tool [25]. The table 2.1 here gives the basic parameters used for numerical simulations used for the remainder of this dissertation [26].

For a straight forward conclusion, the front and back electrodes can be assumed to be ohmic or a non-ohmic Schottky barrier. The baseline for the simulation is considered to have a ohmic contact for electrons at front electrode and a back barrier of 0.3 eV for holes. The r_{sh}= 1 MΩ.cm^2 and a R_S = 1 Ω.cm^2 typical to the CdTe TFSCs is used as a baseline during numerical simulations. Illumination conditions of AM 1.5G at 300 K is considered.

Table 2.1: Critical parameters used for the numerical simulation using SCAPS-1D

Parameters	$SnO_2 : F$	$MgZnO$	$CdSeTe/CdTe$	Te
Thickness (nm)	500	100	1500/3000	50
E_g (eV)	3.2-3.9	3.5	1.4/1.5	0.33
electron affinity (eV)	4.0	4.0	4.2/4.1	5.17
Relative permittivity (ϵ/ϵ_o)	9.0	10.0	9.4	28
Effective density of states in E_c (cm^{-3})	2.2×10^{18}	1.1×10^{18}	8×10^{17}	10^{18}
Effective density of states in E_v (cm^{-3})	1.8×10^{19}	1.8×10^{19}	1.8×10^{19}	10^{18}
electron/hole density n/p (cm^{-3})	n:10^{18}	n:10^{14}-10^{18}	p:10^{14}-10^{17}	p:10^{18}
electron/hole mobility ($cm^2V^{-1}s^{-1}$)	100/25	100/25	320/40	50/175
electron/hole lifetime (ns)	(τ_n=τ_h)1	(τ_n=τ_h)1	(τ_n=τ_h)1-50	-

Default value of effective mass for electrons and holes was used. The defect densities and characteristics of both bulk and interfaces were varied according to the need.

Chapter 3

SEMICONDUCTOR HETEROJUNCTIONS AND METAL OXIDES AS BUFFER FOR POLYCRYSTALLINE CdTe THIN-FILM SOLAR CELLS

The device architecture of CdTe TFSCs shown in Fig 2.4 consists of multiple layers of semiconductors. These semiconductors have different properties such as optical band-gap, doping type, lattice parameters, potential energies, conductivity etc. These properties play a vital role in determining the qualities of a heterojunction formed between the semiconductors. Lattice matching, energy band-diagram alignment, energy band bending and band-offsets are some of the key parameters that govern the quality of a heterojunction. If the conductivity type differs then the junction is called an anisotype heterojunction. More details can be found in text books of semiconductors such as Ref. [12].

3.1 Simple band alignment

Electron affinity (χ) measures the potential energy required to remove an electron from the conduction band to vacuum level. Taking account of the electron affinity and the optical energy band gaps of semiconductors will lead to different types of combination for E_C and E_V alignment at the interface.

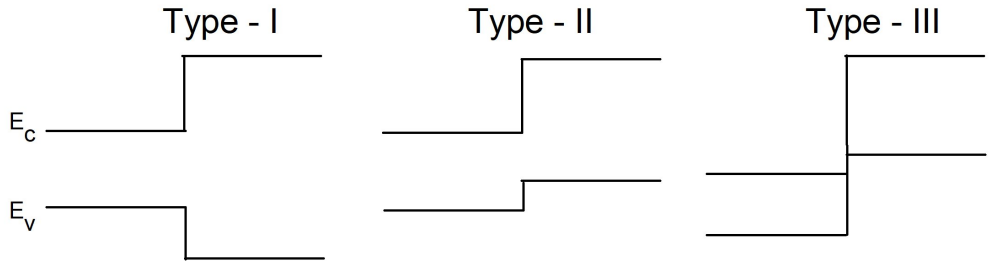

Figure 3.1: Different types of simplified heterojunctions

Simplified combinations of such alignment without any band-bending are Type-I , Type-II, and Type-III shown in the Fig. 3.1. In a Type-I or straddling heterojunction, the E_C and

E_V of one semiconductor is smaller and hence a lower E_g. In Type-II or staggering heterojunction, the relative position of the E_C and E_V in one of the semiconductors is such that the electrons are collected in the E_C of one semiconductor and the holes are collected at E_V of the other semiconductor. This type of band alignment is central to the emitter/absorber interface of CdTe TFSCs. The third Type-III or broken-gap is an extension of Type-II where the E_C at one semiconductor overlaps with E_V on the other semiconductor.

3.2 Band bending at heterojunctions

In previous section we discussed a simple band alignment based on the relative position of the E_C and E_V. However, taking account of the optical band-gap E_g, permittivities (ϵ), work functions (ϕ), and different electron affinity (χ), a simple energy band model for an idealized heterojunction without any interface traps is shown in Fig. 3.2 commonly known as the Anderson model [27]. The work function is defined as the amount of energy needed to remove an electron from the Fermi level E_F.

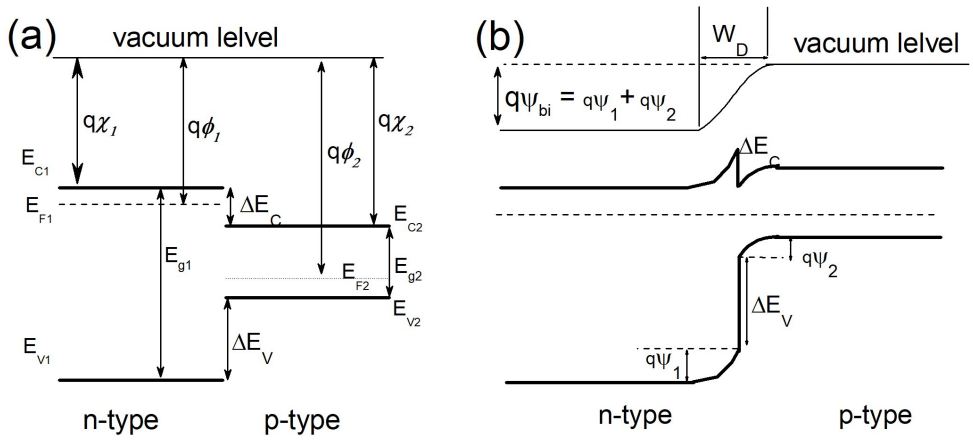

Figure 3.2: (a) Schematic of two semiconductors of different E_g and conductivity in isolation (b) Ideal anisotypic heterojunction formation at thermal equilibrium with respective band-bending in the semiconductors.

In Fig. 3.2(a) the relative position of E_C, E_V, and E_F in reference to the vacuum level is depicted for two isolated semiconductors of different conductivity (n-type and p-type). The heterojunction between semiconductors of different conductivity is called an anisotypic

heterojunction. Here, the optical band-gap , electron affinity and workfunction of n-type semiconductor is E_{g1}, $q\chi_1$, and $q\phi_1$ respectively. Similarly for p-type semiconductors, E_{g2}, $q\chi_2$, and $q\phi_2$ represent the respective quantities. The relative position of E_C, E_V, and E_F for the two semiconductors is governed by the electron affinity of the semiconductors. The conduction band offset (CBO) and valence band offset (VBO) are represented by ΔE_C and ΔE_V respectively. The electron affinity rule ($\Delta E_C = q\Delta\chi$) may not be valid in all cases but choosing ΔE_C as an emperical quantity will give satisfactory approximation of the band offset and band-bending at the heterojunction [28]. At thermal equilibrium, the Fermi level at both sides must coincide, and the vacuum level must be parallel and continuous with the energy bands. The equivalent band bending and energy band diagram looks as shown in Fig. 3.2(b). The total built-in potential and depletion width are partial sum of the respective built-in voltages and depletion widths. Similar arguments can be made for generating energy band diagram for the case when smaller band-gap is a n-type or if both the semiconductors are p-type or n-type to form a heterojunction. More information can be found elsewhere [12].

Fig. 3.2 depicts the heterojunction case when the smaller band-gap is p-type semiconductor. The structure is similar to a MgZnO/CdTe-based TFSCs, where the n-type wide band-gap MgZnO partners with a smaller band-gap p-type CdTe-based absorber. A detailed study of this front heterojunction is presented in chapter 4.

3.3 Metal-Semiconductor contact

In a solar cell, extraction of the photegenerated carriers generated in the absorber is critical to the power conversion efficiency of light energy to electrical energy. The device architecture of a superstrate CdTe TFSC demands a hole contact at the back of CdTe surface. Metals are excellent choice to make hole contact with the CdTe semiconductor to form a metal-semiconductor contact. However, the relatively large ionization energy to eject an electron from the E_V for CdTe means that the work function of a metal should be similar to the ionization energy to make an efficient hole contact.

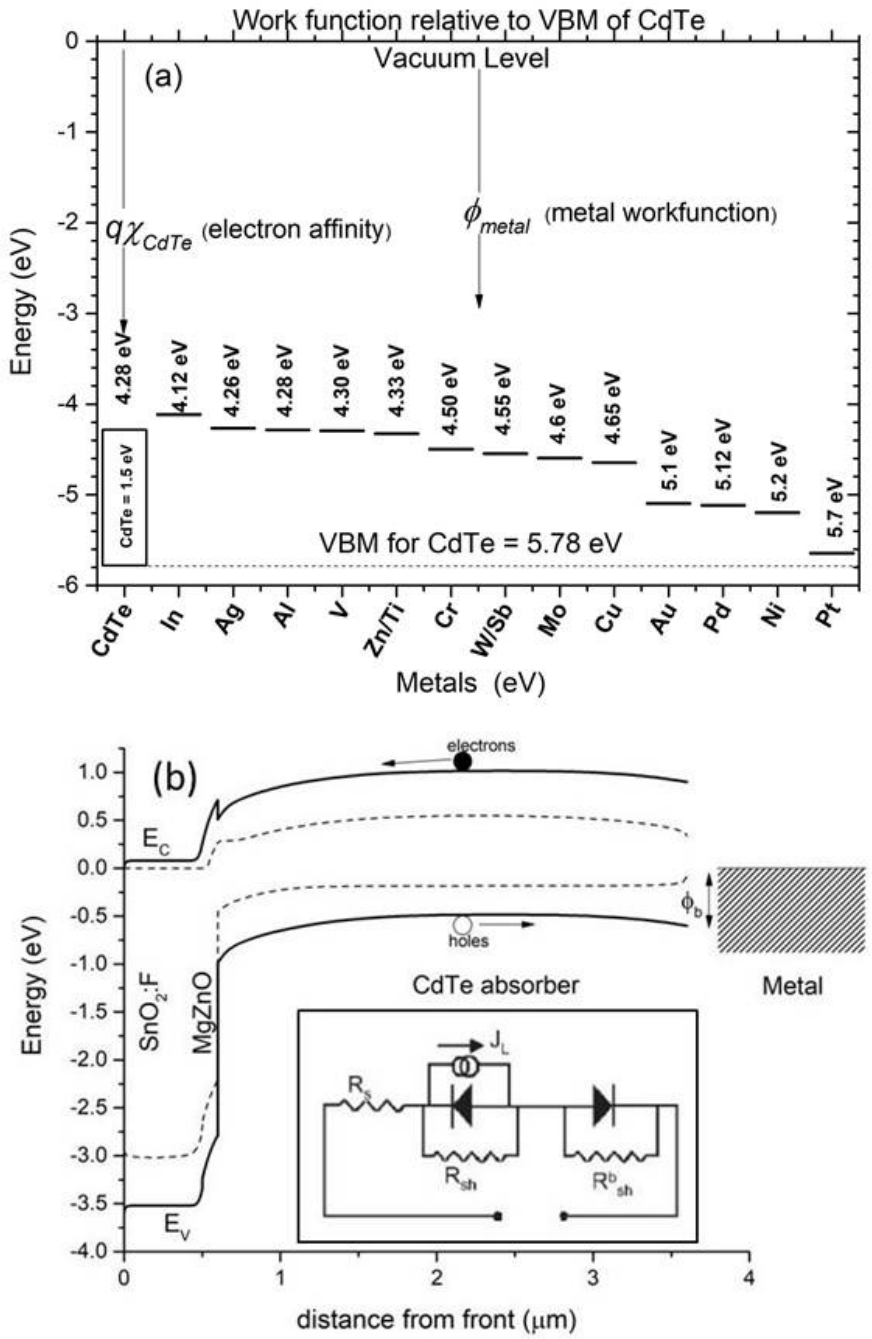

Figure 3.3: (a) Relative position of CdTe Valence band maxima with respect to the work function of various metals (b) Energy band-diagram at AM 1.5G illumination for typical CdTe solar cell at 0 V. Inset shows a back to back double diode model.

Fig. 3.3(a) shows a relative position of CdTe VBM with respect to the work function of most metals used as hole contact [12]. The work function of most metals is not large enough to make an efficient hole contact without formation of a back barrier. In Fig. 3.3(b)

the energy band diagram at 0 V for full AM 1.5G illumination for a typical CdTe solar cell with a metal-semiconductor back contact is presented. A Schottky barrier diode with barrier height (ϕ_b) is created at the back due to the discrepancy in metal work function and the CdTe VBM [29]. A back to back diode model [30] as shown in the inset of Fig. 3.3(b) which has been successfully implemented to explain the various J-V features for CdTe TFSCs. The model assumes two diodes, a primary diode formed between the emitter and absorber, and a secondary diode formed between the CdTe absorber and metal back contact which is in series with the primary diode but in reversed polarity. A working solar cell is always operated at maximum power point at a forward voltage bias of V_{MPP}. This puts the secondary diode at the back in a reverse voltage bias due to it's reversed polarity. A schematic of different voltage bias condition to a typical metal-semiconductor is shown in figure below.

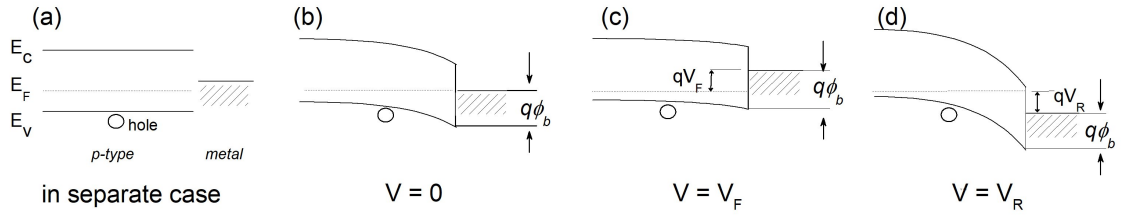

Figure 3.4: (a) Energy band diagram of p-type semiconductor and metal when in separated case, (b) formation of a back barrier, (c) when a forward voltage bias is applied, and (d) when a reverse voltage bias is applied.

When a metal with work function (ϕ_m) is brought in contact with a p-type semiconductor with band-gap E_g and electron affinity (χ) such that $(E_g + q\chi) > q\phi_m$, then a barrier for holes is formed given by $q\phi_b = E_g - q(\phi_m - \chi)$. While this is an over simplified assumption that does not assume the interface defects and surface contamination, it lays foundation for a semiconductor-metal contact and charge transport across the metal-semiconductor interface. The primary mechanisms for charge transport are aided by thermionic emission, tunneling, recombination and diffusion of electrons/holes [31, 32]. A barrier formed at back can lead to charge carrier selectivity issues, and distortions in J-V curves [30, 33, 34, 35]. The unfavorable band-bending for the collection of holes due to the back diode being subjected to a reverse voltage bias condition during the normal cell operation can lead to recombination losses

of minority charge carriers and reduced open-circuit voltage. Multiple strategies has been employed to improve the CdTe back contact like choosing a metal of high work function [34, 36], using a buffer layer to improve lateral conductivity [22, 36, 37, 38], doping of the CdTe back surface with Cu [39, 40, 41] etc. In chapter 5, a comparative study of various back contact is discussed. Different metals with varied metal work function and other back contact schemes has been studied and discussed.

3.4 Metal-Insulator-Semiconductor structures

Introduction of a thin insulating, high dielectric constant material between the semiconductor and the metal will create a metal-insulator-semiconductor (MIS). Such a system can alter the surface condition due to the accumulation, depletion and inversion of charges at the semiconductor/insulator interface. Metal oxides have been the choice for such insulators and has been extensively used to form metal-oxide-silicon (MOS) systems which revolutionized the silicon based transistors.

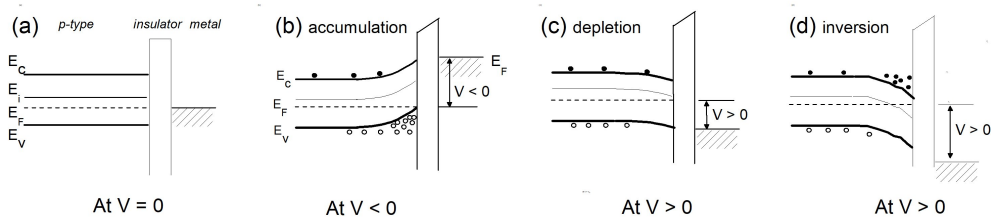

Figure 3.5: Energy-band diagrams for ideal MIS capacitors for p-type semiconductor at different voltage bias conditions (a) equilibrium at V = 0, (b) accumulation at V < 0, (c) depletion at V > 0, (d) inversion at (b) accumulation at V > 0 than that for depletion case.

Fig. 3.5 shows an energy-band diagrams of an ideal MIS capacitor formed with a p-type semiconductor under various voltage bias conditions. For an ideal MIS capacitor, it is assumed that there are no interface traps or oxide charges and there is no carrier transport across the insulator. Further to make things simple, the work function of metal and the semiconductor is assumed to be equal. Again, these assumptions are for ideal case and needs modifications to represent the true scenarios that involve differences in work functions, interface trap densities and oxide charges. This nevertheless provides some useful

insights to the energy band alignment, relative Fermi level position, and band-bending of the semiconductors. In fig. 3.5(b) when a negative voltage is applied to the metal, the valence band edge bends upwards near the surface leading to the accumulation of holes at the surface. Such accumulation of holes at the surface is of particular interest for back contacts for CdTe TFSCs.

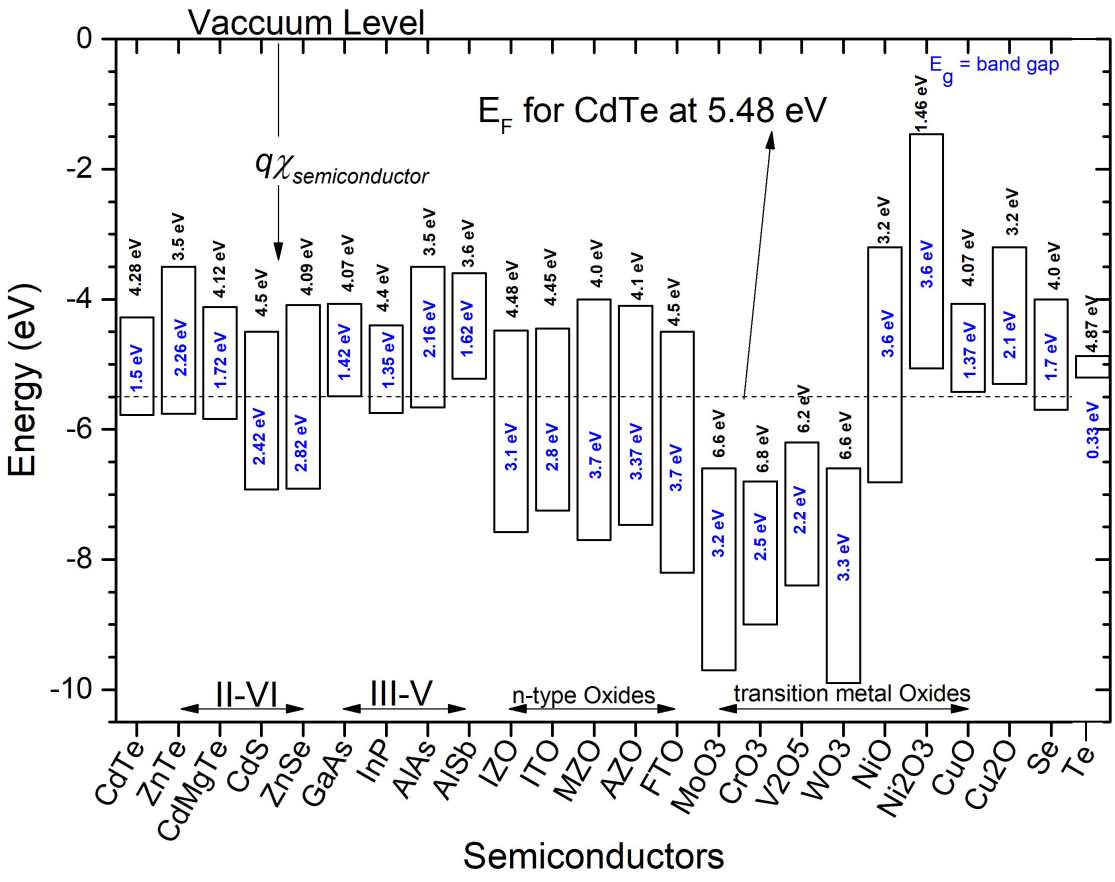

Figure 3.6: Relative energy band position of semiconductors in reference to CdTe.

An appropriate choice of insulator, preferably a thin metal oxide of tunneling thickness, would help in accumulation and extraction of holes at the CdTe surface at the back contact, as the back contact metal is subject to a small negative voltage as discussed earlier. Most metal oxides are wide band-gap and transparent to the visible spectrum. Using them at the back of CdTe opens up the possibility of a bifaciality in CdTe device architecture. The strategy has been implemented in silicon absorber based solar technology to improve the surface passivation, carrier selectivity, minority carrier lifetimes and overall open-circuit voltage.

Commonly found device architecture employed in Si based solar cells are passivated emitter and rear cells (PERC) [42, 43] and tunnel oxide passivated contacts (TOPCon) [44, 45]. In Fig. 3.6 the relative position of E_C and E_V of various metal oxides, and other commonly used wide bandgap semiconductors with CdTe as buffer layers is presented in reference to the energy bands of the monocrystalline CdTe [12]. In the following chapters, we study the use of metal oxides and identify some of the key parameters that govern the choice of such metal oxides as buffer layer for both front electron contact and a back hole contact.

Chapter 4

MgZnO AS EMITTER FOR POLYCRYSTALLINE CdTe THIN-FILM SOLAR CELLS

The emitter is a n-type partner for the p-type absorber in polycrystalline CdTe thin-film solar cells (TFSCs) and plays a critical role in the device performance. An ideal emitter should be wide band-gap for optical tranparency, sufficiently conductive, and carrier selective with a favorable band-offset with the absorber. We will identify and discuss some of the key parameters to employ metal oxides as an emitter for CdTe-based TFSC in a superstrate configuration shown in Fig. 2.4, fabricated at Colorado State University. [1]

4.1 Choice of metal oxide as emitter

In a superstrate configuration, the emitter is the first layer to be deposited on the transparent contact. The emitter material should be robust to the subsequent semiconductor deposition processes and temperatures. Metal oxides have high dielectric constant, thermal tolerance, tunable optical bandgap, easily doped, and high optical transmission to visible solar spectrum. These properties make them attractive candidates for the emitter.

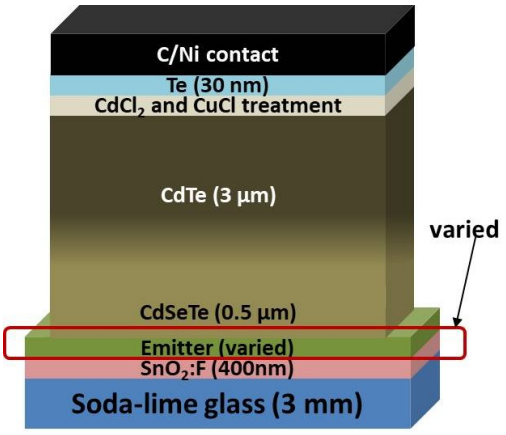

Figure 4.1: Superstrate structure with variation in the emitter for CdTe-based solar cells.

[1] Results discussed in this chapter have been published [20, 26, 46] and some figures are used here.

These emitters are also referred to as "window" layer, as the light enters the absorber through the emitter or a front "buffer" layer because they are adjacent to the absorber at front which improves the junction quality. To further illustrate the point, study of various oxides as an emitter in the device structure shown in Fig. 4.1 was conducted at the Thin-Film Photovoltaic Laboratory at CSU. A comparative J-V plot is presented in Fig. 4.2 along with a traditional CdS/CdTe TFSC for reference.

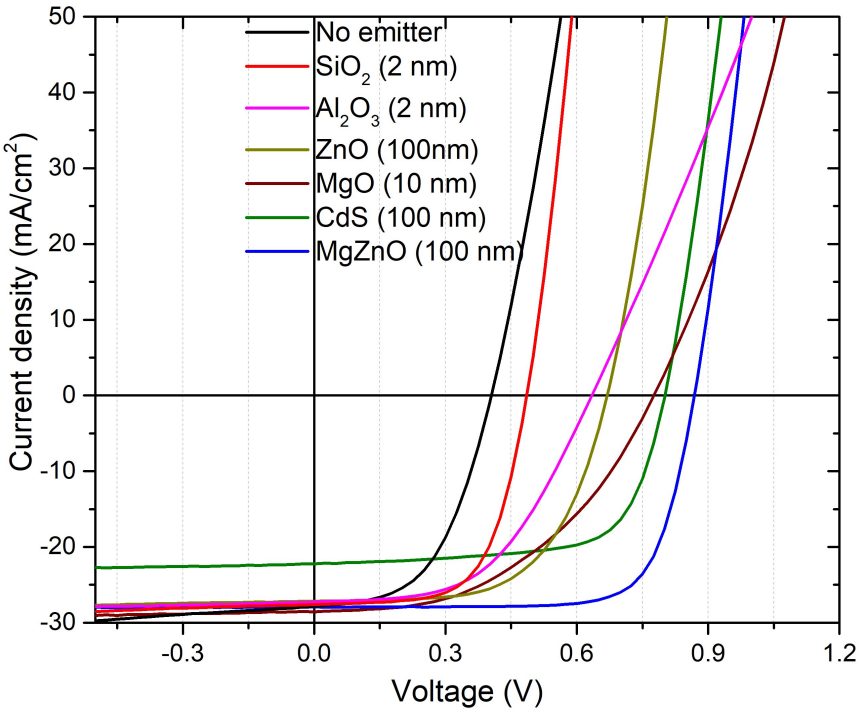

Figure 4.2: J-V plot of CdTe-based TFSCs with various emitters of optimized thicknesses.

Table 4.1: J-V parameters for various emitters for CdTe-based TFSCs in Fig 4.2

Emitter	*Absorber*	J_{SC} (mA/cm^2)	V_{OC} (mV)	FF (%)	$Eff.$ (%)
No emitter	CdSeTe/CdTe	27.9	405	51.9	5.9
CdS (100 nm)	CdTe only	22.2	801	68.3	12.1
SiO_2 (2 nm)	CdSeTe/CdTe	27.6	486	63.4	8.5
Al_2O_3 (2 nm)	CdSeTe/CdTe	27.2	635	51.8	9.0
ZnO (100 nm)	CdSeTe/CdTe	27.2	670	60.5	11.0
MgO (10 nm)	CdSeTe/CdTe	28.5	776	46.8	10.4
MgZnO (100 nm)	CdSeTe/CdTe	27.9	869	75.2	18.2

All the emitters were deposited on a typical Tec glass that has roughly 400 nm of pre-coated SnO_2:F which will also serve as the front electrode. The effect of an emitter is evident

from the J-V parameters of the plots in Fig. 4.2 tabulated in table 4.1. If an absorber is deposited on a commercially available Tec glass with no emitter, the V_{OC} is significantly low. Traditionally, CdS has been the choice of emitter for CdTe TFSCs but these devices suffer from parasitic absorption in the CdS emitter because of it's relatively low band-gap (E_g=2.4 eV) resulting in the lowest J_{SC} in table 4.1. The improved J_{SC} in case of oxide emitters is due to a combination of both, employment of wide band-gap emitter ($E_g > 3.0$ eV) allowing more photons to enter the absorber, and alloying Se in the CdTe-based absorber to form a ternary alloy of CdSeTe with lower $E_g \approx 1.4$ eV for maximizing photon absorption. While a detailed discussion on band-gap engineering for improved J_{SC} will follow in the next section, the effect of oxides as emitter is obvious from the J-V parameters. The intriguing aspect of Fig 4.2 is the performance of device that has the ternary alloy of MgZnO as an emitter. It has superior J-V parameters in comparison to it's constituent oxides of ZnO or MgO only devices. This makes it a worthy candidate for an involved study. The remainder of the Chapter 4 will focus on a detailed study of various aspects of MgZnO emitter layer to serve our understanding of emitter/absorber region. The experimental results coupled with numerical device simulations identify the optical band-gap, energy band-offset, energy band-bending, level of doping etc at the emitter/absorber to be key parameters that govern the performance of a CdTe-based TFSCs.

4.2 Optical band-gap engineering

The progressive improvement in the device performance of CdTe-based TFSCs manufactured at CSU over the last seven years is shown in Fig. 4.3. It is evident that the majority of the improvement comes from the increase in the J_{SC}. The inclusion of the transparent conductive oxide MgZnO as an emitter to replace the traditional CdS emitter allows more photons near short wavelength region to enter the absorber. Alloying of CdTe to form the ternary alloy of CdSeTe to lower the optical band-gap ensures absorption of longer wavelength photons in the absorber. This improvement is consistent with the improvement of CdTe devices fabricated in labs around the world [47].

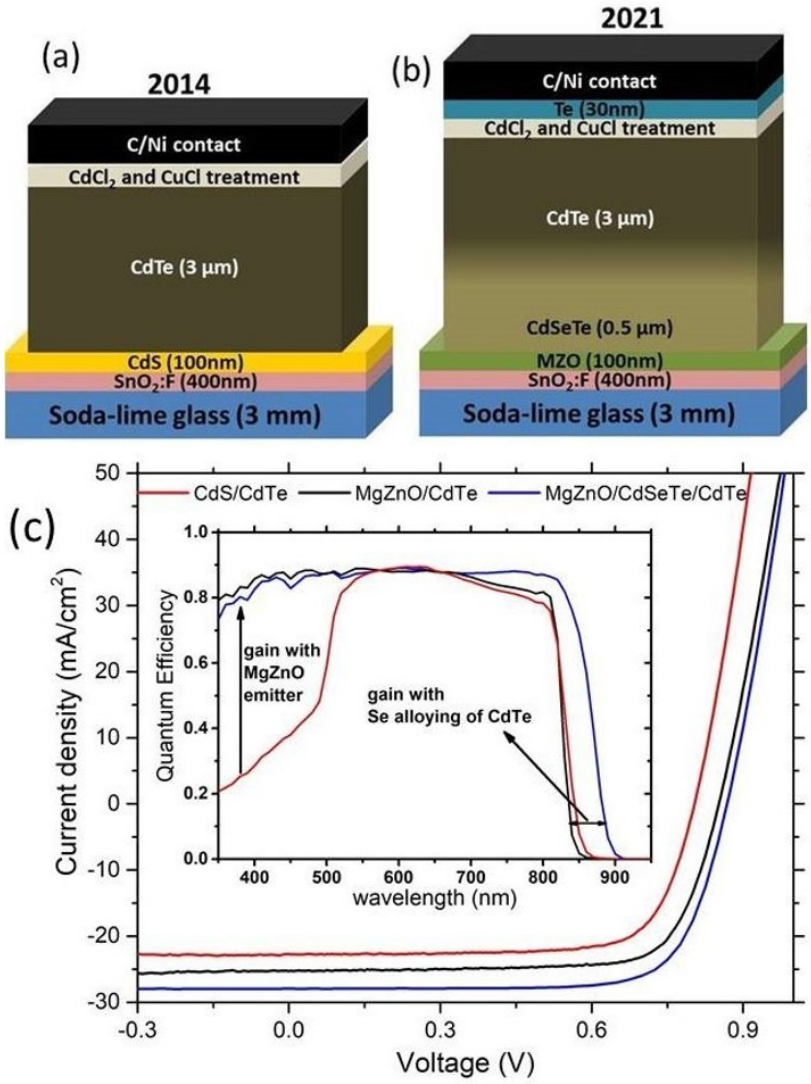

Figure 4.3: Improvement in CdTe TFSCs manufactured at CSU over the last 6 years [46].

Table 4.2: J-V parameters of progressively improved devices from Fig 4.3

Device stack	J_{SC} (mA/cm^2)	V_{OC} (mV)	FF (%)	$Eff.$ (%)
CdS/CdTe	21.7	808	74.7	13.7
MgZnO/CdTe	25.4	857	75.2	16.3
MgZnO/CdSeTe/CdTe	27.9	869	75.2	18.2

4.2.1 Alloying of CdTe with Se

The optimal band-gap for maximum photon absorption for the AM 1.5G spectrum with minimal loss due to thermalization is closer to 1.4 eV which is slightly less than that of polycrystalline CdTe [11]. The alloying of CdSe and CdTe to form a ternary alloy of

$CdSe_xTe_{1-x}$ has been exploited to tune the optical band-gap [48, 49, 50, 51, 52]. As seen in the quantum efficiency curve in the inset of Fig. 4.3, using a lower E_g absorber of CdSeTe between the typical emitter and CdTe aborber increases the photon absorption, primarily in the longer wavelength region that results in the improvement of J_{SC}. The added benefit of presence of the Se in the CdTe-based films is the improvement of the front emitter/absorber interface and the quality of the absorber with elongated minority carrier lifetimes [52, 53, 54, 55, 56, 57, 58, 59, 60]. While the method of deposition of the absorbers varies from closed space sublimation to simple evaporation and the absorbers are either a bilyaer of CdSe/CdTe or CdSeTe/CdTe, the critical $CdCl_2$ treatment done afterwards shows that there is a grading of the Se concentration within the absorber that grades the optical band-gap of the CdTe-based absorber [17, 52].

4.2.2 Alloying of MgO and ZnO to form $Mg_xZn_{1-x}O$ emitter

The purpose of the emitter adjacent to the polycrystalline CdTe absorber is to form a heterojunction. Typical properties of an emitter are wide optical band-gap and high lateral resistance. The wide optical band-gap allows more photons to enter the absorber and larger resistance will remedy potential shunting across the electrodes via pin holes. The typical n-type partner for CdTe has been CdS which has band-gap of about 2.4 eV. This makes it semi-transparent with parasitic losses only at shorter wavelengths as seen by the quantum efficiency curve in Fig. 4.3(c) . Other thin-film solar technologies including $Cu(In,Ga)Se_2$ (CIGS) and $CuInSe_2$ (CIS) have implemented wide band-gap emitters such as oxygenated CdS, ZnS(O,OH), InS(O,OH), ZnO-based emitters to mitigate the parasitic losses from the traditional low band-gap CdS emitter [61, 62, 63]. Similar strategy has been employed in CdTe technology where the ternary alloy of MgZnO has been used [46, 64, 65, 66, 67] as wide band-gap emitter that has led to increase in J_{SC} due to improvement in absorption of photons in short wavelength region of solar spectrum. The J-V parameters for MgZnO emitter from table 4.1 are superior in comparison to the ZnO only or MgO only emitter.

A detailed study to understand the physics that governs the photovoltaic performance of a CdTe-based TFSCs that employs MgZnO as emitter is the motivation for this chapter.

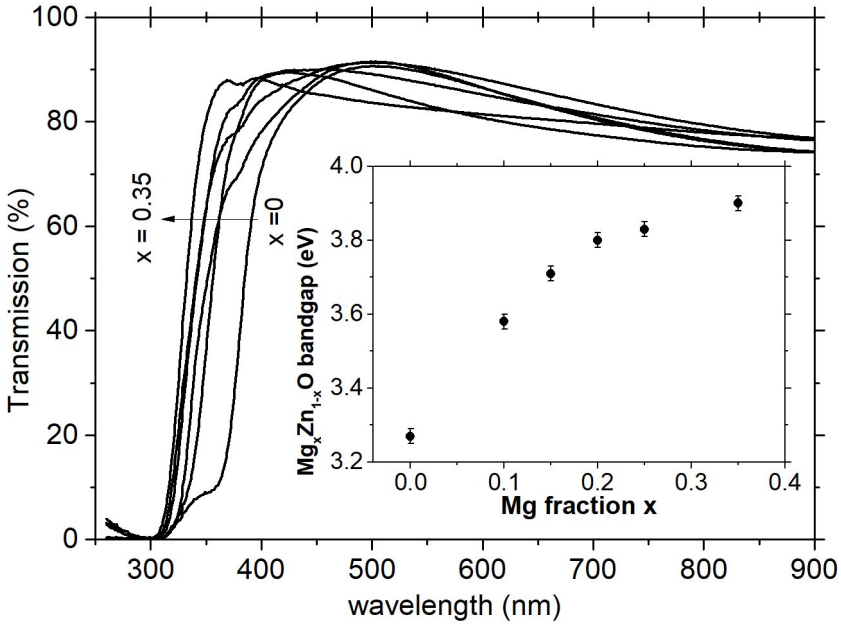

Figure 4.4: Improved optical transmission measurements with increasing Mg fraction in $Mg_xZn_{1-x}O$. The inset presents the optical band-gap measured using the Tauc method [46].

Variation in the atomic Mg fraction (x) in the $Mg_xZn_{1-x}O$ emitter controls the optical band-gap of the MgZnO film, where the Mg atomic fraction is given by x = Mg:(Mg + Zn). To study the optical band-gap as a function of variation in 'x', 100 nm thin films were sputter deposited on a soda lime glass with x = 0, 0.10, 0.15, 0.20, 0.25, 0.35. The presence of stated Mg fraction in the films was verified using the elemental X-ray photoelectron spectroscopy analysis. Optical transmission and reflection measurements were conducted using an UV-VIS photo spectrometer. The optical bandgap was then measured using the Tauc method [68] which is then plotted as function of Mg fraction in the Fig. 4.4. It is evident that the increasing Mg fraction in the MgZnO film widens the optical band-gap. ZnO has an optical band-gap measured to be 3.28 eV and the $Mg_xZn_{1-x}O$ band-gap varies between 3.58 eV to 3.9 eV as x is varied from 0.1 to 0.35, values that are consistent with previous studies [67, 69]. The transmission curves clearly show that higher Mg fraction in $Mg_xZn_{1-x}O$ will allow more photons in the short wavelength regions to enter the absorber.

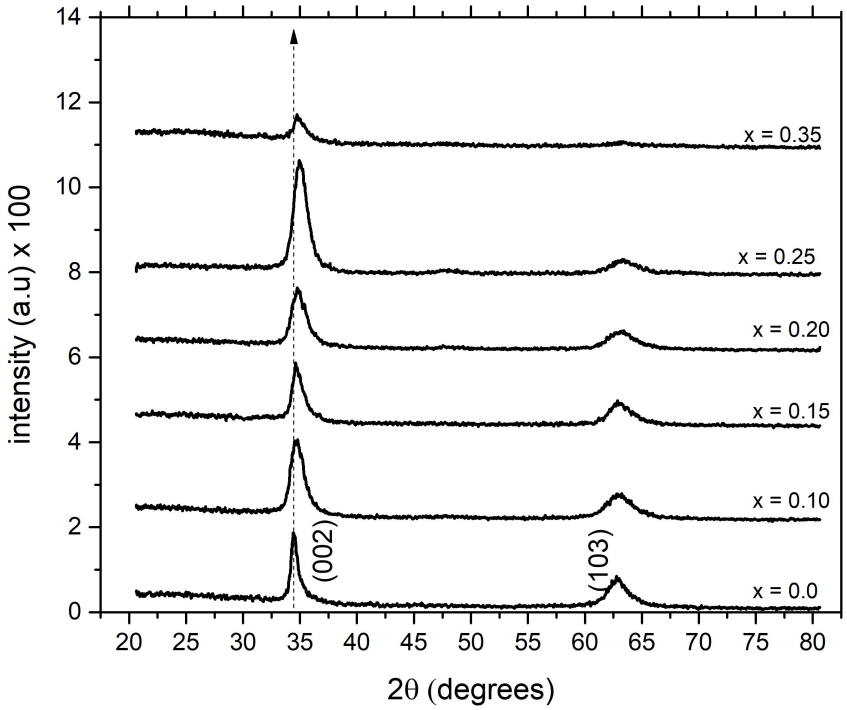

Figure 4.5: Glancing-angle XRD measured for $Mg_xZn_{1-x}O$ for varied x [46].

It is also important to focus on the structural changes in the $Mg_xZn_{1-x}O$. The primary constituent in the ternary alloy is ZnO, which has a wurtzite hexagonal structure with E_g = 3.2 eV, while MgO has a cubic zinc-blende structure with E_g = 7.7 eV [69]. Glancing-angle X-ray diffraction (GXRD) measurements using an X-ray wavelength of 1.54 $\AA$ from a Cu $K_{\alpha 1}$ source on the 100 nm films was conducted to study the structural changes in the film with variation in the Mg fraction. The inter planar spacing (d_{hkl}) between two planes with Miller index (hkl) is given by

$$d_{hkl} sin\theta = n\lambda \tag{4.1}$$

where $\lambda = 1.54$ $\AA$ is the X-ray wavelength, θ is diffraction angle. The planar spacing (d_{hkl}) obtained from this can be then used to find the lattice parameters 'a', 'b', and 'c' using the following equation,

$$\left(\frac{1}{d_{hkl}}\right)^2 = \frac{h^2}{a^2} + \frac{k^2}{b^2} + \frac{l^2}{c^2} \tag{4.2}$$

For a cubic structure, $a = b = c$ and for a hexagonal structure, $a = b \neq c$. A comparative GXRD for the different composition of Mg fraction in the $Mg_xZn_{1-x}O$ is presented in Fig.

Table 4.3: Critical parameters for linear fitting for Tauc plot in Fig. 4.4, calculated inter planar spacing and the lattice paramerers for XRD measurements from Fig. 4.5

$Mg_xZn_{1-x}O$	Optical	XRD-measurement						
x	E_g (eV)	$2\theta_{002}$	d_{002} ($\AA$)	c ($\AA$)	$2\theta_{103}$	d_{103}($\AA$)	a=b ($\AA$)	c/a
0.00	3.28	34.5°	2.597	5.19	62.88°	1.476	3.26	1.59
0.10	3.58	34.77°	2.578	5.15	63.02°	1.473	3.30	1.56
0.15	3.71	34.82°	2.574	5.14	63.1°	1.472	3.30	1.55
0.20	3.80	34.9°	2.568	5.13	63.18°	1.47	3.31	1.55
0.25	3.83	35.04°	2.558	5.11	63.39°	1.466	3.31	1.54
0.35	3.9	34.87°	2.570	5.14	-	-	-	-

.

4.5. There are two distinct peaks with Miller indices (002) and (103). The (002) peak is seen shifting to a larger diffraction angle with increasing Mg fraction while the (103) peak is decreasing in the intensity. The lattice parameters are calculated in the table 4.3 clearly indicates that there is a structural transition from a wurtzite to a zinc-blende at Mg fraction of x = 0.35. Similar structural changes has been reported in previous studies [70, 71, 72, 73, 74, 75].

4.3 CdTe-based solar cells with $Mg_xZn_{1-x}O$ emitter

CdTe-based TFSCs with MgZnO emitter as shown in Figs. 2.4 and 4.2 were fabricated, the only variation being the Mg fraction in the $Mg_xZn_{1-x}O$ emitter in the set of devices. J-V curves for the best performing devices for each case of 'x' is shown in Fig. 4.6 with the J-V parameters in table 4.4. It is evident that the Mg fraction in the MgZnO emitter has a

Table 4.4: J-V parameters of best devices with varying Mg fraction shown in Fig 4.6

Mg fraction (x)	J_{SC} (mA/cm^2)	V_{OC} (mV)	FF (%)	$Eff.$ (%)
0.00	27.2	738	62.8	12.6
0.10	27.9	849	74.0	17.5
0.15	28.1	856	76.8	18.5
0.20	27.6	861	77.4	18.4
0.25	27.9	841	73.9	17.3
0.35	26.8	777	60.8	12.7

significant effect on the over all device performance of CdTe-based TFSCs. The J_{SC} for the devices with different Mg fraction is comparable. The V_{OC} and FF improves significantly even with a slight introduction of Mg in the ZnO-based emitter as revealed by a comparison

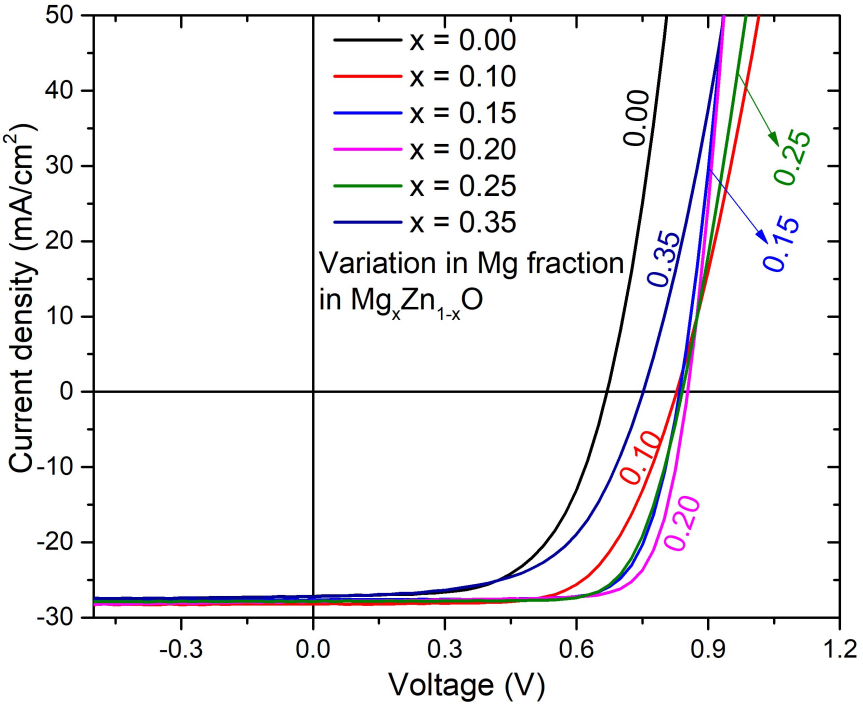

Figure 4.6: J-V plot of best performing cell with varying Mg fraction in $Mg_xZn_{1-x}O$.

between x = 0.00 and x = 0.10. The focus will be on identifying the key parameters that govern the fundamental mechanism behind such behavior.

4.3.1 J-V and QE measurement for $Mg_xZn_{1-x}O$ emitters

The box plot of J-V parameters of 25 small area solar cells with varying Mg fraction in MgZnO emitter fabricated under identical process parameters/conditions is presented below. A statistically significant systematic trend as a function of Mg fraction in $Mg_xZn_{1-x}O$ is observed. With variation in Mg from x= 0.00 to x = 0.10, there is boost in both V_{OC} and FF that leads to an improved efficiency. The V_{OC} continues to increase with Mg fraction, but drops significantly at x = 0.35. The range of the J-V parameters with inclusion of Mg in MgZnO is quite narrow with good uniformity across the 25 small-area solar cells. The FF is maximum at x = 0.15. The J_{SC} and V_{OC} between the various Mg fraction does not change significantly. The efficiency follows the trend of the FF, the efficiency is highest for

the optimal Mg fraction of x = 0.15 as tabulated for the average values of the J-V parameters in table 4.5

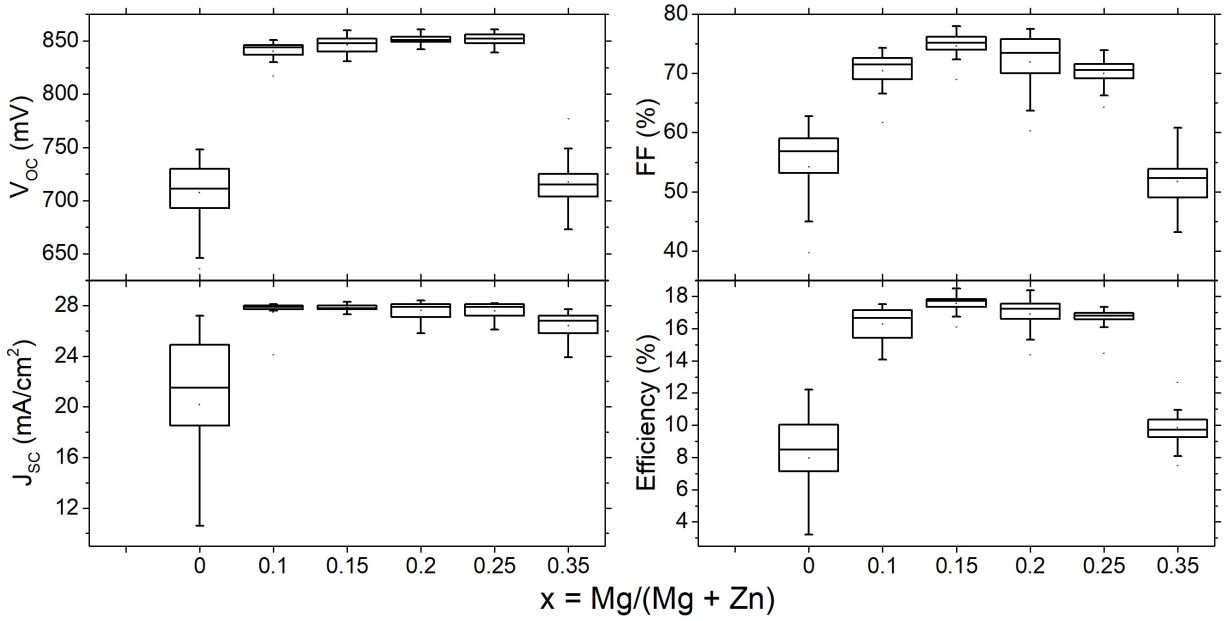

Figure 4.7: Box plot of J-V parameters of 25 solar cells with varying 'x' in $Mg_xZn_{1-x}O$ [46].

Table 4.5: Average J-V parameters and standard deviation of 25 devices with varying 'x'.

Mg fraction (x)	J_{SC} (mA/cm^2)	V_{OC} (mV)	FF (%)	$Eff.$ (%)
0.00	20.1 ± 6.2	707 ± 29.8	54.2 ± 7.0	8.0 ± 2.9
0.10	27.4 ± 1.0	840 ± 8.9	70.4 ± 3.2	16.3 ± 1.0
0.15	27.8 ± 0.2	846 ± 7.8	74.5 ± 2.5	17.5 ± 0.6
0.20	27.6 ± 0.7	851 ± 4.7	71.9 ± 5.1	16.9 ± 1.0
0.25	27.5 ± 0.7	851 ± 6.1	70.0 ± 2.5	16.4 ± 0.9
0.35	26.4 ± 1.1	717 ± 24.0	51.7 ± 4.4	9.8 ± 1.2

Fig. 4.8 shows a comparison of quantum efficiency responses from the devices with varying Mg fraction in the MgZnO emitter. The increase in the E_g of the $Mg_xZn_{1-x}O$ films with increasing Mg fraction discussed in previous section is consistent and verified by the the improved QE response in the lower wavelength region. The fraction of solar photons at low wavelengths is small, so there is no significant increase in the J_{SC} as seen in box plot in Fig. 4.7. However the introduction of a small fraction of Mg improves the other J-V parameters significantly.

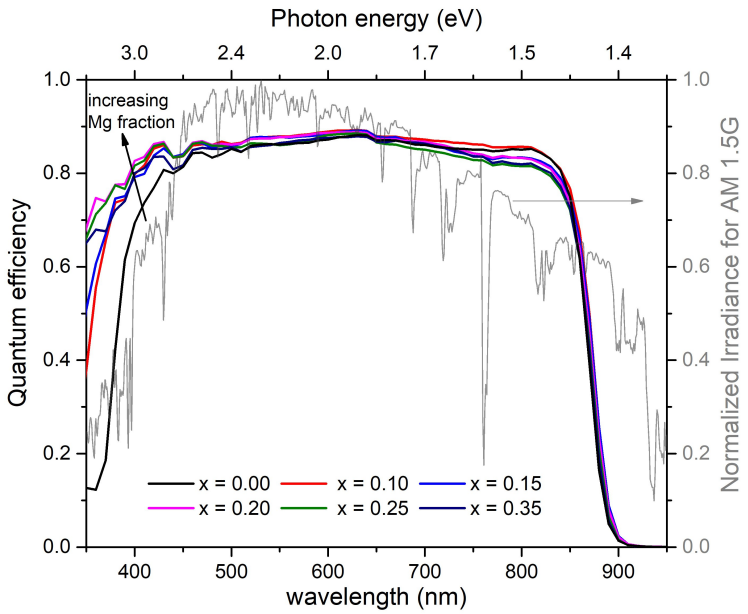

Figure 4.8: Quantum efficiency of CdTe-based solar cells with variation in the Mg fraction in the $Mg_xZn_{1-x}O$ emitter with the normalized AM 1.5G solar spectrum [46].

4.3.2 Energy band-offset between emitter and absorber

The optical band-gap widening in $Mg_xZn_{1-x}O$ can occur either due to the E_V moving further away or the E_C getting closer to the vacuum energy level. The implication of such bandgap widening in the MgZnO emitter will be on the energy band offset between the emitter and its adjacent semiconductor layers, primarily the emitter/absorber interface, one of the key parameters for the interface engineering. The energy band-offset between the emitter and the absorber plays significant role in the performance of CdTe-based TFSCs. The band-alignment between emitters like CdS and MgZnO with CdTe-based absorbers have characteristics of a Type II heterojunction discussed in earlier chapter. Such an alignment assures the extraction of the electrons in the E_C of the emitters and holes in the E_V of CdTe aborber side. The energy band-offsets, specially the conduction band offset (ΔE_C) between the emitter and absorber has been identified to play critical role in the performance of TFSCs liked CIS [62, 76] and CIGS [61, 77, 78, 79]. It can be varied from a flat band to a small positive spike the order of few tenth of an eV between the emitter and absorber, and it has been found to be effective to improve device performance according to various numerical

simulations [26, 66, 80, 81] and experiments [46, 64, 65, 66, 67] on CdTe-based thin film solar cells. A small positive ΔE_C will allow transport of photogenerated electrons in E_C through the thermionic emission transport, but it is effective to reduce the interface recombination velocity (S_{IF}) or to mitigate the effects of large S_{IF} by surface modifications, charging of defects, Fermi-level pinning, and favorable band-bending. This leads to an improved V_{OC} and FF in the devices [80, 81, 82, 83].

Fig. 4.4 from the previous section shows the optical band-gap widening in $Mg_xZn_{1-x}O$ as a function of Mg fraction. The optical band-gap widening occurs mostly from the E_C moving closer to the vacuum energy level in comparison to the E_V moving away from the vacuum energy level [84, 85, 86, 87]. The modulation of the relative position of E_C in MgZnO provides a knob to tune the ΔE_C at the interface between MgZnO emitter and CdTe-based absorber. To find the relationship between the optical band-gap widening and ΔE_C at the emitter/absorber interface experimentally, Kraut's method was used [88]. The method relies upon the measurement of photo-electron spectra to locate the valence-band edge and measuring the difference between the binding energy of the core levels and the valence band maxima to give a valence band offset (ΔE_V). In a MgZnO bulk, the major contribution to the valence band maxima comes from the $Zn_{2p3/2}$ and for CdTe-based absorber, the contribution to the valence band maxima comes from the $Cd_{3d5/2}$. Using a X-ray source, the photoelectron spectroscopy measurements was conducted to measure the ΔE_V at the MgZnO/CdSeTe interface as

$$\Delta E_V = \left(Zn_{2p3/2} - E_{VBM}\right)_{ZnO} - \left(Cd_{3d5/2} - E_{VBM}\right)_{CdSeTe} - \left(Zn_{2p3/2} - Cd_{3d5/2}\right)_{ZnO/CdSeTe} \tag{4.3}$$

where, $(Zn_{2p3/2} - E_{VBM})_{ZnO}$ and $(Cd_{3d5/2} - E_{VBM})_{CdSeTe}$ are the differences in $Zn_{2p3/2}$ in bulk ZnO and $Cd_{3d5/2}$ in bulk CdSeTe core levels and their respective valence band maxima. The $(Zn_{2p3/2} - Cd_{3d5/2})_{ZnO}$ measures the shift in the energy between the core levels at the ZnO/CdSeTe interface. X-ray photo electron spectroscopy measurement was conducted using $Al_{K\alpha}$ that produces X-ray photons of 1.486 keV energy. Three sets of sample specimen

that consist of 100 nm of oxide on a glass substrate, a 500 nm of CdSeTe on Tec glass and a bilayer of 500 nm of CdSeTe with a 2-nm oxide layer on top were prepared.

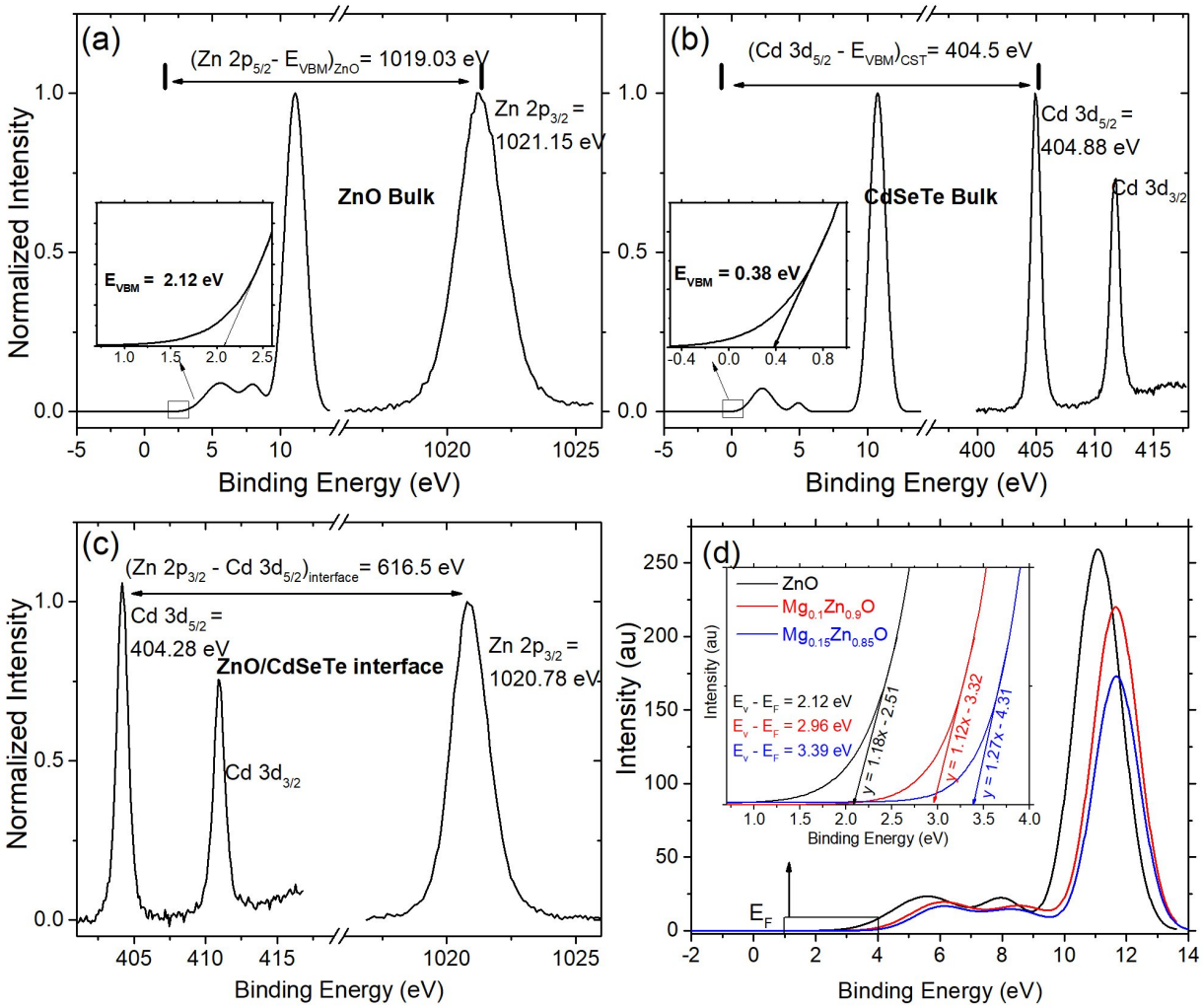

Figure 4.9: XPS spectra for various samples (a) VBM of ZnO bulk and binding energy of $Zn_{2p3/2}$ (b) VBM of CdSeTe bulk and binding energy of $Cd_{3d5/2}$ (c) Binding energy difference between the $Zn_{2p3/2}$ and $Cd_{3d5/2}$ at the ZnO/CdSeTe interface (d) VBM for $Mg_xZn_{1-x}O$ for x = 0.00, 0.10, 0.15

The Kraut's method was first introduced to measure the valence band offset between Ge and GaAs, a heterojunction formed between an elemental semiconductor and a binary semiconductor. To apply the Kraut's method to the ternary alloys of MgZnO and CdSeTe, two assumptions were made to measure the conduction band offset at the heterojunction formed between the $Mg_xZn_{1-x}O$ and the CdSeTe as follows:

- First assumption: In the ternary alloy of MgZnO and CdSeTe, the major contribution to the valence band comes from the core electrons of the dominant element in the alloy, which are Zn in the MgZnO and Cd in the CdSeTe.

- Second assumption: The optical energy bandgap can be used to calculate the conduction band offset from the electronic valence band offset measured by the Kraut's method as $\Delta E_C = \Delta E_V + E_{g,\ MgZnO} - E_{g,\ CdSeTe}$.

Table 4.6: ΔE_C between $Mg_xZn_{1-x}O$/CdSeTe for varied 'x' , and ratio of ΔE_C to ΔE_V in $Mg_xZn_{1-x}O$.

x	E_g (eV)	ΔE_g(eV)	ΔE_C:ΔE_V for $Mg_xZn_{1-x}O$				
-	-	-	3:2	5:3	**2:1**	7:3	3:1
-	-	-	ΔE_C at $Mg_xZn_{1-x}O$/CdSeTe				
0.00	3.28	0	-0.1	-0.1	**-0.1**	-0.1	-0.1
0.10	3.58	0.30	0.09	0.09	**0.11**	0.12	0.13
0.15	3.71	0.43	0.16	0.17	**0.19**	0.21	0.23
0.20	3.80	0.52	0.22	0.23	**0.25**	0.27	0.30
0.25	3.83	0.55	0.24	0.25	**0.27**	0.29	0.32
0.35	3.90	0.62	0.28	0.29	**0.32**	0.34	0.37

The difference between the binding energy of various core electrons has been measured in Fig 4.9 and a ΔE_V of 1.97 eV was measured using equation 4.3 which is in close agreement with reported values [89]. Based on the ΔE_V between the ZnO/CdSeTe interface and the E_g = 3.28 eV, a cliff-like ΔE_C = - 0.1 eV was calculated at the ZnO/CdSeTe interface.

This can be extrapolated to measure the ΔE_C at $Mg_xZn_{1-x}O$/CdSeTe interface for other values of 'x'. The optical band-gap widening of $Mg_xZn_{1-x}O$ with varying 'x' can be accounted with the relative change in the E_C and E_V in the MgZnO as a ratio of ΔE_C:ΔE_V in reference to the ZnO energy bands [86, 87]. Various ratios for ΔE_C:ΔE_V in $Mg_xZn_{1-x}O$ were used to account for uncertainty between the two band offsets. These ratios along with the second assumption were used to calculate ΔE_C at the $Mg_xZn_{1-x}O$/CdSeTe interface that are presented in table 4.6. A simple energy band position for the $Mg_xZn_{1-x}O$ with x = 0.00, 0.10, and 0.15 with reference to the CdSeTe is as shown in Fig. 4.10 for the ΔE_C:ΔE_V = 2:1 as highlighted in Table 4.6. It is evident that the introduction of Mg changes the ΔE_C from a cliff like to a spike like. This is consistent for all the ratios of ΔE_C:ΔE_V taken. The ΔE_C for

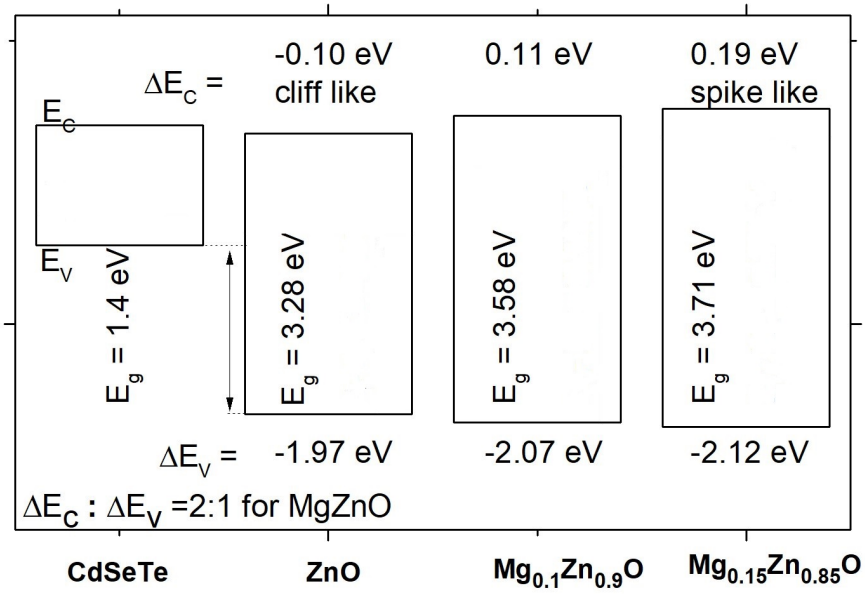

Figure 4.10: Relative energy band position of $Mg_xZn_{1-x}O$ with reference to CdSeTe

x = 0.15 is near 0.2 eV in any case, and this composition of MgZnO has the best photovoltaic performance as shown in the box-plots in Fig. 4.7. The conduction band offset starts to get larger with increasing 'x' and this is reflected in the reduced FF and the reduced efficiency in devices with Mg fraction greater than 0.15 [80, 81, 83].

4.3.3 Energy band bending and Interface passivation

As seen in Fig. 4.10, the conduction-band offset becomes more positive as the Mg fraction is increased. The band bending at the MgZnO/CdSeTe heterojunction is progressively increasing with Mg fraction in the MgZnO emitter as illustrated by energy band diagram at the MgZnO/CdSeTe interface generated by a SCAPS simulation based on the parameters from table 2.1 in Fig 4.11. The band offsets at the MgZnO/CdSeTe interfaceis based on the calculations in table 4.6 for ΔE_C:ΔE_V = 2:1. The band diagram clearly shows that for the optimal Mg fraction of x = 0.15, a favorable band bending occurs for the collection of electrons. A similar band bending occurs in the valence band region where the holes are effectively pushed away from the interface causing a large disparity in the electron and hole

concentration at the emitter/absorber interface leading to a low interface recombination [26].

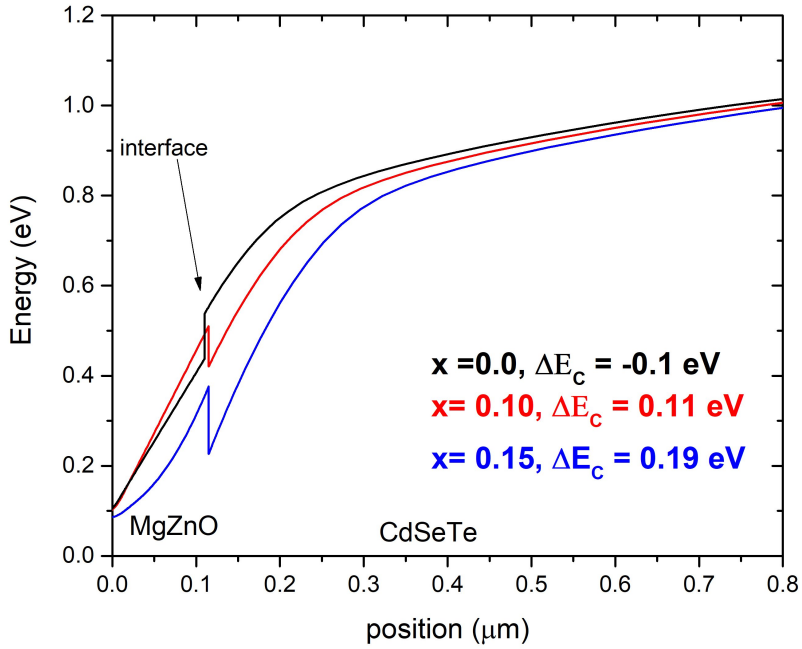

Figure 4.11: Simulated E_C at the MgZnO/CdSeTe interface for varied 'x' at 0 V [46].

Photoluminescence measurement was performed in the devices with different Mg fraction in MgZnO using a 520-nm photon source. A relative PL intensity for varied Mg fraction in the MgZnO emitter is presented in Fig. 4.12. The PL spectra corresponds near 880 nm (1.4 eV) which is the optical band-gap of CdSeTe absorber. The PL signal intensity is strong for the intermediate Mg fractions, but the PL signals for x = 0.00 and x = 0.35 are very low in comparison to the other Mg fractions. Such a trend is congruent to the trend observed in the V_{OC} in the Fig. 4.7 box plots.

A time resolved photoluminescence was conducted with 300-fs pulses using a Yb:KGW laser and an optical parametric amplifier for a 640-nm excitation wavelength and 1.1-MHz repetition rate. The emission spectra was collected with a 44-nm bandpass filter centered at 819 nm with time-correlated single-photon counting. The spectral photoluminenscence decay for the different samples is plotted in Fig. 4.13. It clearly shows that the fastest decay rates occur for x = 0.00 and x = 0.35. These Mg fraction samples had the smallest PL intensity and lowest V_{OC}. This is consistent with the other measurements that clearly show

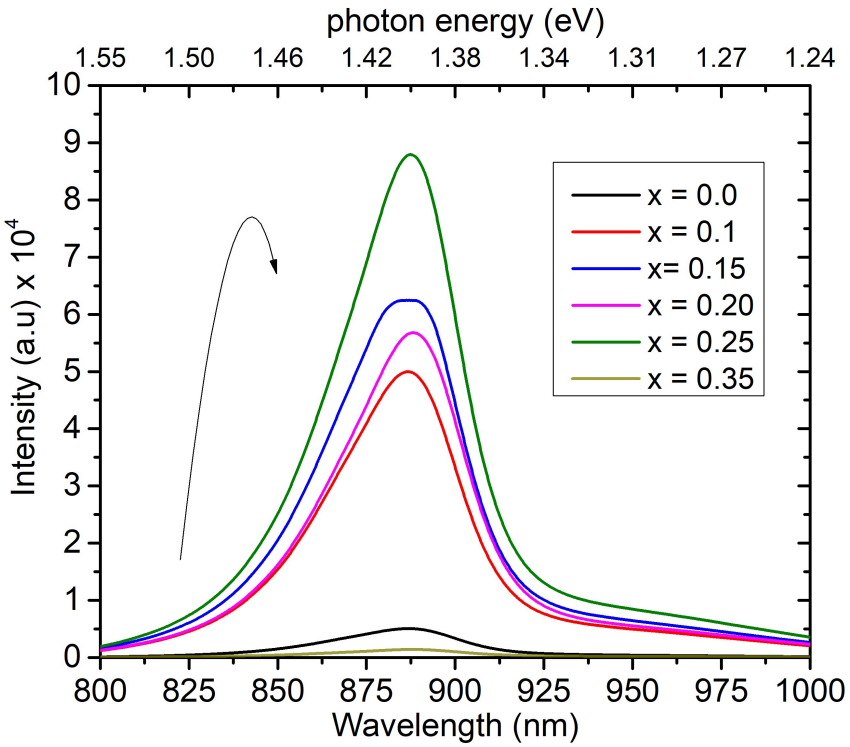

Figure 4.12: PL measured for devices with various Mg fraction in MgZnO [46].

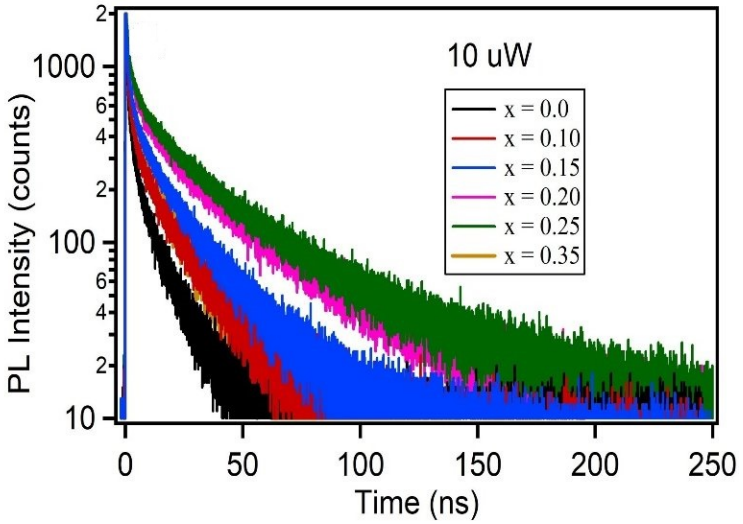

Figure 4.13: TRPL decay for devices with various Mg fraction in $Mg_xZn_{1-x}O$. Fastest decays observed for x = 0 and 0.35. [46].

that the incorporation of Mg helps improve the front interface, but there is an upper limit to the Mg fraction in the MgZnO as suggested by low J-V parameters, small PL intensity and fast PL decay for Mg fraction at x = 0.35.

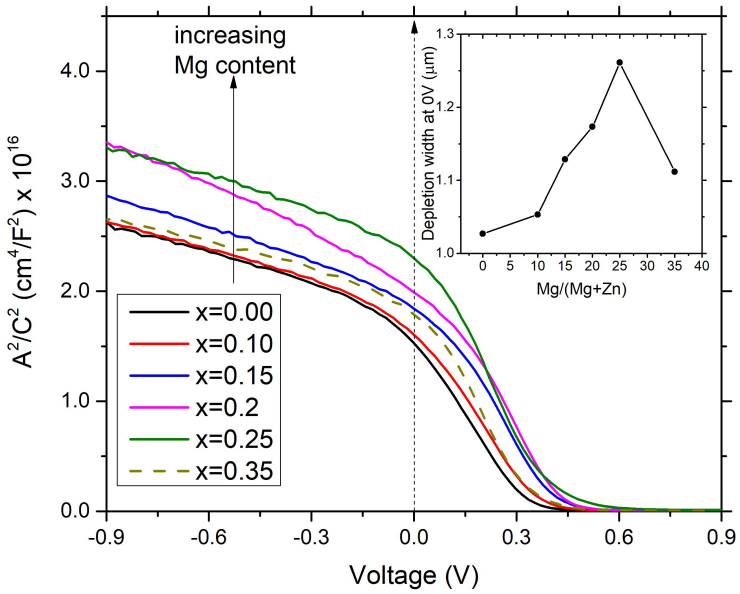

Figure 4.14: Mott-Schottky plot from C-V measured for different Mg fraction. Inset shows the variation in depletion width at 0 V.

Capacitance-Voltage measurement was carried out on the same samples. The depletion width derived from the C^{-2} vs. V in the Mott-Schottky plots at 0 V for the devices clearly shows that there is an increase in the depletion width with increasing Mg fraction. An increase in depletion width can be associated with the increase in band-bending in the emitter/absorber heterojunction. Such band-bending will extend the depletion width deeper into the absorber and creates a larger built-in potential, which should yield a larger V_{OC}. This is consistent with the decay rate and intensity of the PL emission and the monotonic increase in the V_{OC} box-plots with increasing Mg fraction except for the case of x = 0.35, most likely due to the upper limit coming to an effect, coupled with the transition from a wurtzite to a zincblende structure in the MgZnO.

Current-voltage measurements were extended to lower temperatures on two devices, one without Mg in the emitter and the other with optimal Mg fraction of x = 0.15. The devices in Fig. 4.15(a) with no Mg in the emitter (x = 0.0) shows large distortions in the J-V curves at lower temperatures whereas such distortions are smaller and only observed at the lowest temperatures for the optimal Mg fraction in Fig. 4.15(b). The V_{OC} plotted against the temperature in Fig. 4.15(c) shows that the V_{OC} for both cases progresses at typical rate

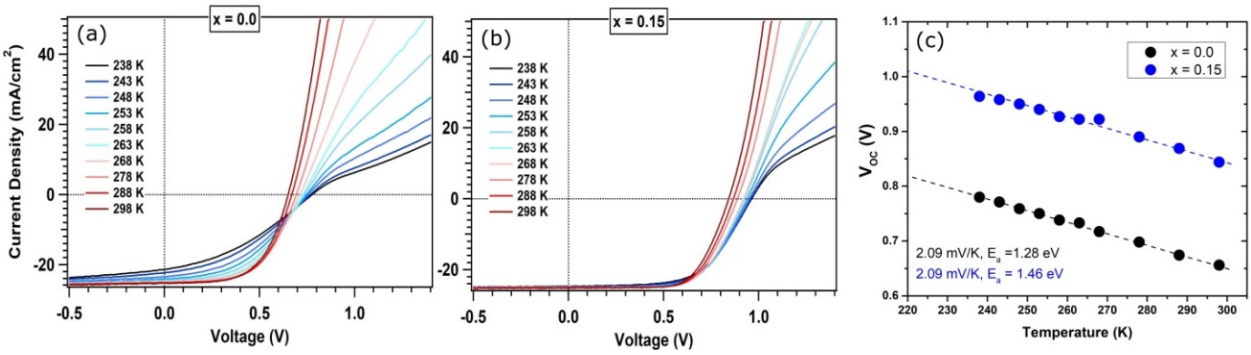

Figure 4.15: Low Temperature J-V curves for (a) x = 0.00 and (b) x = 0.15. (c) V_{OC} versus temperature with fitted parameters [46].

of 2.09 mV/K. The extrapolated activation energy for the optimal Mg fraction is 1.46 eV which is close to E_g of CdTe-based absorber in comparison to the 1.28 eV for the emitter without Mg. Thus, ΔE_C near 0.2 eV for the optimal Mg fraction is not large enough to have negative effect on the device performance within any reasonable operating temperatures of solar cells.

4.4 J-V distortion in CdTe solar cells with $Mg_xZn_{1-x}O$ emitter

Distortions that are sometimes observed in J-V curves even with optimum Mg fraction can be a simple failure to superimpose between the light and dark curve [83, 90] referred to as a 'crossover' or distortion of the light curve in the power quadrant, often called 'kinks', or in the first quadrant referred to as the 'roll over' [30, 66]. These distortions can be more pronounced when the solar cell is measured with filters that eliminate photons of certain wavelengths [62, 63]. In this section, we will discuss such distortions, their origin in MgZnO employed CdTe-based solar cells, their characteristics and methods that can be employed to eliminate such distortions.

4.4.1 Effect of Mg fraction on J-V distortion

A direct effect of replacing the traditional CdS emitter with MgZnO can be observed in the J-V characteristics. This improved the J-V parameters overall, but distortions from

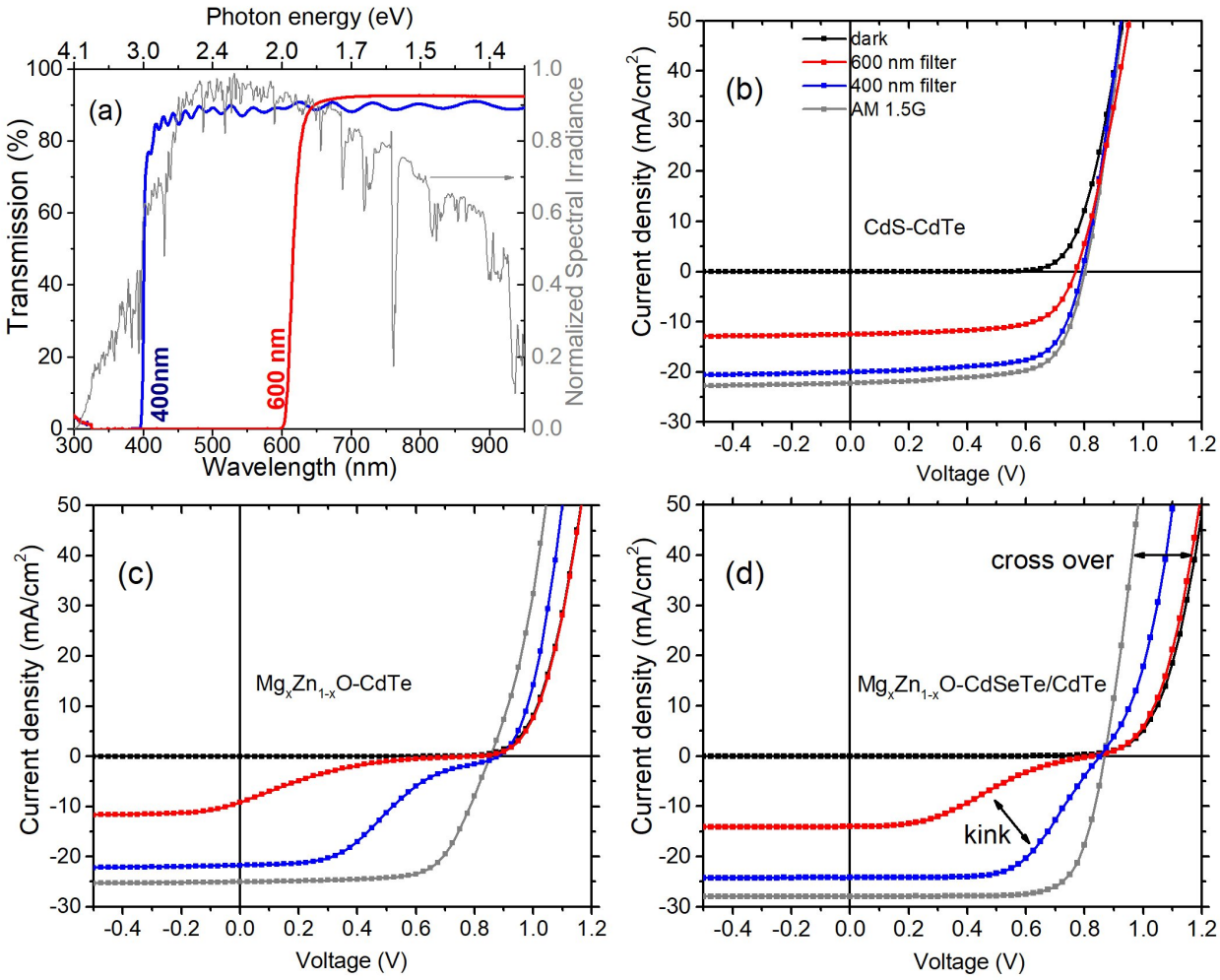

Figure 4.16: (a) Transmission of two filters in reference to normalized AM 1.5G spectrum. (b)-(d) J-V measurements for various illumination conditions for CdS-CdTe, $Mg_{0.25}Zn_{0.75}O$-CdTe and $Mg_{0.25}Zn_{0.75}O$-CdSeTe/CdTe respectively [20].

normal J-V characteristics are sometimes observed for MgZnO employed CdTe-based solar cells as shown in Fig. 4.16. To test the influence of photon spectrum, and the J-V shape, two filters were used to block short-wavelength photons as shown in Fig. 4.16(a). A 400-nm long-pass filter eliminates most of the u-v and low wavelength blue photons , and the 600-nm filter cuts off all photons of wavelength below 600 nm. The traditional CdS-CdTe devices are well behaved; they do not exhibit any crossover between the light and dark curves, and, they do not exhibit distortions in J-V measurements under filtered illumination shown in Fig. 4.16(b). However, with the wide band-gap emitter of $Mg_{0.25}Zn_{0.75}O$, the devices with CdTe only and with the bilayer of CdSeTe/CdTe do show distortions in the filtered

curves and crossover between light and dark curves in Figs. 4.16(c) and (d). The 600-nm filter produced larger distortion than 400-nm filter and the J-V parameters for various illumination conditions are presented in table 4.7.

The filtered measurements show a change in the J_{SC}proportional to the reduction in photons. The fill factor for CdS was unchanged, but with MgZnO, it was reduced significantly. The huge reduction in cell efficiency primarily due to reduced fill factor under the 400-nm filter for the MgZnO emitter suggests that the MgZnO film is sufficiently resistive that absorption of high-energy blue photons is central in improving the conductivity in the MgZnO and for the normal operation of devices with the MgZnO emitter. Such characteristics is referred to as 'photodoping' which will be discussed in more detail in next section with light soaking experiments.

Table 4.7: J-V parameters for CdTe-based solar cells in Fig. 4.16 measured under various illumination conditions.

	J_{SC} (mA/cm^2)	V_{OC} (mV)	FF (%)	$Eff.$ (%)
	Under AM 1.5G			
CdS/CdTe	22.2	801	68.3	12.1
MgZnO/CdTe	25.0	854	677	14.4
MgZnO/CdSeTe/CdTe	27.9	869	75.2	18.2
	Under 400 nm filter			
CdS/CdTe	20.0	792	68.1	10.8
MgZnO/CdTe	21.8	880	35.6	6.8
MgZnO/CdSeTe/CdTe	24.2	852	59.9	12.3
	Under 600 nm filter			
CdS/CdTe	12.5	769	65.4	6.3
MgZnO/CdTe	9.2	814	13.2	1.0
MgZnO/CdSeTe/CdTe	14.0	829	32.6	3.8

A simple crossover between light and dark curves for three different Mg fractions of x = 0.00, 0.20 and 0.25 is presented in Fig. 4.17. A progressively larger crossover is observed. Such a crossover is signature of a spike behavior of considerable height caused by a large conduction band offset ΔE_C, often referred to as secondary barriers [83, 90]. A simple thermionic emission for electron current at a heterojunction [12] is given by

$$J_n = \int_{E_{Fn}+\phi}^{\infty} q v_x dn \approx A^* T^2 \exp^{-\frac{\phi}{kT}} \tag{4.4}$$

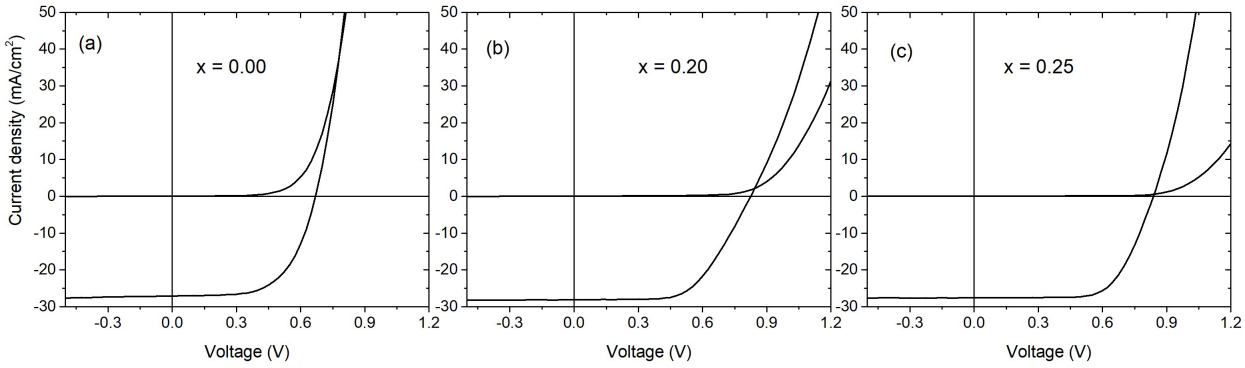

Figure 4.17: Cross over between the light and dark curves for MgZnO/CdSeTe/CdTe devices with different Mg fractions in MgZnO.

where J_n is electron current density, q is electronic charge, v_x is carrier velocity in direction of transport, dn is change in electron density, A^* is effective Richardson constant, T is absolute temperature, k is Boltzmann constant and $\phi = E_C - E_{Fn}$, is effective barrier height for electrons measured between the conduction band in emitter and electron fermi position at absorber side at the emitter/absorber interface. A progressive increase in this barrier height with increasing Mg fraction according to the measurements in Fig. 4.10 is the cause for the discrepancy in superposition of dark and light curve [90].

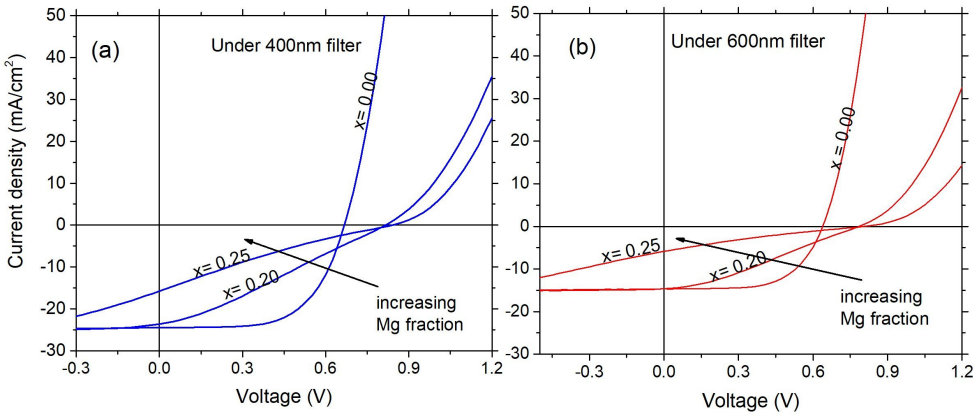

Figure 4.18: Distortion in the filtered light curves with different Mg fractions in MgZnO.

A larger Mg fraction means a larger ϕ that impedes the transport of the electrons. Under illumination, some of the external voltage will be dropped at the emitter/absorber interface to lower the barrier for the efficient electron transport, this causes the turn on voltage to be lower than that for a dark curve which leads to the failure of superposition of dark and light

curves, giving rise to a typical cross over. Increasing ϕ leads to larger cross overs as seen with increasing Mg fraction in Fig. 4.17. The effect of increased ϕ is evident in the filtered light curves shown in Fig. 4.18. There is no distortion in filtered curves for lower-voltage cells with ZnO (x = 0.00) similar to the CdS emitter but the filtered curves develop distortion for x = 0.20 and even more for x = 0.25.

4.4.2 Cause of J-V distortion

J-V distortions identical to the ones for MgZnO devices shown in Fig. 4.16 have been reported previously for other TFSCs like CIS and CIGS [62, 63, 91, 92] when a wide band-gap emitter is employed. J-V distortion in MgZnO/CdTe devices referred as S-kink behavior has also been reported [66]. The general consensus here is that the presence of acceptor type defects in the wide band-gap emitters which compensate the n-type property of the emitter. In dark or absence of blue photons, these acceptor type defects are occupied with electrons that reduces the n-type behavior of an emitter. Under full illumination with the solar spectrum, these acceptor type defects become unoccupied and release electrons after the absorption of short-wavelength (blue) photons as depicted in Fig. 4.19(a) that improves the n-type conductivity in the MgZnO emitter.

In simple words, the population of the occupied acceptor-type defects is larger in the dark than under illumination of full AM 1.5G spectrum. The presence of such acceptor-type defects has been reported in ZnO films which is the primary oxide in the ternary MgZnO alloy [93, 94, 95]. A SCAPS numerical simulation was carried out with variation in density of such occupied neutral acceptor type defects (N_t) in the MgZnO emitter. An N_t of 2.0×10^{16} cm^{-3} was chosen to simulate the dark and 600-nm filter J-V curves, reduced to 1.6×10^{16} cm^{-3} for 400-nm filter J-V curve, and to 1.2×10^{16} cm^{-3} for the full solar spectrum. The choice of energetic position of such defects was 0.2 eV and 1.2 eV above the E_V to complement their double acceptor type nature [93, 94]. Other critical parameters are listed

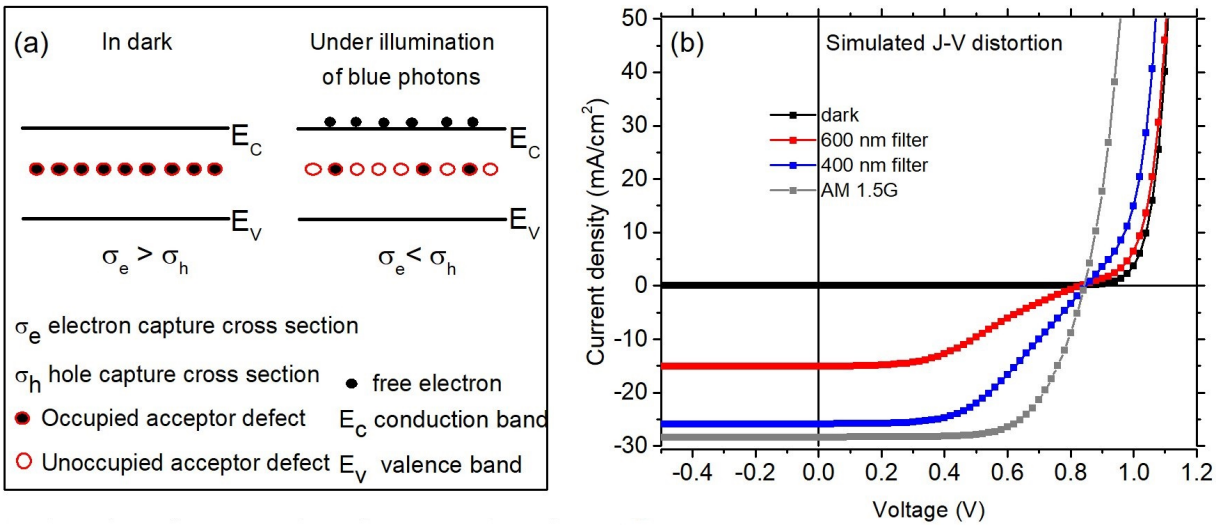

Figure 4.19: (a) Schematic of the occupation and release of the electrons from the acceptor type defect states in dark and with blue photons in a wide band-gap emitter (b) Simulated J-V distortions under various illumination conditions [20].

in table 2.1. The simulated J-V curves plotted in Fig. 4.19(b) have similar features to the J-V curves of CdTe-based devices with MgZnO emitter, measured under different illumination conditions in Fig. 4.16.

Table 4.8: J-V parameters for experimentally measured and simulated CdTe-based solar cells under various illumination conditions.

	J_{SC} (mA/cm^2)	V_{OC} (mV)	FF (%)	$Eff.$ (%)
Time (min)	Experimental light curves			
0	28.4	843	62.0	14.8
1	28.4	842	65.2	15.6
5	28.4	840	67.6	16.1
15	28.5	839	69.6	16.6
30	28.4	835	70.8	16.8
60	28.4	832	72.2	17.1
N_t ($\times$ 10^{16} cm^{-3})	Simulated light curves			
1.5	27.8	845	60.3	14.2
1.3	27.8	844	65.1	15.3
1.2	27.8	843	67.3	15.8
1.1	27.8	842	69.4	16.2
1.0	27.8	841	71.4	16.7
0.9	27.8	841	73.2	17.1

J-V measurements were conducted on the same devices at regular interval during a prolonged illumination of AM 1.5G to study the time-scale of the photogeneration in MgZnO commonly known as light-soaking and the recovery of the devices in dark. A numerical simulation was carried out to generate light and dark J-V curves with variation in the density

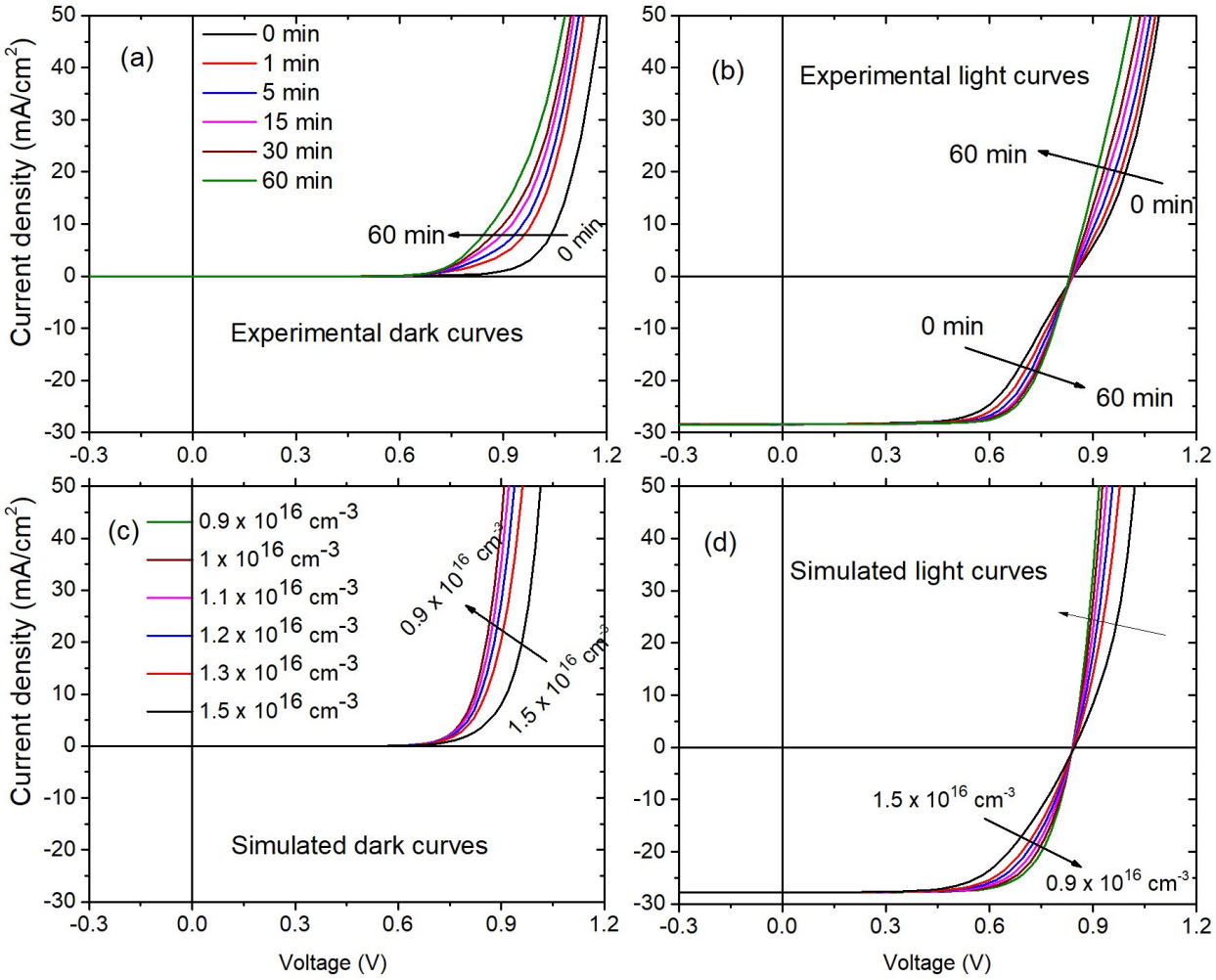

Figure 4.20: (a)-(b) Light and dark J-V curves measured at various interval during light soaking (c)-(d) Simulated light and dark J-V curves generated by varying the occupied acceptor defects (N_t) in MgZnO (x = 0.20).

of occupied N_t in the MgZnO. The J-V parameters for the experimental and simulated light curves are tabulated in table 4.8 and the experimental and simulated curves are plotted in Fig.4.20. Both simulated and experimental dark curves show similar features, the turn-on voltage in the dark shifts to a lower value with increased illumination time as additional acceptor-type defects become unoccupied, releasing electrons and increasing the conductivity in the MgZnO. The J-V parameters for experimental and simulated light curves show improvement in the conversion efficiency due to improvement in the fill factor. This shows that the photogeneration in MgZnO is a relatively slow process that can contribute to the irregularities in the cell measurements.

4.4.3 Remedy for J-V distortions by Ga-doping of MgZnO

A good take from last section is the need to employ a more reliable method such as extrinsic doping of the MgZnO to increase the n-type carrier concentration rather than relying on the photogeneration of electrons in the emitter by absorption of high energy photons. The undoped MgZnO is a relatively high resistance transparent oxide [64] with n-type carrier density the order of 10^{14} cm^{-3} [67]. Extrinsic Ga-doping of MgZnO has been investigated to improve the n-type carrier concentration in the MgZnO [96, 97, 98, 99].

In previous section, we discussed that J-V distortions in MgZnO emitters and how it becomes progressively severe for more than the optimal Mg fraction of x = 0.15. In this section, we demonstrate that the Ga-doping of MgZnO even with high Mg fraction (x = 0.25) can remedy the J-V distortions. Two separate sputter targets with composition of $Mg_{0.25}Zn_{0.75}O$ and $Mg_{0.25}Zn_{0.73}O{:}Ga_{0.02}$ were used to sputter-deposit 100 nm of emitter for the CdTe-based solar cells. Two sets of CdTe-based TFSCs were then fabricated using these 100-nm of undoped MgZnO and MgZnO:Ga as emitter under identical conditions and process parameters as discussed in section 2.5. More information can be found in Ref. [20].

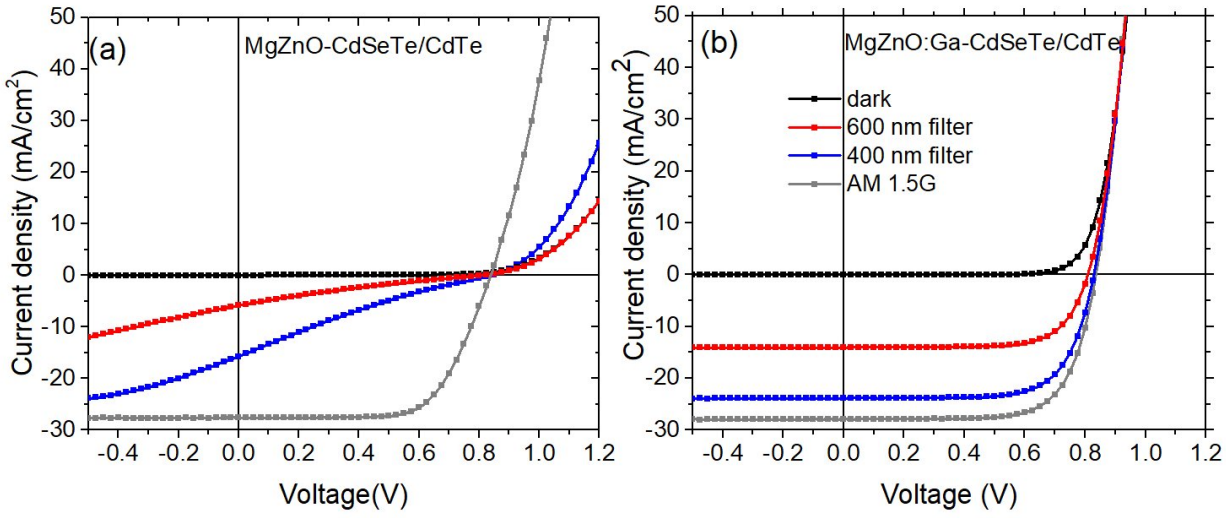

Figure 4.21: Comparison of J-V curves measured under different illumination conditions for CdTe-based solar cells with (a) undoped MgZnO emitter (b) Ga-doped MgZnO [20]. (Both sets of cells had Mg fraction x = 0.25)

The Ga-doping of MgZnO emitter eliminated the kink from the J-V curves measured under filtered light and did not show any crossover between the light and dark curves in comparison to the undoped MgZnO emitter. This suggests that the carrier density in the Ga-doped MgZnO emitter is sufficiently high and the dependence on photogeneration of electrons is eliminated. This effectively demonstrates that extrinsic doping of MgZnO can be achieved to improve the n-type carrier concentration. The Mg fraction of x = 0.25 is closer to the upper limit for effective dopant activation. Appropriate fractions of Mg, Zn and Ga to maintain an optimal ΔE_C and high carrier concentration [99] are the keys to elimination of the J-V distortion.

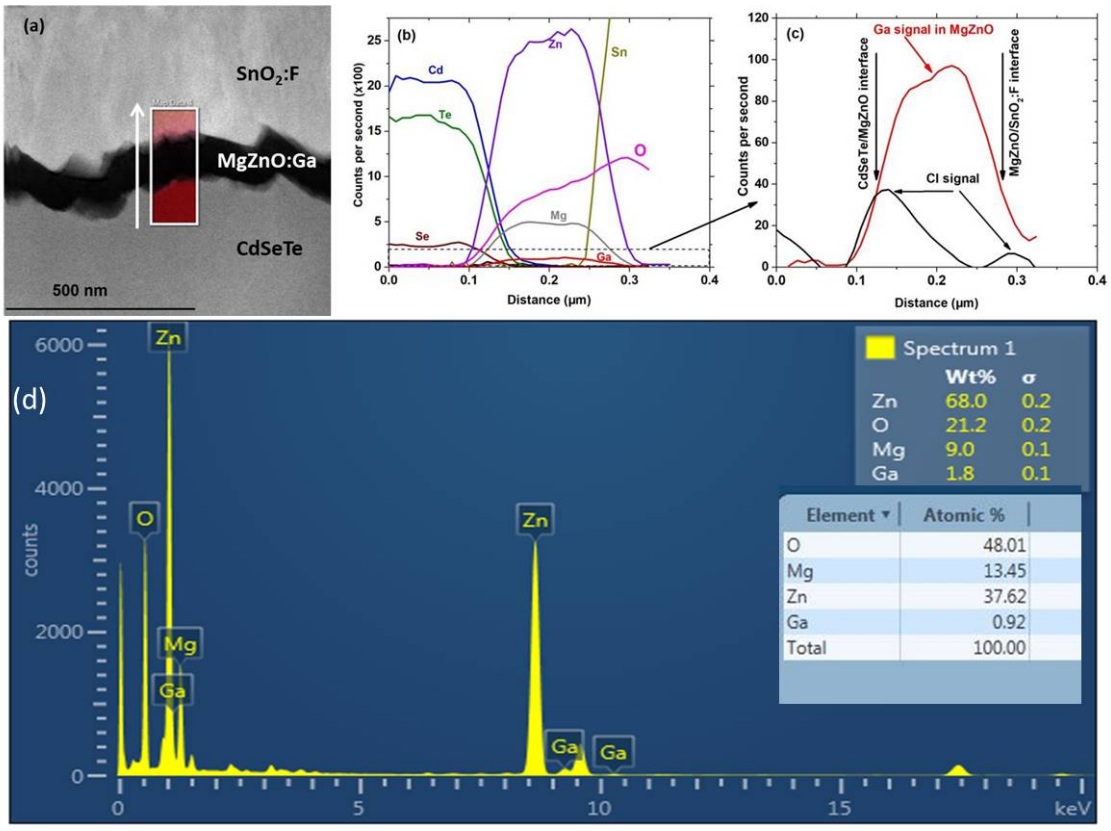

Figure 4.22: (a)High angle annular dark field STEM image of a MgZnO:Ga/CdSeTe interface. (b) Intensity profile of elemental distribution measured by energy-dispersive X-ray spectroscopy (XEDS) in direction of arrow in (a). (c) Expanded scale to highlight the Cl and Ga signals (d) XEDS signals for various elements [20]. (*measured at University of Illinois Chicago)

High resolution Transmission Electron Microscopy (TEM) measurements were carried out at University of Illinois Chicago (UIC) on the Ga-doped MgZnO device. An elemental

analysis at the MgZnO/CdSeTe interface shows the expected ratios of the elements for Cd, Se and Te in the absorber. The Ga signal tracks with the Zn and Mg signals, and no significant diffusion of elements at the interfaces was observed. The presence of Cl at the MgZnO/CdSeTe and MgZnO/SnO_2:F interfaces, however, was detected. The Cl is presumed to have diffused via the grain boundaries during the $CdCl_2$ treatment done on a CdTe surface about 3.5 μm from the emitter. The elemental ratios of Mg, Zn, O and Ga measured in the MgZnO:Ga region with the energy dispersive X-ray spectroscopy (XEDS) verify the elemental ratios to be close to the expected value within the limit of error.

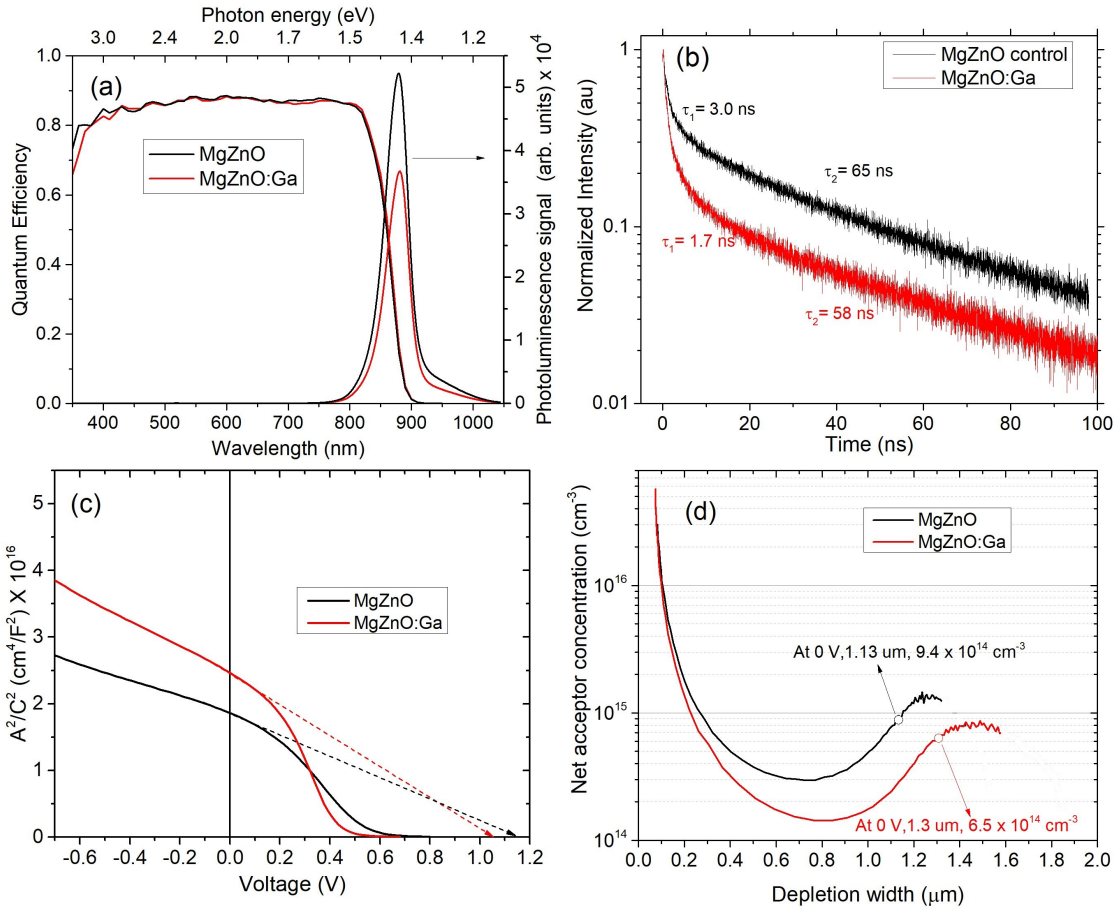

Figure 4.23: Comparison of undoped and Ga-doped MgZnO (a) QE and PL measurement (b) TRPL measurement (c) Mott-Schottky plots (d) Carrier-density vs. depletion-width plot.

A comparison of QE and PL spectra shows only minor differences between the doped and undoped MgZnO emitters. The band edge from QE and the PL emission spectra align at 1.43 eV in both cases. TRPL comparison shows that the τ_1 lifetime, which measures the

effective interface recombination lifetimes, is 1.7 ns for Ga-doped MgZnO, slightly lower than the 3.0 ns measured for undoped MgZnO. The bulk recombination lifetimes measured by τ_2 are not significantly different for doped and undoped MgZnO emitter. The built in potential derived from the Mott-Schottky plot is around 1.1 V, the Ga-doped has slightly lower than the undoped case. The carrier density Vs. depletion width shows that the carrier density of absorber is the order of 10^{14} cm^{-3} at the belly and comparable depletion width at 0 V.

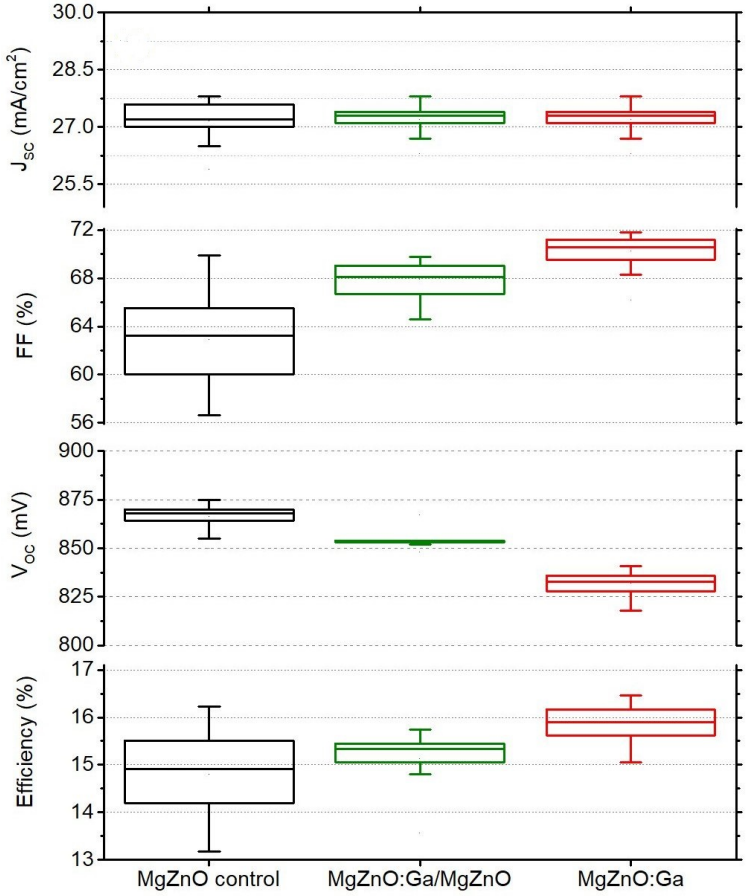

Figure 4.24: Box plot of J-V parameters for 25 small area solar cells with 100-nm undoped MgZnO, bilayer of 100-nm undoped and 20-nm Ga-doped MgZnO, and 100-nm Ga-doped MgZnO emitter layer [20].

A comparative box plot of J-V parameters is shown in Fig. 4.24 which shows that the Ga-doped MgZnO emitter produces a better efficiency than the undoped MgZnO. The majority of the improvement in efficiency comes from an improved fill factor but there is a slight loss of V_{OC}. The small built in potential and small interface recombination lifetimes

measured for Ga-doped emitter devices earlier are in agreement with the low V_{OC}. The improvement in the J-V parameters strongly suggest that the advantage outweighs any negative impact. Interestingly, if a thin 20 nm of undoped MgZnO is introduced between the Ga-doped emitter and CdSeTe absorber, majority of the V_{OC} loss can be recovered suggesting the MgZnO/CdSeTe provides a better interface than the MgZnO:Ga/CdSeTe interface. The results here demonstrate that the extrinsic Ga-doping of MgZnO emitter will rectify the J-V distortions and yield better efficiency conversion in the CdTe-based solar cells.

4.5 Emitter doping

The Ga-doping of MgZnO has paved a path for implementing the highly doped emitter for CdTe-based solar cells. The devices with Ga-doped MgZnO emitter had better conversion efficiency along with rectification of the J-V distortions under various illumination conditions. In this section, we exploit the SCAPS numerical simulation to explore the benefits of doping emitter in addition to variation in other parameters like doping in the absorber, interface recombination velocity at emitter/asborber interface, and bulk recombination lifetimes in the absorber.

The V_{OC} for polycrystalline CdTe-based solar cells have stagnated below 900 mV. A voltage deficit of around 200 mV is observed for CdTe solar cells in comparison to the GaAs for similar E_g. This has been attributed due to low bulk recombination, and low carrier density in the absorber [100]. The polycrystalline nature of the CdTe thin film makes the grain boundaries an effective recombination centers that reduce the recombination lifetimes in the absorber. The $CdCl_2$ treatment and alloying of CdTe with Se helps grade the Se and passivate these grain boundaries [17, 18, 19, 52, 53, 54, 56, 101], enhances carrier collection [50], and enables high minority carrier recombination lifetimes the order of hundreds of ns [55, 57, 59, 60]. The group-V dopants employed to improve the hole carrier concentration in the CdTe has yielded the carrier concentration the order of 10^{16} cm^{-3} [26, 102, 103, 104, 105]

but the V_{OC} in the polycrystalline CdTe has still not crossed the 900 mV mark without significant reduction in fill-factor.

4.5.1 Emitter and absorber carrier densities

With large lifetimes and carrier concentration possible in the CdTe-based absorber, the V_{OC} has still has not improved. Design strategies to increase the V_{OC} of CdTe-based solar cells has focused on efficient charge extraction. The discussions in earlier sections have shown that the emitter/absorber interface plays key role in the performance of CdTe-based TFSCs.

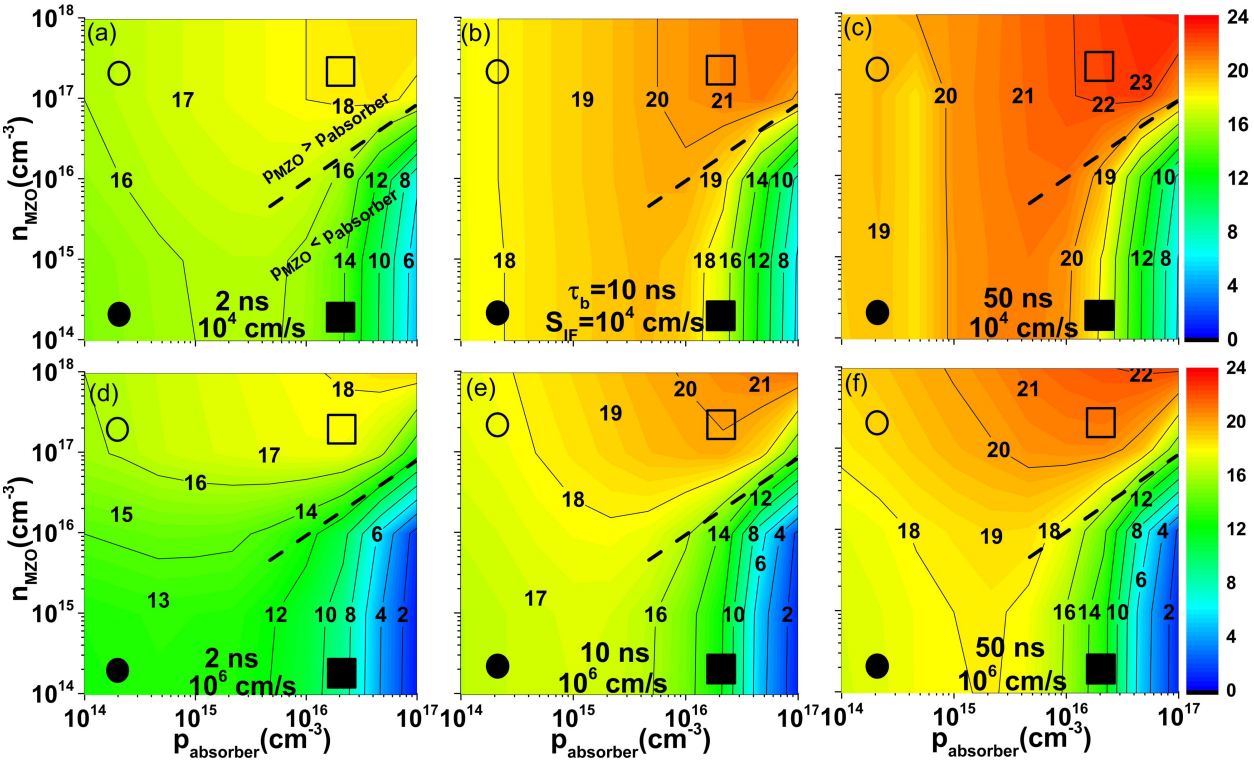

Figure 4.25: Efficiency contour plot with varied carrier concentration in the MgZnO emitter and absorber, for recombination lifetimes of 2, 10, and 50 ns for S_{IF} = 10^4 and 10^6 cm/s [26].

Numerical simulations wre carried out where the carrier concentration in the emitter and absorber was varied along with bulk recombination lifetimes in the absorber (τ_b), and interface recombination (S_{IF}) at the emitter/absorber interface. The ΔE_C was set to 0.2 eV and other key parameters simulation are listed in table 2.1. Fig. 4.25 presents a comprehensive

picture of efficiency calculated with variation in the carrier concentration of MgZnO emitter (n_{MZO}) between 10^{14} - 10^{18} cm^{-3}, absorber carrier concentration ($p_{absorber}$) between 10^{14} - 10^{17} cm^{-3} for three different absorber recombination lifetimes of 2, 10, 50 ns and for two S_{IF} of 10^4 and 10^6 cm/s. A distinct feature is observed in each of the six plots where four points are highlighted with

- typical absorber density of 2×10^{14} cm^{-3} and low MgZnO carrier density (solid circles),
- same absorber carrier density with large MgZnO carrier density (open circles),
- higher absorber carrier density of 2×10^{16} cm^{-3} with large MgZnO carrier density (open square), and
- large carrier density in absorber with low carrier density in MgZnO (solid square).

The solid square representing the large carrier density in absorber coupled with low carrier density in emitter always produced low efficiencies for all of the six combinations for τ_b and S_{IF}. All six figures in Fig. 4.25 show that for large absorber doping, the region satisfying $n_{MZO} > p_{absorber}$ yields high efficiency but the efficiency is reduced considerably when this condition is not met.

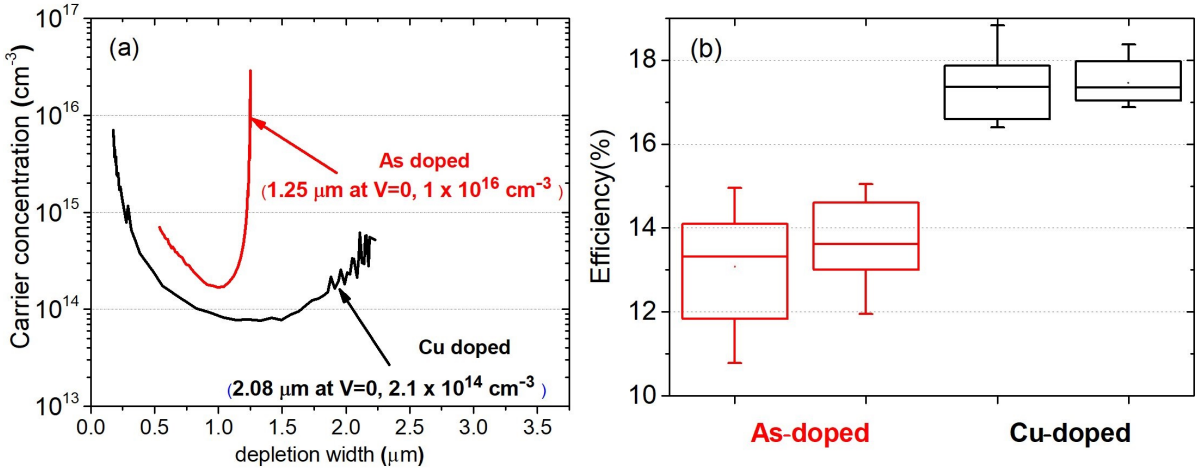

Figure 4.26: (a) Carrier concentration comparison for typical Cu-doped and As-doped absorbers derived from C-V measurement done at 100 kHz (b)Box plot comparison of efficiency of As-doped and Cu-doped absorbers with undoped MgZnO [26].

An experiment was conducted where a typical undoped MgZnO was used as an emitter with Cu-doped and As-doped absorbers. The typical carrier concentration for undoped MgZnO is the order of 10^{14} cm^{-3}. The typical Cu doped devices show absorber carrier density of $\approx 10^{14}$ cm^{-3} and the As doped absorbers have $\approx 10^{16}$ cm^{-3} as seen by carrier density vs depletion width plot in Fig. 4.26(a). The comparison of device efficiency of Cu-doped and As-doped absorbers is presented in Fig. 4.26(b). Based on the carrier concentrations of emitter and absorbers, the Cu-doped absorbers are more representative of the solid circles and the As-doped absorbers are representative of the solid squares. The decrease in efficiency of the As-doped devices in comparison to the Cu doped ones is likely due to the condition of $n_{MZO} > p_{absorber}$ not being satisfied.

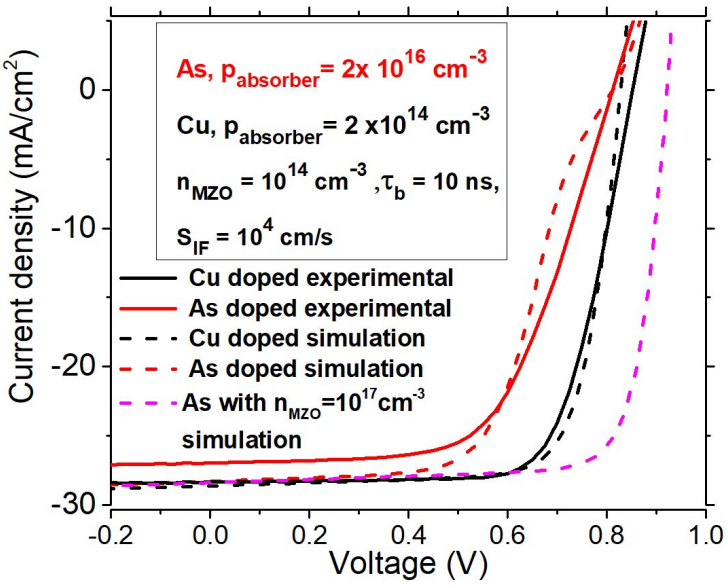

Figure 4.27: A comparison of As-doped and Cu-doped absorbers between the experiment (solid lines) and simulations (dotted lines). The inset presents the simulation parameters [26].

A close agreement is observed in the side-by-side comparison of the simulated and experimental J-V plots in Fig. 4.27. The As-doped absorbers suffered from a low V_{OC} in comparison to the Cu doped absorbers. To improve the V_{OC} and overall efficiency in the high carrier concentration absorbers with As doping, the emitter carrier concentration should be larger than that of the absorber as shown by the simulation with $n_{MZO} = 10^{17}$ cm^{-3}. Increased carrier concentration in the emitter will result in a larger built-in potential, and a

larger built-in potential results in a larger V_{OC}. Other advantage of such favourable band bending is the passivation of the emitter/absorber interface discussed in earlier sections.

4.5.2 Advantage of doping the emitter for highly doped absorbers

The advantage of Ga-doping in a typical Cu-doped low carrier concentration absorbers is seen with improvement in efficiency and the effective mitigation of the J-V distortions. Here we explain the mechanism of improvement of device performance shown by numerical simulations, primarily in the V_{OC}, that satisfy $n_{MZO} > p_{absorber}$ for highly doped absorbers.

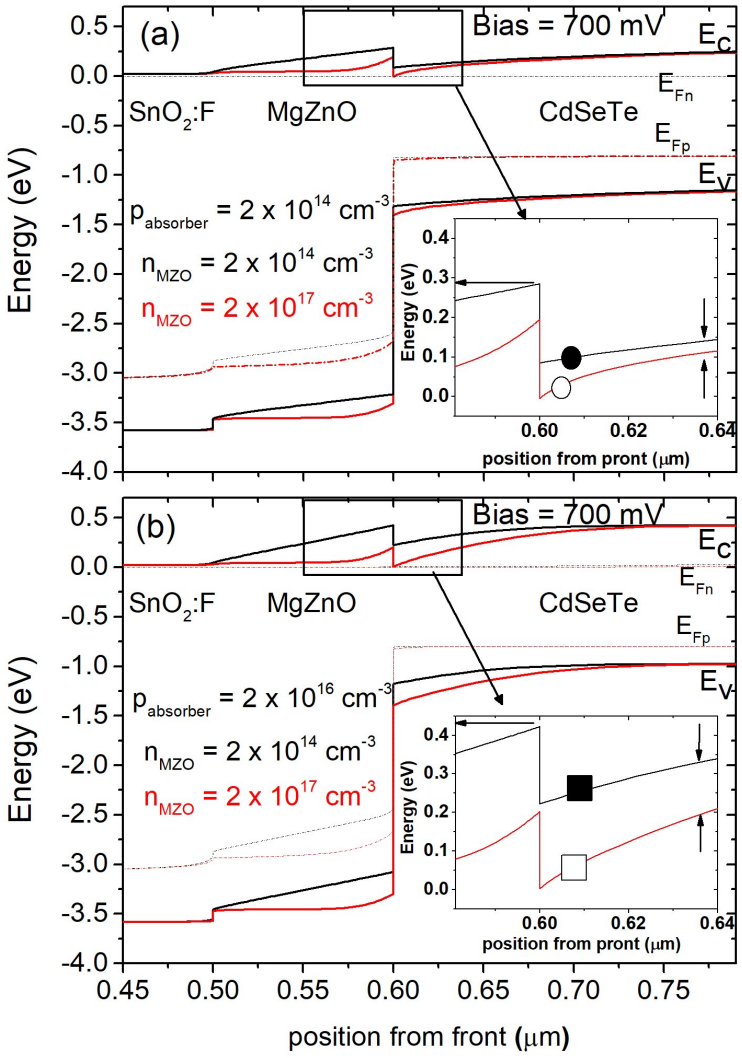

Figure 4.28: Energy band diagram at 700 mV for four points in Fig. 4.25(c) [26].

The energy band diagram at a forward voltage bias of 700 mV close to the maximum power point for the four key points from Fig. 4.25 is presented in Fig. 4.28. There is no significant difference between the energy band diagram for large and small emitter carrier concentration for a low abrober carrier density. However, for the higher carrier concentration in absorber of 2×10^{16} cm^{-3}, a higher carrier concentration in MgZnO of 2×10^{17} cm^{-3} has significant downward band bending at the interface in comparison to the low MgZnO carrier density of 2×10^{14} cm^{-3}.

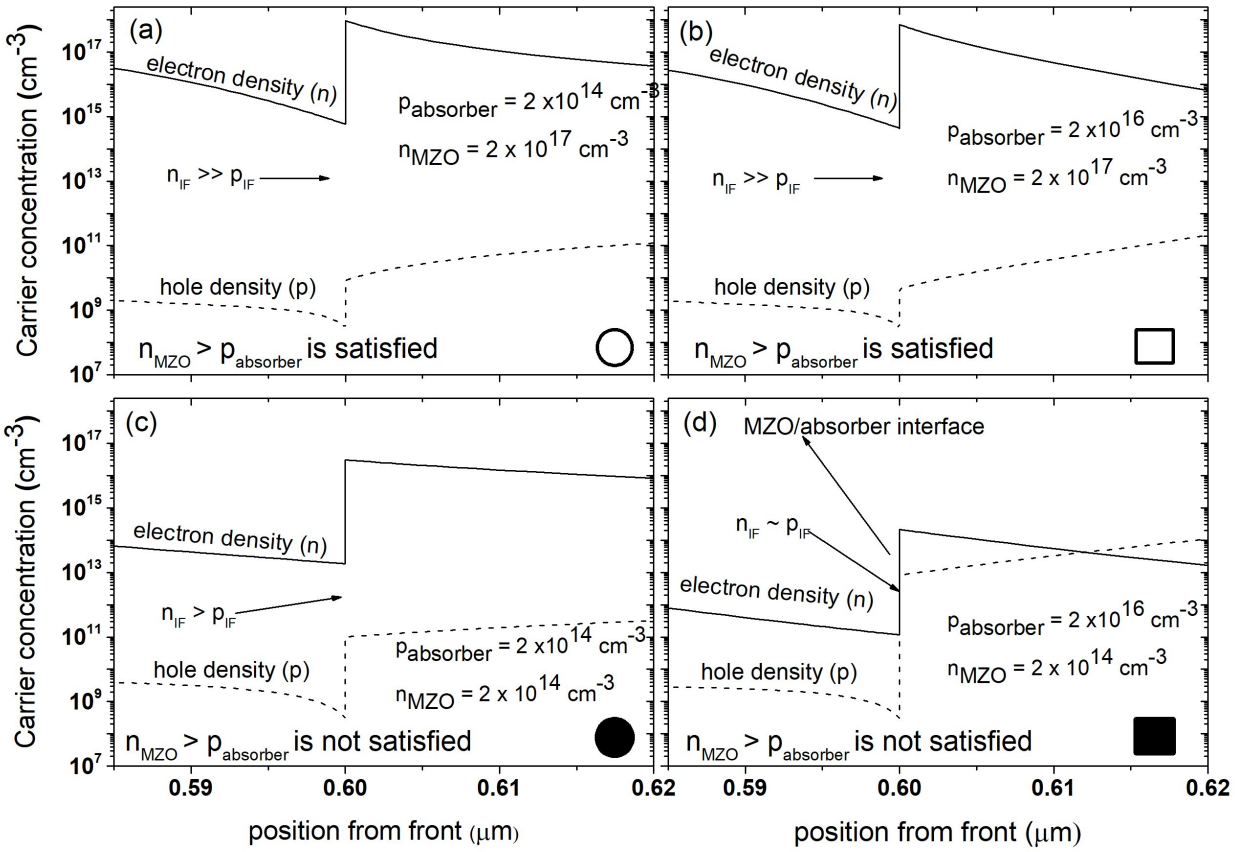

Figure 4.29: Electron and hole densities at the MgZnO/CdSeTe interface for the four cases from Fig. 4.25(c) at 700 mV [26]. Band diagrams are illustrated in Fig. 4.28.

A favorable band bending on the absorber side at the MgZnO/CdSeTe interface acts as a barrier for the holes and assists the movement of the electrons towards the front. This creates a large difference of a few orders of magnitude between the electron and hole densities at the interface as seen in Fig. 4.29(b). Such a disparity will reduce the recombination of the photogenerated electron-hole pairs at the interface and improve the extraction of electrons

at front contact. Further, the higher carrier density of emitter with higher absorber carrier density (open square) shows that the emitter/absorber barrier height is significantly smaller, and the band bending in the absorber side extends much deeper. The majority of the externally applied electric potential will drop in the absorber due to lowered emitter/absorber barrier height, resulting in efficient collection of photo-generated carriers due to larger band bending in the absorber, both contributing to an improved V_{OC} as shown by the simulated J-V curve for $n_{MZO} = 10^{17}$ cm^{-3} in Fig. 4.27.

4.5.3 Mitigation of large S_{IF}

The interface recombination discussed in section 2.3 can be employed to quantify the recombination at the interface (R_{IF}). The expression for bulk recombination given by equation 2.12 and the interface recombination velocity given by equation 2.16 can be used to deduce the total rate of recombination per unit area at the interface given by

$$R_{IF} = \frac{p_{IF}.n_{IF}}{p_{IF} + n_{IF}}.S_{IF} \tag{4.5}$$

where n_{IF} and p_{IF} are electron and hole densities at the emitter/absorber, and S_{IF} is the interface recombination velocity at this interface. This expression for interface recombination is a direct function of the carrier density at the interface. It was discussed above how a favorable band bending creates a large difference in electron and hole densities at the interface. This difference is orders of magnitude. Assuming $n_{MZO} > p_{absorber}$ for the highly doped absorber, from Fig. 4.29(b), $n_{IF} \gg p_{IF}$. Applying this condition to equation 4.5, the total interface recombination per unit area reduces to

$$R_{IF} \approx p_{IF}.S_{IF} \tag{4.6}$$

This means that when the $n_{MZO} > p_{absorber}$ is satisfied, the interface recombination rate depends on the smaller of the electron or hole densities at that interface. The interface recombination velocity also depends on various properties of the materials used, lattice mismatch, fixed charges, charge accumulations, and dangling bonds. An effective way to significantly reduce the detrimental effect of high S_{IF} at the emitter/absorber is by increasing the carrier concentration of MgZnO emitter so that $n_{MZO} > p_{absorber}$.

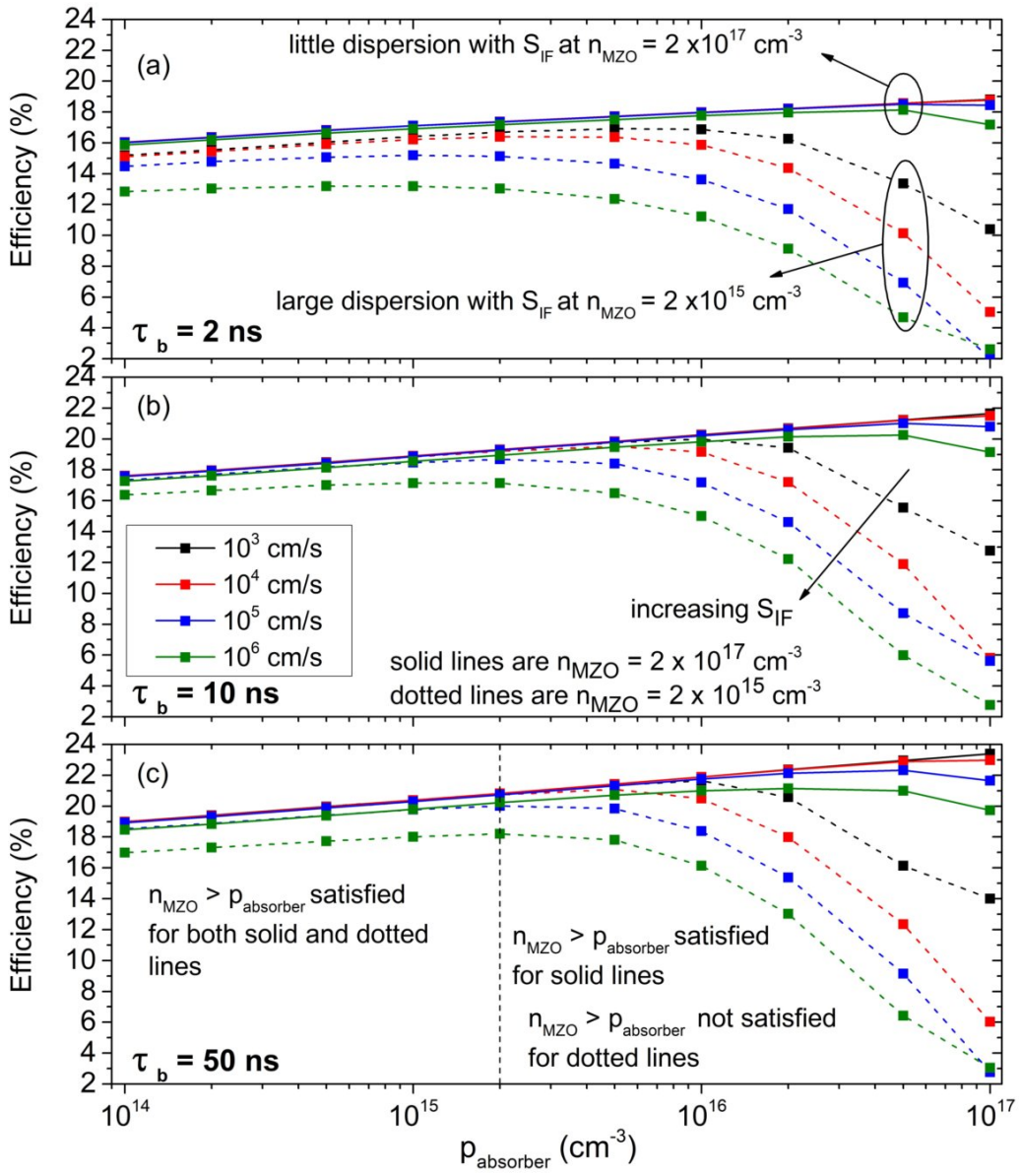

Figure 4.30: The deviations in device efficiency with varied S_{IF}, bulk carrier lifetimes with increasing carrier density in absorber [26].

A comprehensive picture of the effect on efficiency for varied interface recombination velocity with varied bulk carrier lifetimes is presented in Fig. 4.30 Low carrier density of 2 $\times$ 10^{15} cm^{-3} and high carrier density of 2 $\times$ 10^{17} cm^{-3} in MgZnO was chosen to compare the effect. The devices with higher doping in MgZnO are seen to have little dispersion in the efficiency with varied S_{IF}, whereas the devices with low carrier density in MgZnO suffered with low efficiency and large variations, especially when the condition of $n_{MZO} > p_{absorber}$ was not met at high absorber carrier density condition. The trend is consistent with every bulk carrier lifetime and confirms, $n_{MZO} > p_{absorber}$ to be a key factor in performance of highly doped absorbers.

4.6 Summary

Replacing the traditional CdS emitter with wide optical band-gap metal oxides improves the current collection in the CdTe-based TFSCs. The ternary alloy of $Mg_xZn_{1-x}O$ is of particular importance because the elemental ratio of the Mg:(Mg + Zn) in the ternary alloy can be varied. The optical band-gap widens with incorporation of larger Mg fraction in the MgZnO, and the majority of this optical band-gap widening occurs due to the E_C moving closer to the vacuum level. An optimal Mg fraction of 0.15 was found to be effective in the MgZnO emitter to produce high-efficiency CdTe-based solar cells. A moderate spike-like conduction band offset near 0.2 eV exists for this optimal Mg fraction. This band offset is not large enough to impede the thermionic emission of the photo-generated electrons in the absorber, and it was found to effectively passivate the emitter/absorber interface shown by the PL, TRPL and low temperature J-V measurements.

Current-voltage distortions of various magnitudes were observed in the CdTe-based solar cells that employ the wide band-gap MgZnO emitter layer, and were particularly large when there were insufficient short-wavelength photons to increase the electron density above that of the absorber hole density. The distortions were observed to be dependent in the Mg fraction in the MgZnO. Increasing Mg fraction increases the secondary barrier at the emitter/absorber interface above the optimal $\Delta E_C = 0.2$ eV. An enlarged secondary barrier results in the failure

of superposition of the light and dark curves. The light soaking experiments coupled with the numerical device simulations demonstrated that the wide band-gap MgZnO emitters are populated by acceptor-type compensating defects. These defects have different properties in dark and under illumination condition. In dark, these acceptor-type defects are filled with electrons which compensates the n-type carrier concentration in the emitter. Under the illumination, these acceptor type defects release electrons by absorbing the high energy blue photons. The released electrons increase the n-type conductivity in the MgZnO emitter, but not necessarily by a sufficient amount. The Ga-doping of the MgZnO demonstrates the promise of extrinsic doping of MgZnO. Such extrinsic doping eliminate the J-V distortions typical of the undoped MgZnO emitter and remove the need for the undoped MgZnO to rely on photogeneration of the electrons to improve its conductivity.

Further, the numerical simulations confirm that the doping in the emitter should be higher than the doping in the absorber to achieve better efficiency. The condition is particularly crucial in absorbers with high hole carrier concentration. In these highly doped absorbers, if the emitter carrier density is higher than the absorber carrier density, there is an effective band-bending that extends much deeper into the absorber side while the barrier height at the emitter/absorber is realtively low, a condition that will help achieve high V_{OC}. Another advantage of doping emitter in highly doped absorbers is a large difference in the electron and hole densities at the emitter absorber interface that occurs due to a favourable band bending and is key to minimize the negative impacts of large S_{IF} at the emitter/absorber interface.

Chapter 5

ALTERNATIVE BACK CONTACT APPROACHES FOR POLYCRYSTALLINE CdTe THIN-FILM SOLAR CELLS

The double-diode model discussed in chapter 3 pointed out that the the choice of the metal contact at the back will have significant bearing on efficient hole extraction. An ideal metal contact would have a work function close to the VBM position of the CdTe absorber. This chapter focuses on various back contact structures as shown in Fig. 5.1 and listed in table 5.1.

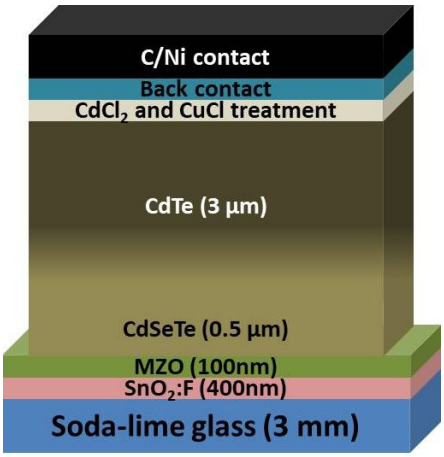

Figure 5.1: Schematic of the device structure for various back contact study.

Table 5.1: Description of various back contacts for CdTe absorber

Back contact	Description	Purpose
CdTe - Ag/Co/Pt/Te/Se	Metal back contact	Metal-Semiconductor contact
CdTe/Te - Ag/Co/Pt/Se	Te as a back buffer	Effect of back buffer layer
CdTe/TeO_x/Te	Oxide as back buffer	Copper-free back contact
CdTe/Se/ITO	Transparent back contact	Tandem and bifacial cells
CdTe/MgO-NiO/Te	Metal oxide contact	MIS back contact

Key for this chapter are the different possibilities for the back contact. The effect of introducing a thin Te buffer layer between the CdTe and various metals has been previously

shown to improve the contact [21]. The newer work reported here includes TeO_x as metal-oxide buffer, a Se/ITO transparent back contact with promise for a tandem and bifacial structure, and two metal oxides, MgO and NiO, that were explored as metal-oxide back contacts. The traditional C/Ni paint was applied when applicable to protect the devices from the probe damage during the various measurements.

5.1 Background

A common feature of most back contacts for CdTe to date is the use of Cu. Diffusing Cu at the back of the CdTe solar cells helps attain a good lateral conduction and effectively reduces the back contact barrier [39, 40, 41, 106, 107]. The Cu diffusion is achieved by various methods such as performing a CuCl treatment or deposition of metallic Cu followed by annealing, depositing Cu_xTe. The Cu diffusion helps improve the hole density and makes a quasi-ohmic back contact, but it also leads to device stability issues and degradation in the CdTe-based solar cells due to the diffusion of the interstitial Cu towards the front [39, 108, 109, 110]. The recent development of As-doping of the absorbers has led to the replacement of the Cu doping in the absorber and back contact formation in the commercial CdTe modules that has improved the stability, reliability and degradation of the modules [111, 112].

The back contact in a typical superstrate configuration for CdTe-based TFSCs should be a good hole-selective layer. A large work function for CdTe means that the valence band maxima position is farther away from the vacuum energy level and a barrier will be formed at the back that impedes the hole collection [30]. Such a barrier at back can lead to the current limitation effect and rollover in the first quadrant [34]. The use of a buffer layer at the back has been employed to facilitate the hole extraction, while the use of wide band-gap semiconductor like ZnTe doped with Cu [113, 114, 115], and the use of ternary alloys such as CdZnTe, and CdMgTe have been applied to use as an electron reflector strategies to reflect the electrons in the conduction bands towards the front CdTe region and assist holes collection [116, 117]. Chemical etchants to selectively remove the Cd from the CdTe to make

a Te-rich back surface have also been implemented [118, 119]. At CSU, a thin Te buffer between the CdTe absorber and the C/Ni electrode has been an effective way to improve the back contact [21, 22]. The purpose of the buffer layers at the back is to reduce the back contact barriers, reduce the interface recombination, and attain suitable band bending to promote an efficient hole extraction [120, 121].

5.2 CdTe-metal back contact with varied metal work function

An experiment with five different elements with increasing work functions was used as a direct back contact in a typical device structure. Out of the five elements used, Ag (4.2 eV), Co (5.0 eV) and Pt (5.6 eV) are metals whereas Se (5.7 eV) and Te (5.2 eV) are metalloids [12, 122]. A schematic of the device structure for the various contacts is shown in the Fig. 5.2. The thickness of the metals i.e. Ag, Co and Pt was 100-nm which were sputter deposited. The thickness of metalloid i.e. Te, and Se was 30-nm which were evaporated. Current-voltage, quantum efficiency, and capacitance-voltage measurements were done on these devices.

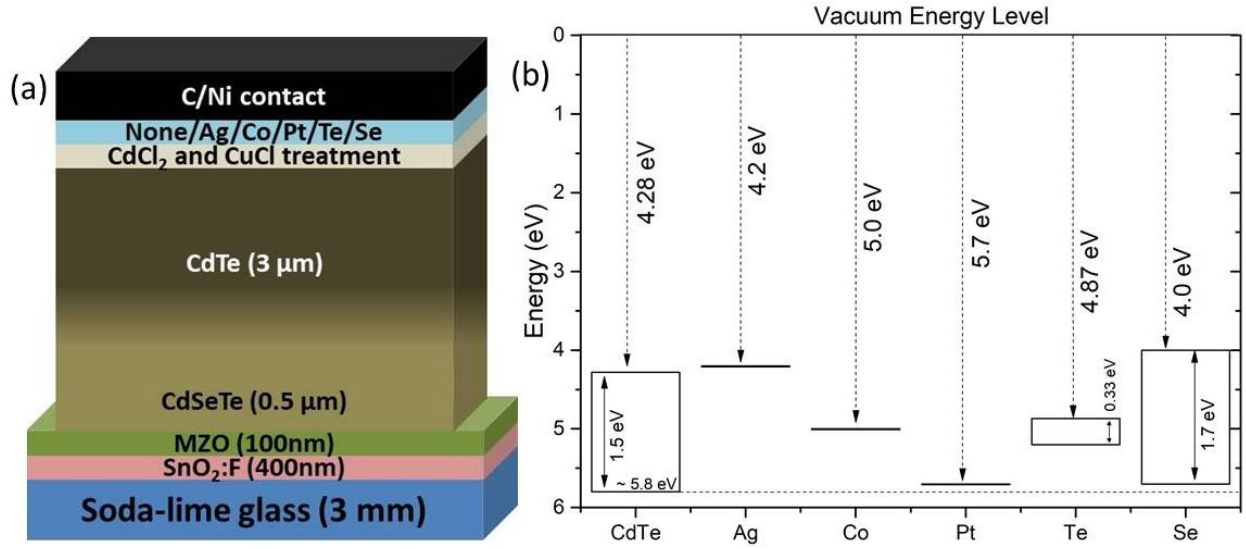

Figure 5.2: (a) Schematic of the device structure. (b) Relative position of VBM and work functions of various back contacts with respect to CdTe.

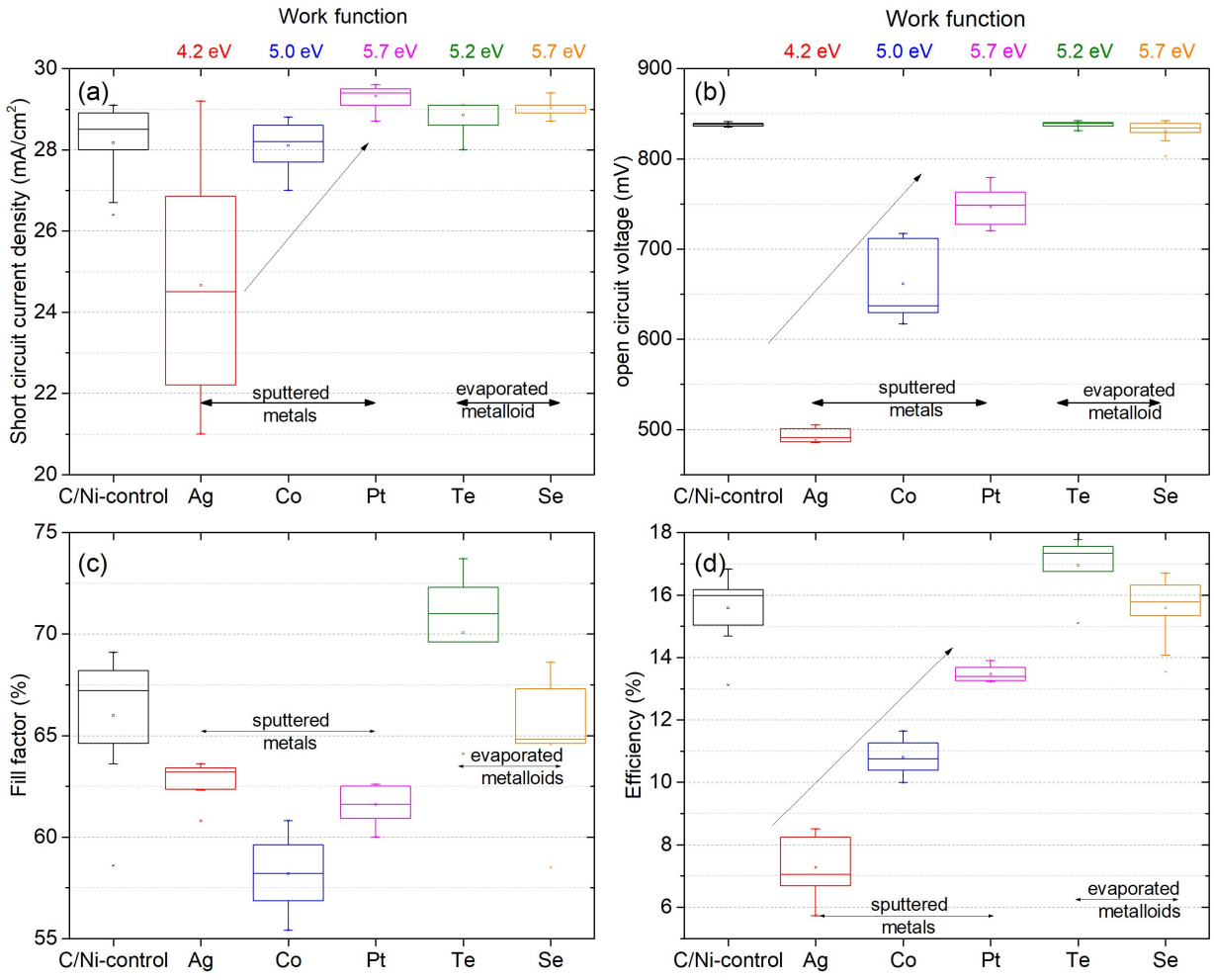

Figure 5.3: Box plot of J-V parameters for the 10 small area devices with various elements as a back electrode in direct contact with CdTe.

Box plots of the J-V parameters for the ten small area devices with various back contact elements are shown in Fig. 5.3. A clear trend in the J_{SC}, and V_{OC} is seen in the metal contacts with increasing work function that dictates the over all conversion efficiency. The metalloids Te, and Se have a better V_{OC} and have better power conversion efficiency than the C/Ni-control sample, and any of the sputtered metal contacts. The J-V, QE, and C-V for the best devices from each plate is plotted in the Fig. 5.4, and the critical parameters are tabulated in table 5.2. A possible explanation for the difference in device performance between the metals and metalloids could be the method of deposition. Sputtering produces better film quality and uniformity but can potentially cause sputter damage to the CdTe

surface due to larger kinetic energy of the sputtered species when they arrive to adhere to the CdTe surface during sputter deposition. A relatively low power density of less than 2 W/cm^2 on metal targets was used to mitigate such issues, so the difference in performance between the metal and metalloid as contacts could be more fundamental.

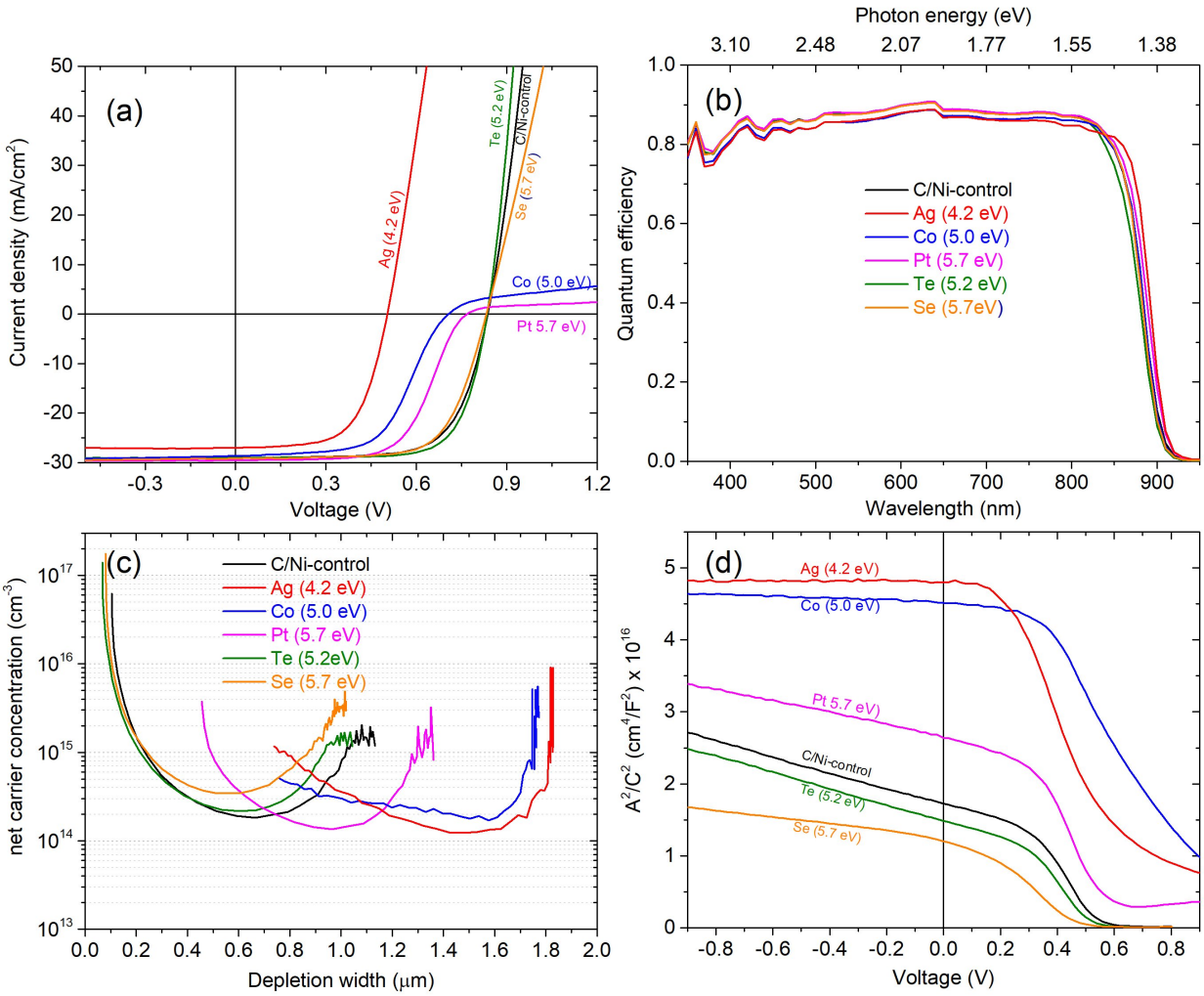

Figure 5.4: (a) J-V plots, (b) QE plots, (c) Carrier density vs. depletion width plots, and (d) Mott Schottky plot for the best devices from Fig. 5.3.

The J-V plot for best devices for each back contact show that the metal contacts sputtered directly on CdTe suffer from low V_{OC} and exhibit a roll-over behavior in the first quadrant even in devices with large work function metal contact like Co and Pt. The QE response of all devices is comparable throughout the visible spectrum. The depletion width is decreasing with increasing work function but still larger in comparison to the C/Ni-control, Te, and Se

Table 5.2: J-V parameters, depletion width (W_D) at 0 V and net carrier concentration (N_A) at bottom of belly from C-V measurement from Fig. 5.4(c)

Back contact	J_{SC} (mA/cm^2)	V_{OC} (mV)	FF (%)	$Eff.$ (%)	W_D (μm)	N_A (cm^{-3})
C/Ni-control	29.1	838	69.1	16.8	1.09	1.8×10^{14}
Ag	27.0	505	62.3	8.5	1.82	1.2×10^{14}
Co	28.7	707	57.4	11.6	1.76	1.7×10^{14}
Pt	29.6	767	61.3	13.9	1.35	1.3×10^{14}
Te	29.1	836	72.7	17.7	1.01	2.1×10^{14}
Se	29.2	833	68.6	16.7	0.91	3.4×10^{14}

contacts. A roll-over behavior in the first quadrant in J-V plot is signature of a typical barrier at back and issues with selectivity of hole extraction at back [30, 33].

This rollover suggests that the origin of the back barrier may not be solely dependent on the difference between the work function of metal and valence band maxima position of the CdTe. The back electrodes studied in this first experiment were all deposited on bare CdTe. The bare CdTe surface is marred with significant amount of defects as discussed in section 2.3, Fig. 2.1, due to the dangling bonds, lattice interruption, charge accumulation etc. An atomistic level approach by density functional theory (DFT) numerical simulations has shown that these defects on the free CdTe surface are dependent on the atomic termination and crystal orientation [123]. Interestingly, the metalloids like Se, and Te have well-behaved J-V curves with efficiency better or comparable to the C/Ni-control. Unlike the metals, these two metalloids are elemental semiconductors with well defined conduction band and valence bands with optical band-gap of 0.33 eV and 1.7 eV for Te and Se respectively. This puts their VBM closer to that of CdTe VBM that could potentially act as an intermediate buffer layer to make a hole contact as shown in Fig. 5.2(b).

5.3 Te as a buffer layer between CdTe and metal electrode

In last section, the use of elemental semiconductors such as Te, and Se produced better results than the metal contacts at the back surface of the CdTe film. One logical explanation is the use of Te, and Se layers at the back act as a buffer layer that helps to mitigate the negative effects of the intrinsic defects present on the free CdTe surface. The use of

appropriate buffer layer at back reduces the effective barrier for the holes, and improves the hole extraction at the back [22, 120]. To test the effects of such buffer layers, a second experiment was designed where 30-nm of Te was introduced between the various metal contacts and the CdTe surface in the device structure as shown in Fig. 5.5.

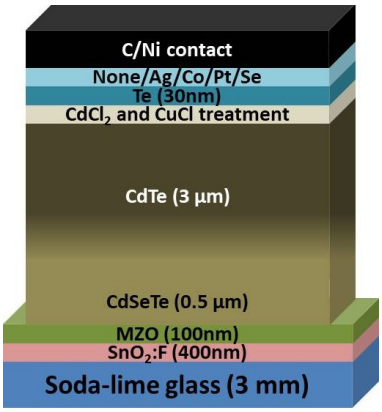

Figure 5.5: Schematic of the device structure with 30 nm of Te as back buffer.

The choice of Te was based on the results presented in Fig. 5.3 where the conversion efficiency was highest for Te incorporated devices. All the sputtered metal contacts were 100-nm thick and the Se was 30-nm thick with identical deposition methods and conditions. The box plots of the J-V parameters of fifteen small area devices from this set of experiments are presented in Fig. 5.6. The plot clearly demonstrates that the use of Te as a buffer layer improves the over all performance of the devices. The Te/Ag combination produced low J-V parameters, which is probably due to the very low work function of Ag. The other higher work-function elements, Co, Pt and Se, showed a significant improvement in the J-V parameters and overall efficiency. A comparison of the results form the two experiments where metal was directly deposited on bare CdTe surface and another where a buffer layer of Te was used between the CdTe and metal electrode clearly establishes the usage of the buffer layer to be beneficial for the improvement of the back contact.

The J-V, QE, and capacitance-voltage measurements for the best devices with the Te layer are shown in Fig. 5.7. The Te/Ag suffers from a low V_{OC} and has a relatively larger depletion width. The capacitance-voltage measurement from Fig 5.4(c) and 5.7(c) clearly shows that the well-performing devices have narrow depletion widths. Inclusion of a Te

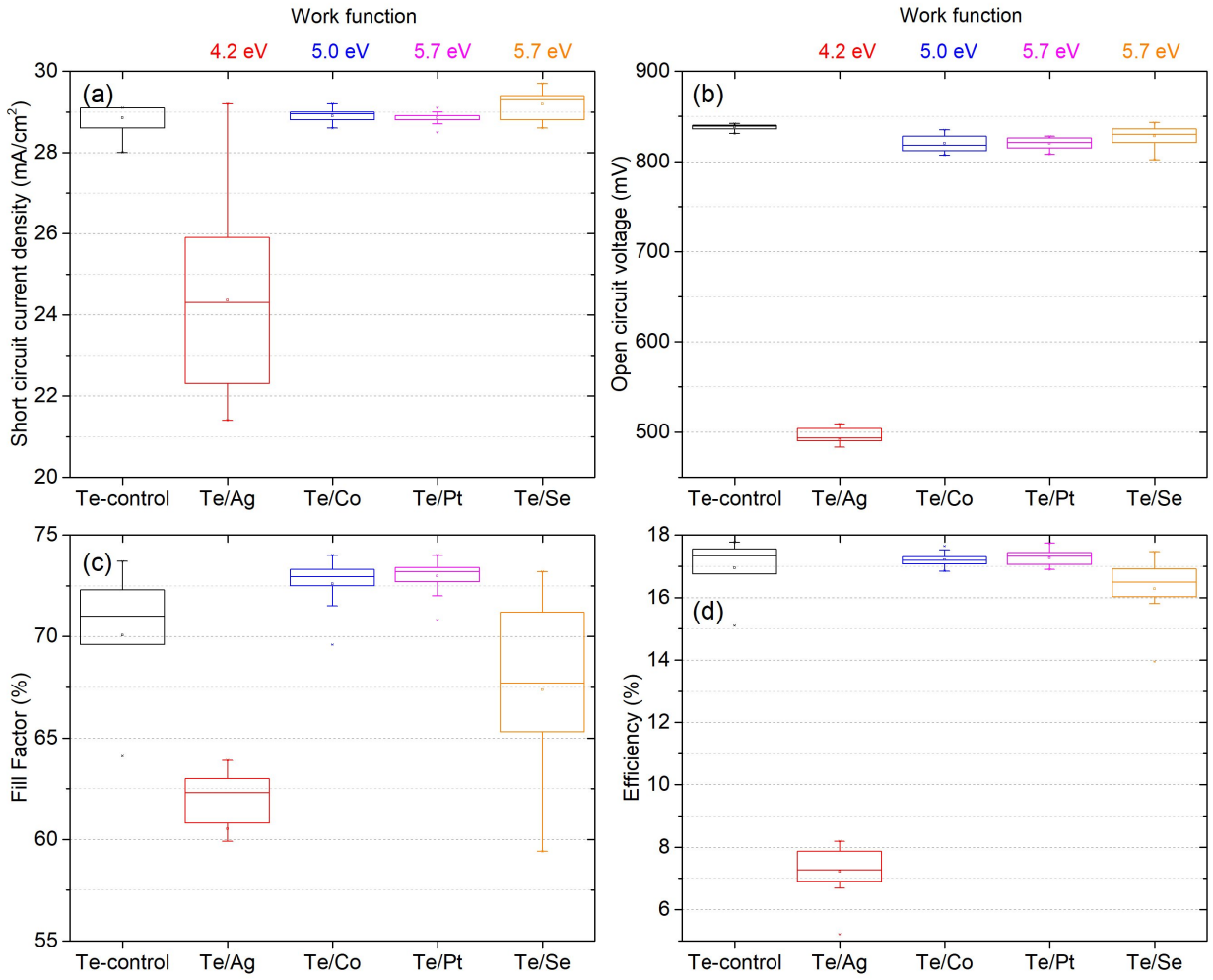

Figure 5.6: Box plot of J-V parameters with Te back buffer and various back electrode.

Table 5.3: J-V parameters, depletion width (W_D) at 0 V and net carrier concentration (N_A) at bottom of belly from C-V measurement from Fig. 5.7(c)

Back contact	J_{SC} (mA/cm^2)	V_{OC} (mV)	FF (%)	$Eff.$ (%)	W_D (μm)	N_A (cm^{-3})
Te-control	28.9	835	73.7	17.8	1.01	2.2×10^{14}
Te/Ag	25.9	508	62.8	8.2	1.70	5.7×10^{13}
Te/Co	29.2	824	73.3	17.6	0.98	2.6×10^{14}
Te/Pt	29.1	826	73.7	17.7	0.91	2.9×10^{14}
Te/Se	29.0	823	73.2	17.5	0.91	3.6×10^{14}

buffer layer at the back of CdTe surface helped the Co, and Pt devices achieve a smaller depletion width and larger V_{OC}. The large gain in V_{OC} for these cells is attributed to reduced recombination at the interface. As the devices under study were fabricated under identical conditions except for the application of a Te buffer layer, the improvement in V_{OC} of the

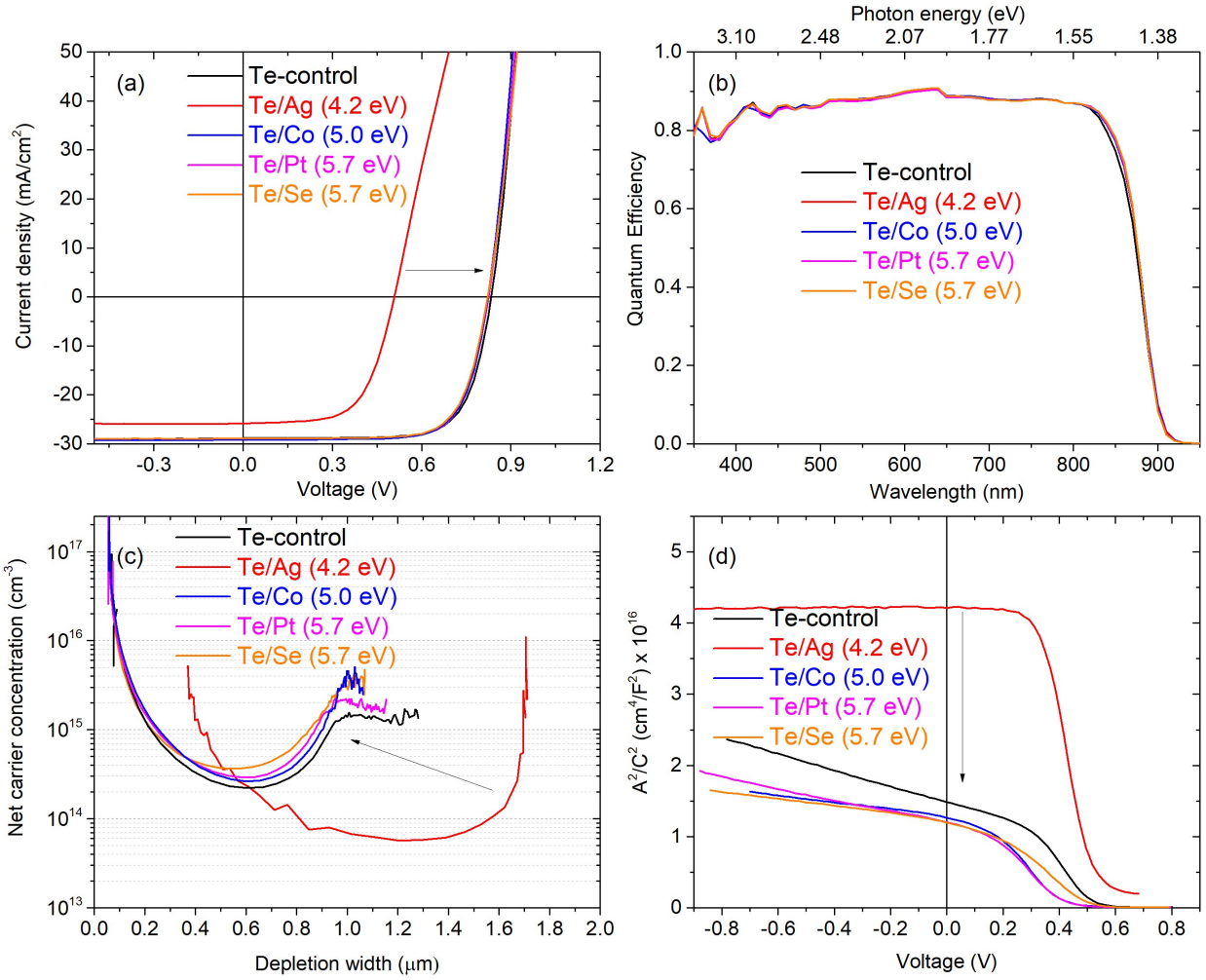

Figure 5.7: (a) J-V plots, (b) QE plots, (c) Carrier density vs. depletion width plots, and (d) Mott Schottky plot for the best devices from Fig. 5.6.

devices with Te buffer layer is due to the effective mitigation of the interface recombination present in the CdTe/Co, and CdTe/Pt contacts due to the presence of the Te buffer layer.

5.4 TeO_x as a back buffer and surface passivation oxide

Improved device performance by using a buffer between the CdTe back surface and the electrode is found to be key in the improvement of the V_{OC} and the over all device performance in the previous section. The choice of the buffer is dictated by various parameters like, an appropriate work function, good lateral conductivity, high p-type doping, ability to passivate the defects in the bare CdTe surface etc. A good back buffer reduces the back

contact barrier, reduces the interface recombination, and help attain a suitable band bending to effectively extract the photogenerated holes [120, 121]. The results with Te buffer layer clearly show that it satisfies these conditions [21, 22]. Various oxides like Al_2O_3, SiO_2, MoO_x, and other transition metal oxides has been extensively used to passivate the defective semiconductor surfaces for silicon solar technology [42, 43, 45, 44, 124]. The purpose of using such oxides is to passivate the surface/interface defects in the silicon semiconductors to lower surface recombination by both chemical and field effect passivation. Chemical passivation refers to the reduction of dangling bonds by saturating them, and field-effect passivation refers to an alteration of concentration of electrons and holes at an interface to reduce the recombination, a mechanism extensively discussed with the MgZnO front contact in chapter 4.

An added benefit of using an oxide as a back buffer for surface passivation is the possibility of bifacial in the solar cells, as most oxides have wide bandgaps [125]. Most metal oxides, however are insulating, with large dielectric constant which aids to the formation of a metal-insulator-semiconductor. The results with the Te back buffer have opened possibility of other back buffer layers. This section is focused on implementing the TeO_x as a back buffer, a choice based on the results from devices with Te buffer. The method of deposition of the TeO_x is RF-sputtering from a single TeO_x target at a 5-mTorr pressure with Ar process gas with relatively low power density of 0.75 W/cm^2 applied to the target. A detailed study in the variation of process parameters, thickness of the oxide, the compatibility with existing device architecture and device characterization is presented in the remainder of this section.

5.4.1 TeO_x thickness, and sequence of $CdCl_2$ treatment

To explore the possibility of using a TeO_x as a back buffer for CdTe-based solar cells, experiments with variations in the TeO_x thickness, and the sequence of the vital $CdCl_2$ treatment were conducted. Fig. 5.8(a) represents the schematic diagram of the semiconductor stack. A Cu doping prior to the $CdCl_2$ treatment is not an ideal device processing sequence, since it drives the Cu towards the front junction and lowers the device performance due to

the high processing temperatures during $CdCl_2$ treatment. With this in mind, the devices with TeO_x were fabricated without any Cu doping. Owing to the insulating nature of oxides, only two thicknesses of 5 nm, and 10 nm of TeO_x were chosen, and variation in the sequence of the $CdCl_2$ treatment: before the TeO_x, after the TeO_2, and a double $CdCl_2$ treatment both before and after the deposition of the TeO_x were carried out.

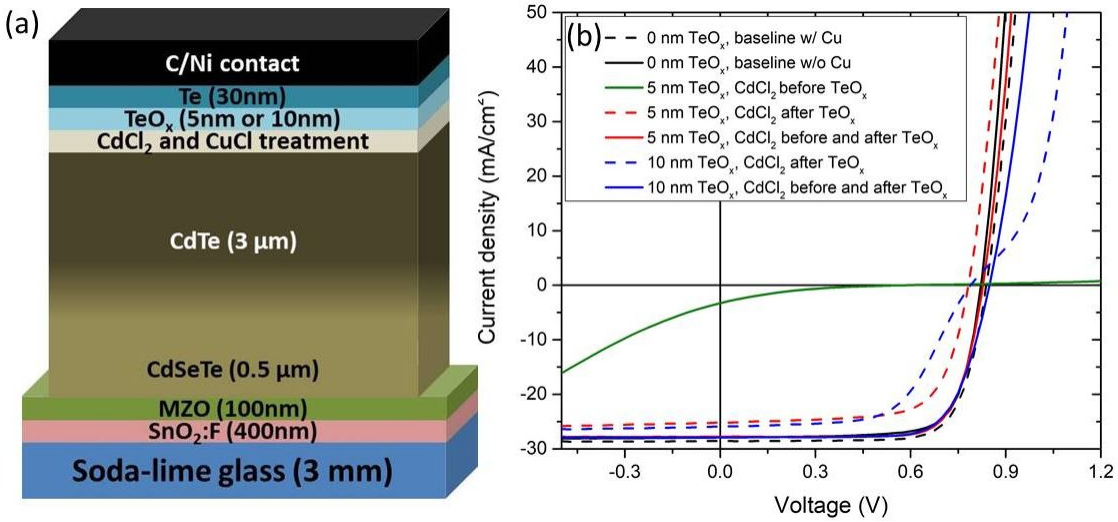

Figure 5.8: (a)Schematic of the device structure with TeO_x as back buffer (b) J-V plots for typical devices with various thickness of TeO_x and $CdCl_2$

Table 5.4: J-V parameters for varied TeO_x thickness and $CdCl_2$ sequence from Fig. 5.8

TeO_x thickness	# of $CdCl_2$	$CdCl_2$ sequence	Cu doping	J_{SC} (mA/cm^2)	V_{OC} (mV)	FF (%)	Eff. (%)
0 nm (baseline)	1	after CdTe	Yes	28.6	839	75.0	18.0
0 nm (baseline)	1	after CdTe	No	27.9	822	75.0	17.2
5 nm	1	before TeO_x	No	3.3	587	12.6	0.2
5 nm	1	after TeO_x	No	25.2	783	70	13.8
5 nm	2	before and after TeO_x	No	27.8	829	75.8	17.5
10 nm	1	after TeO_x	No	25.9	789	60.2	12.3
10 nm	2	before and after TeO_x	No	27.9	849	72.8	17.2

The J-V plots for the best devices from each substrate is presented in Fig. 5.8(b), the J-V parameters are listed in table 5.4, and the box plots of the J-V parameters for 25 small area solar cells from each substrate are presented in Fig. 5.9. The devices with a 5-nm TeO_x without a second $CdCl_2$ treatment after the TeO_x exhibit extremely poor photovoltaic performance. This suggests that 5-nm TeO_x as deposited is insulating and hinders the

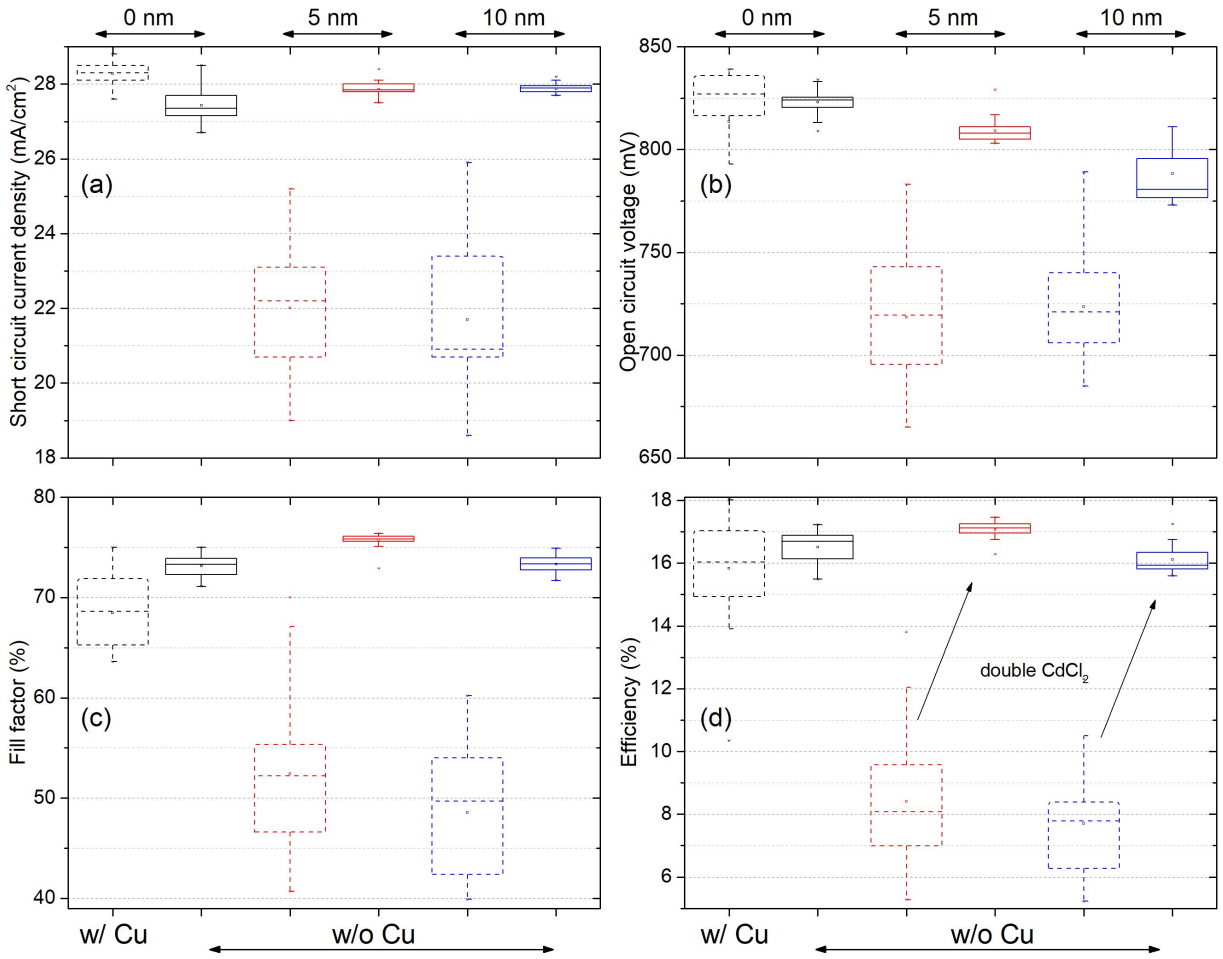

Figure 5.9: Box plot of J-V parameters of 25 small area cells with varied TeO_x thickness (0 nm, 5 nm, 10 nm) and $CdCl_2$ sequence. Dashed boxes are for a single $CdCl_2$ step.

extraction of charges. However, 5-nm TeO_x devices exhibited the best performance when a double $CdCl_2$ treatment, one before and the other after the deposition of TeO_x, was carried out. This suggests that the second $CdCl_2$ treatment is critical to extract charges. The key point from this set of experiments is the ability to fabricate devices with efficiencies in excess of 17 % with an absorber that is not intentionally doped. The Cu doping of the absorber has been considered vital to improve the hole density and form a quasi-ohmic back contact for the CdTe solar cells, but the results here show that application of TeO_x eliminates the need for intentional Cu doping of the absorber.

Devices with TeO_x thickness of 5-nm and 10-nm with double $CdCl_2$, as well as baseline devices with no TeO_x, and with and without copper were chosen for further analysis. Spectral

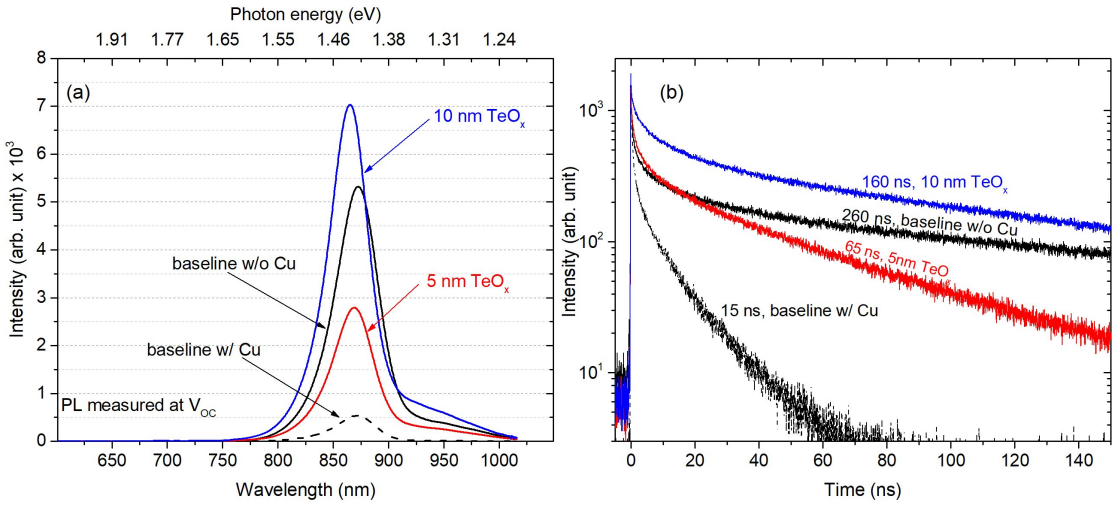

Figure 5.10: (a) PL spectra intensity and (b) TRPL decay of select devices from Fig. 5.8

PL and time resolved PL was conducted for a comparison of the relative peak intensities and decay rates of these four samples. The copper doped absorber with no TeO_x has the smallest spectral PL intensity and the fastest TRPL decay. Others that had no copper had stronger PL intensities and slower TRPL decay rates. The results demonstrate the passivating effect of TeO_x on the CdTe-based TFSCs. An earlier study shows correlation of the Te^{4+} at the MgZnO/CdSeTe interface and the carrier recombination lifetimes demonstrated a similar passivating effect of TeO_x [59] at the front MgZnO/CdSeTe interface. The relative energy band position of CdTe with TeO_x is given in Fig. 5.11(a) [126, 127].

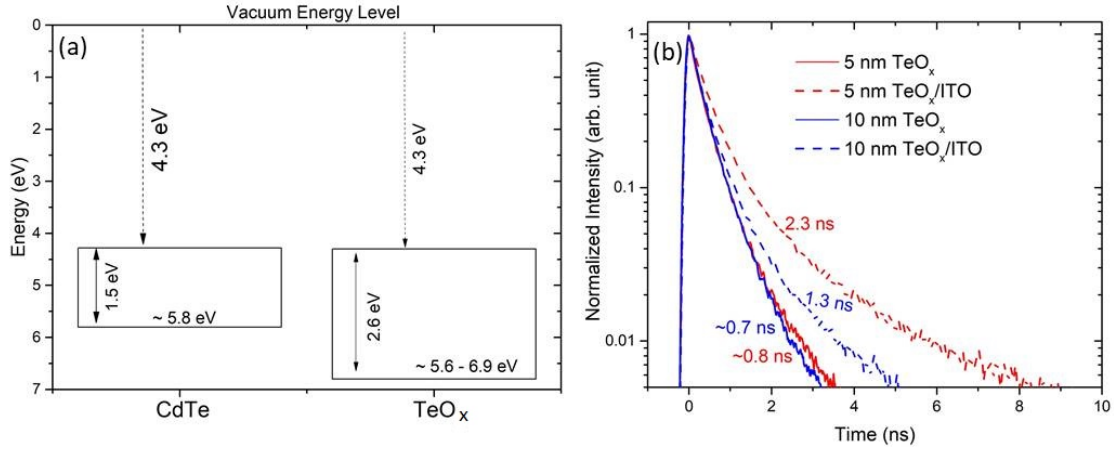

Figure 5.11: (a) Relative position of energy bands for CdTe and TeO_x (b) TRPL decay from back illumination for TeO_x with a transparent back contact.

To further study the passivating nature of TeO_x, devices with configuration shown in Fig. 5.8(a) with double $CdCl_2$ and thin 30-nm transparent ITO replacing the opaque Te/C/Ni back contact were fabricated. The thin transparent ITO should allow optical probing of the CdTe/TeO_x interface, which is not possible with the standard opaque contact. TRPL measurements were then conducted with the laser illuminating through the ITO contact, and the result presented in Fig. 5.11(b) shows lifetimes of a few ns measured with the TeO_x/ITO back contact. In contrast, the TRPL signal with the laser illuminated on a bare CdTe surface is below the detection limit. While, further study is needed to identify the actual mechanism of the passivation, the results presented here clearly demonstrate the passivating nature of TeO_x to a CdTe surface. The J-V results and TRPL results present TeO_x as a promising candidate for the passivation of the CdTe surface which can be integrated in the existing device architecture for typical CdTe superstrate configuration with no major changes. An added benefit of using TeO_x is the fabrication of devices with an undoped absorber that have device performance comparable to the doped absorber which is critical for the stability, and longevity of the solar cells.

5.4.2 Effect of Oxygen during the TeO_x deposition

The use of oxygen during the various steps of the semiconductor deposition and treatment process plays a significant role in the device performance of the CdTe-based solar cells. To study the effect of presence of oxygen during the deposition of the TeO_x, a repeat of the experiment discussed in the previous section was conducted, except the TeO_x was deposited with $Ar/O_2 = 95/5$ instead of pure Ar. Here also, four substrates, a baseline with Cu, a baseline without Cu, and two substrates with 5 nm and 10 nm TeO_x with a double $CdCl_2$ treatment without Cu were fabricated with the device stack similar to Fig. 5.8(a).

The devices with TeO_x deposited in the mixed gas had a similar performance to the ones where the TeO_x is deposited in Ar only. The box plots for J-V parameters in Fig. 5.12 show the TeO_x devices perform better than the Cu doped devices and validates the reproducible results with TeO_x. The J-V plots for the best devices, spectral PL and a comparative C-V

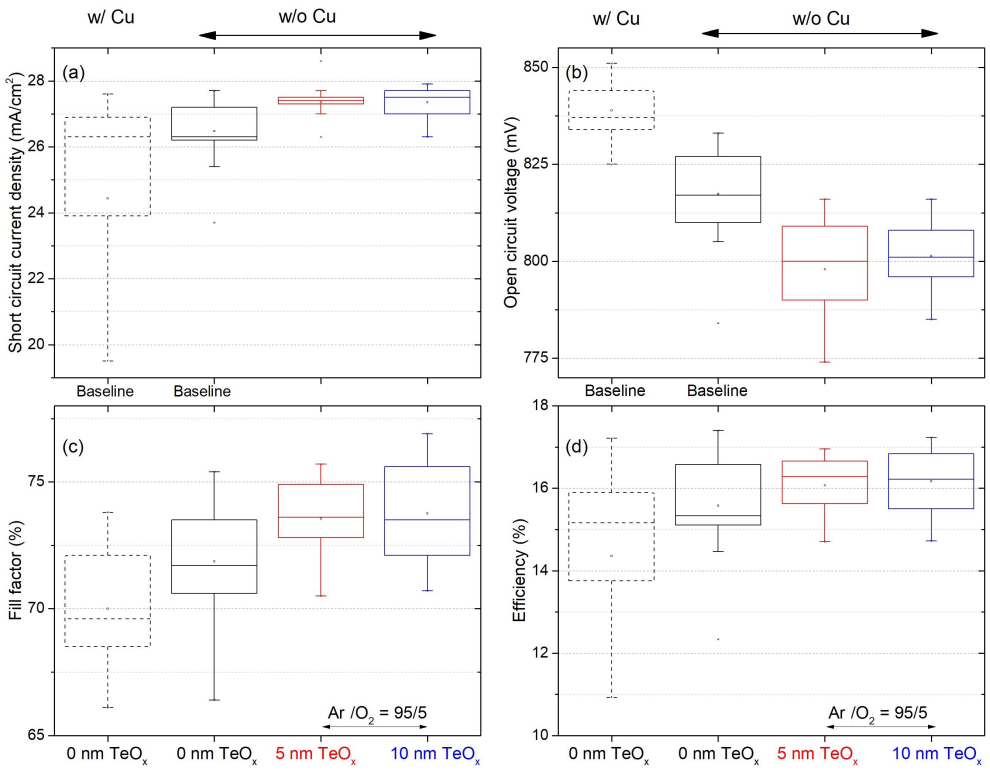

Figure 5.12: Box plot of the J-V parameters of 25 small area devices from each substrates with TeO_x deposited in a Ar/O_2 ambiance.

plot are shown in Fig. 5.13. The J-V parameters in table 5.5 are similar to the J-V parameters form table 5.4 for TeO_x with similar thickness irrespective of the ambiance during the TeO_x deposition. The relative spectral PL intensity presented in Fig. 5.13(b) has a trend similar to the one observed in Fig. 5.10(a) with highest PL for 10 nm TeO_x and lowest for Cu doped absorber.

Table 5.5: J-V parameters for best devices from Fig. 5.12.

TeO_x thickness	Cu doping	J_{SC} (mA/cm^2)	V_{OC} (mV)	FF (%)	$Eff.$ (%)
0 nm (baseline)	Yes	27.6	851	73.4	17.2
0 nm (baseline)	No	27.7	833	75.4	17.4
5 nm	No	27.7	816	74.9	17.0
5 nm	No	27.7	815	76.4	17.2

The major difference between the devices with TeO_x deposited in different ambiance is evident in the capacitance measurement as shown in Fig. 5.13(c)-(d) and the parameters tabulated in table 5.6. Among the TeO_x devices, deposited in $Ar/O_2 = 95/5$ ambiance,

the measured depletion width is relatively wider than in the devices where the TeO_x was deposited in pure Ar. This is analogous to the undoped devices where the depletion width is large and the Cu doping reduces the depletion width. One possibility is the variation in the stoichiometry of the as deposited TeO_x between the Ar-only and Ar/O_2 ambiance. The TeO_x deposited in Ar only ambiance is Te rich and pushes the depletion width to be narrower as we saw in Fig. 5.7(c). Unlike what was observed in Fig. 5.4 with different metal back contacts, where the increase in depletion width was accompanied by poor device performance, the effect of the TeO_x deposition ambiance and the increase in depletion width had minimal effect on the device performance. This indifference further suggests that TeO_x is a good choice for a transparent back buffer layer.

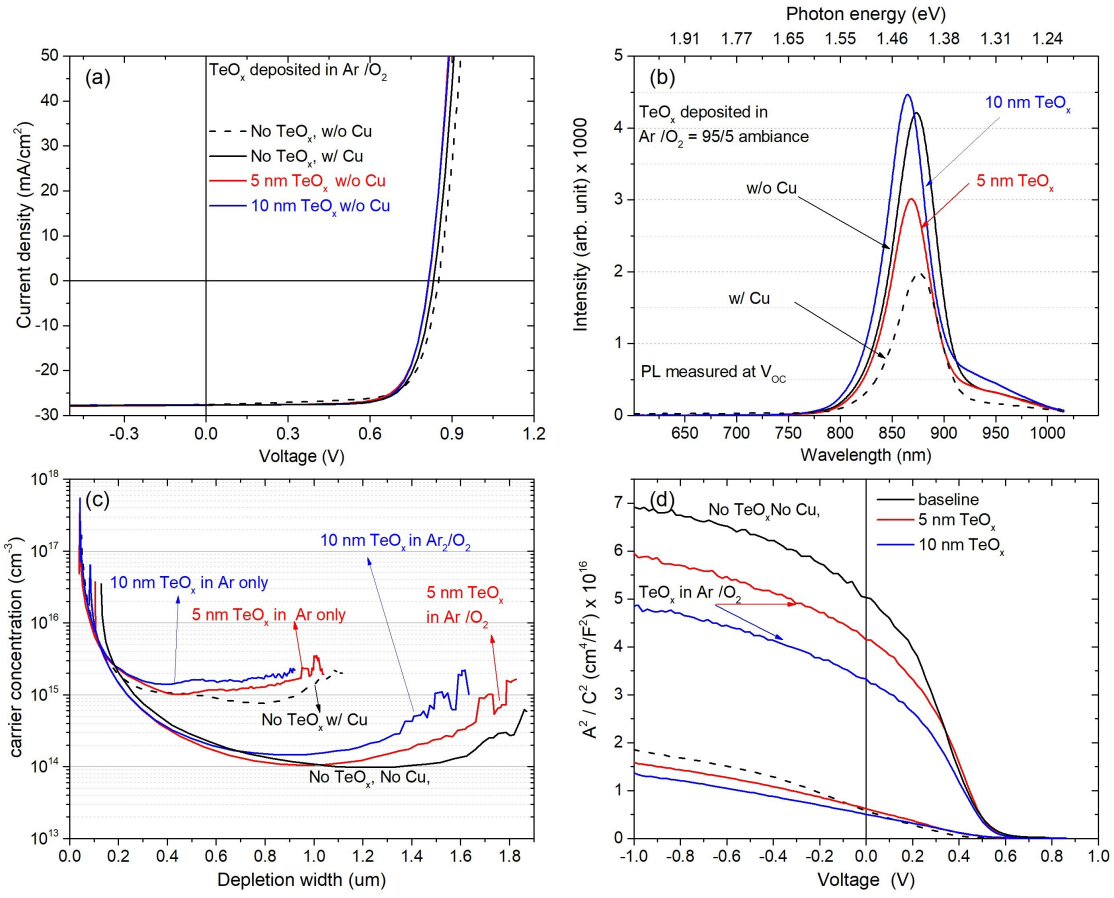

Figure 5.13: (a) J-V plots and (b) spectral PL intensity for best devices, (c)-(d) capacitance measurements of best devices with TeO_x deposited in Ar only and in $Ar/O_2 = 95/5$ ambiance.

Table 5.6: C-V parameters for TeO_x deposited in different ambiance from 5.13(c)-(d).

TeO_x thickness (nm)	TeO_x ambiance	Cu doping	Depletion width at 0 V (μm)	Carrier density at bottom of belly (cm^{-3})
0 nm (baseline)	-	Yes	0.63	7.5×10^{14}
0 nm (baseline)	-	No	1.86	9.7×10^{13}
5 nm	Ar only	No	0.65	1.0×10^{15}
5 nm	$Ar/O_2 = 95/5$	No	1.7	1.0×10^{14}
10 nm	Ar only	No	0.59	1.4×10^{15}
10 nm	$Ar/O_2 = 95/5$	No	1.52	1.4×10^{14}

5.5 Se/ITO transparent back contact

The use of Se as back contact discussed in section 5.2 produced devices with respectable conversion efficiency among the set of back contact studied. An added benefit of Se at back is it's wide optical bandgap of 1.7 eV, making it suitable for transparent back contact. The traditional C/Ni paint was replaced by indium tin oxide (ITO), a transparent conductive oxide, to make a fully functional solar device. A transparent back contact opens possibility for a bifacial solar cell or a tandem device structure such a two junction monolithic structure or a mechanically stacked four contact structure.

Solar cells with transparent back contacts of 30-nm of Se and 100-nm of ITO were prepared with device stack as shown in Fig. 5.14(a). The J-V plot with the J-V parameters of a typical device is presented in Fig. 5.15(b). A respectable device efficiency of 14.1 % was achieved in comparison 16.7 % with the standard C/Ni back contact. The transmission measurements in Fig. 5.14(c) show a relative ratio of transmission of sub bandgap photons for a Se/ITO device to the bare CdTe only film is relatively high. Such a high transmission validates the transparent back contact. These Se/ITO devices when measured from a back illumination for both J-V and QE measurement had a poor response. The comparison of a QE for front and back illumination is presented in Fig. 5.14(d). The QE response for the back illumination has a characteristics of a deep buried junction. Effective ways to mitigate such buried junction to activate the bifaciality are thinning of the absorber, improving the lateral conductivity of the Se back contact, improve crystalline nature of the Se, use metal finger grids for contact on ITO, device processing and thermal anneals etc. The presented

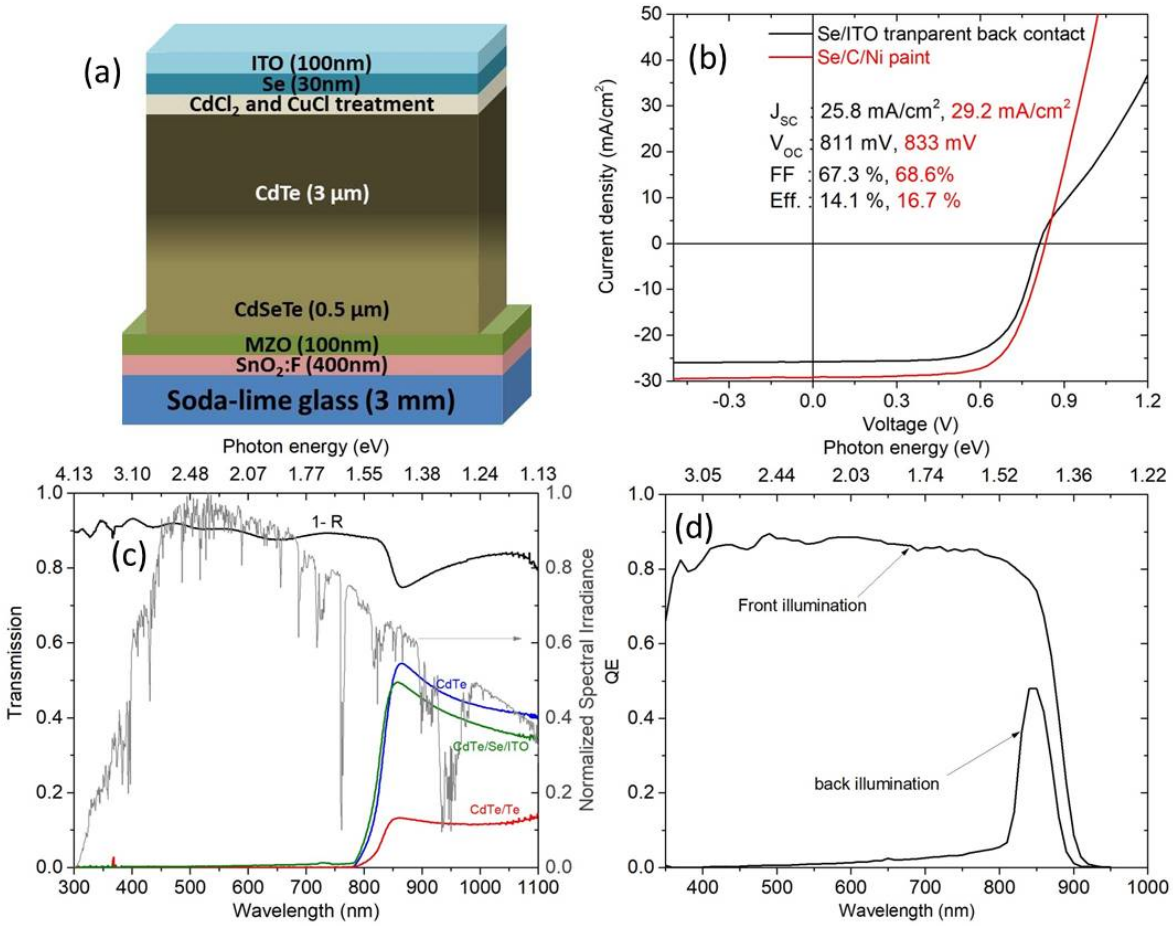

Figure 5.14: (a) Schematic of Se/ITO transparent back contact (b) Comparative J-V plot of Se/ITO and Se/C/Ni back contact (c) Transmission measurement for various structures (d) QE plot of Se/ITO transparent back contact with front and back illumination

Se/ITO work is preliminary and exploratory in nature, but holds significant promise in term of bifaical and tandem device architectures.

5.6 Metal-oxide buffer layers

Double heterostructures with a CdTe-based absorber sandwiched between the sputter deposited metal oxides like Al_2O_3, MgZnO, SiO_2, and TiO_2 have produced lifetimes the order of hundred of ns [128]. The $Mg_xZn_{1-x}O$ emitter work in chapter 4 has demonstrated that the alloying of ZnO with MgO has passivating effects and a statistically monotonic increase in V_{OC} with increasing Mg fraction. With this in mind, MgO and NiO were chosen

as metal oxides for the back contact. A schematic of the device structure is as shown in Fig. 5.15(a) with a combination of MgO and NiO. An electrode of traditional Te/C/Ni or transparent ITO of 30-nm was applied to measure the J-V measurements and optical/opto-electronic measurements from both front and back illumination. A comparative J-V plot for various combination of MgO and NiO in comparison to the control sample is presented in Fig. 5.15(b) and J-V parameters in table 5.7. While the devices with metal oxide as

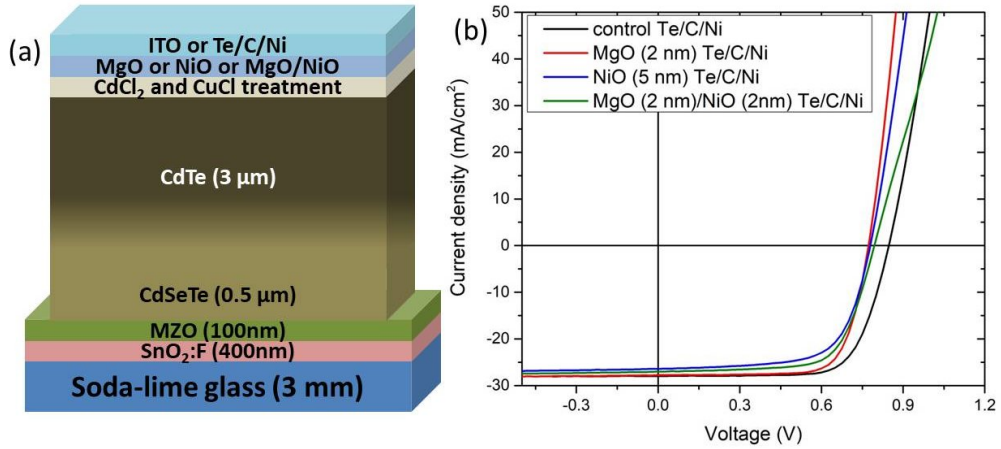

Figure 5.15: (a) Schematic of the device structure (b) J-V plots for best devices.

Table 5.7: J-V parameters for best devices from Fig. 5.15(b).

back contact	J_{SC} (mA/cm^2)	V_{OC} (mV)	FF (%)	$Eff.$ (%)
control Te/C/Ni	27.9	848	72.0	17.0
MgO (2 nm) Te/C/Ni	27.7	773	74.6	16.0
NiO (5 nm) Te/C/Ni	26.4	780	67.1	13.8
MgO (2 nm)/NiO (2 nm) Te/C/Ni	27.0	794	69.1	14.8

a back contact with traditional Te/C/Ni back electrode produced devices with conversion efficiency less than that of the control samples, a transparent back contact of ITO allowed to probe the back of CdTe with the PL, TRPL, and QE measured for both front and back illumination as shown in Fig. 5.16. The PL measured from front for a typical CdTe device and a 2-nm MgO back buffer layer is comparable, the PL signal for a back illumination for the MgO back buffer was significant and corresponds to the optical bandgap of CdTe. Further, a comparative TRPL measurement was conducted on devices with MgO deposited from a single cermaic target and a metallic Mg target with reactive sputtering in an Ar_2/O_2

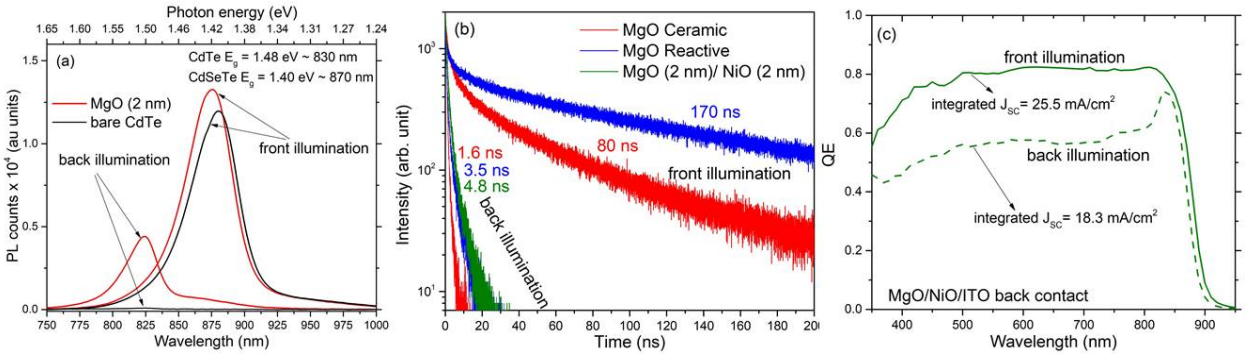

Figure 5.16: (a) PL measurement, (b) TRPL measurement, and (c) QE measurements with illumination from front and back of the cell for combinations of MgO and NiO back buffers.

ambiance. Lifetimes the order of few ns have been measured for rear illumination, which shows that MgO has the potential to passivate defects present in the bare CdTe irrespective of the method of deposition. A bilayer of 2 nm MgO and 2 nm of NiO produced a lifetime close to 5 ns from back illumination. Quatum efficiency measured in the device with such bilayer of MgO/NiO showed excellent opto-electronic response for illumination from both sides even though the J-V response from the back illumination was poor. A high resolution TEM imaging of the bilayer back contact region in Fig. 5.17 demonstrates the metal oxides are conformal and unform.

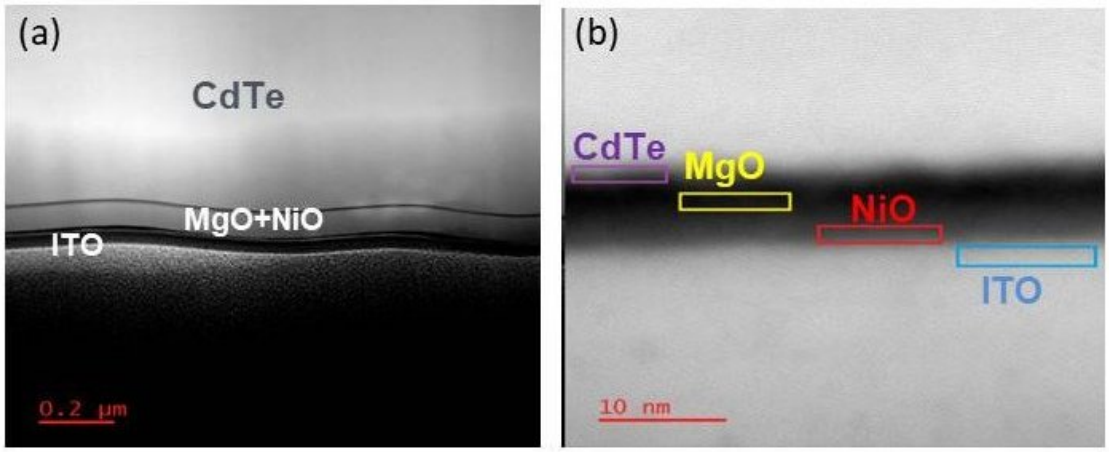

Figure 5.17: (a) High resolution TEM image of MgO/NiO bilayer metal oxide back contact for CdTe. (b) Zoomed region at the hole transport interface (* measured at University of Illinois Chicago)

5.7 Summary

The efficient extraction of the holes form the back of a CdTe-based solar cell in a superstrate configuration is critical. The device architecture and the polycrystalline nature of the CdTe makes the bare CdTe surface prone to the recombination. To inhibit the recombination on the CdTe surface and make a hole selective contact, the use of a buffer layer would be beneficial. Such a buffer layer should be highly doped p^+ in nature with relatively large work function to bend the bands upwards.

The use of a thin Te as a buffer between the high work function metal contacts and the bare CdTe surface has shown the importance of a back buffer layer for the CdTe-based TFSCs. An extension of the Te to a thin TeO_x back buffer has demonstrated the device efficiency in excess of 17 % without doping the absorber. A dopant free absorber has an improved stability, and realiabilty which is immune to the degradation induced due to the external dopants. Wide bandgap TeO_x has exhibited passivating properties to the CdTe surface measured with the PL and TRPL measurements. The results have paved path for the exploration of other metal oxides like MgO, NiO, MoO_x and other transition metal oxides to make a passivated hole selective back contact for the polycrystalline CdTe TFSCs. The integration of such oxides in the existing device architecture is fairly straight forward which provides the flexibility in terms of device architecture modifications in future for structures like bifacial, PERC, tandem etc.

Further the buffer layer should have passivating properties to inhibit the negative effects of the large interface recombination prevalent on a CdTe surface. Metal oxides can passivate a surface either with a chemical passivation by saturating the dangling bonds or by field effect passivation due to the inherent fixed charges in them. Also, the use of a wideband-gap back buffer layer opens the possibility of a transparent back contact which can boost the conversion efficiency by enhanced current collection due to absorption of diffused light from the back. In addition, a transparent back contact opens the possibility for a tandem solar cells. A proper band-gap engineering and current matching between the top and a bottom

solar cell with a transparent contact between them would help absorb most of the solar spectrum and an added voltage.

Chapter 6

CONCLUSIONS AND DISCUSSION

From being just a niche new-generation absorber few decades ago, the CdTe-based thin-film technology has established itself as a leading photovoltaic technology. The research and technological advancements coupled with the low cost and large scale manufacturing has given it the status of the second most common commercial photovoltaic technology, only behind the crystalline silicon. Hence, the technology is a forerunner to make a significant difference in the renewable energy supply and the global clean energy market.

Understanding the fundamental device physics, material selection and characterization techniques are key to the further advancement of the CdTe-based TFSCs. The primary findings of the work has been discussed in detail in chapter 4 and 5. Both chapters have a summary at the end that gives a brief of the key findings and the advantages of employing the metal oxides as front and back buffer for the CdTe-based solar cell. While the technology has made tremendous advancements, there is considerable room for improvement. The key to further the technology lies in the modification of the current device architecture enabled by the passivating transparent metal oxides. This sets a good premise to elaborate the findings from the work to a much broader aspects of the CdTe technology.

Alloying, optical bandgap and energy band offset engineering

The majority of improvement in the CdTe solar cells has come by employing optical band-gap engineering to improve the photon collection that elevated the current collection. This optical band-gap engineering has been achieved by alloying the semiconductors whether that be in the emitter of $Mg_xZn_{1-x}O$ or the absorber of $CdSe_xTe_{1-x}$. The results of this work has demonstrated that the optical band-gap can be modulated by varying the elemental fraction of the constituents which can have a significant bearing on the energy band offset at the interface. An optimal ΔE_C of 0.2 eV with Mg fraction of 0.15 in the MgZnO for the

CdSeTe absorber was found to be ideal. These results were derived from the electron contact at the emitter/absorber interface in the E_C, but the findings are equally applicable to other interfaces within the CdTe-based TFSCs.

Origin of J-V distortions, doping of emitter and energy band-bending

A small spike in the conduction energy band that can be easily overcome by the electron charge carrier with thermionic emission between the absorber and emitter was found to be beneficial that showed improved passivation based on the low temperature J-V and photoluminescence measurements. A larger than optimal ΔE_C of 0.2 eV leads to the distortions in the current voltage characteristics. An appropriate alloying of the materials with correct choice of dopants can improve the conductivity and bend the bands for efficient collection of charges as was achieved by Ga-doping of the MgZnO emitter. An extrinsic doping of wide bandgap emitter will remedy the need for photogeneration and improves the n-type behaviour, and electron concentration in the emitter. Larger electron concentration in the emitter leads to a favorable band bending that will mitigate the surface recombination by creating disparity in electron and hole densities at the interface. Such a phenomenon is particularly important at interfaces that have inherently large defects, charge accumulations, large lattice mismatch which are unavoidable either due to the limitations in material choice or the device processing parameters. In any case, an ideal emitter for CdTe-based solar cells should have electron carrier density comparable or larger than the hole concentration in the absorber.

Back contact barrier

The efficient extraction of holes at the back of superstrate CdTe has been a challenge primarily due to the barrier at the back. It impedes the charge collection and has been identified as significant cause for the large voltage deficit. Introduction of a 30 nm of Te as a back buffer layer between the CdTe and different metal back contacts with varying work function points that the origin of a back barrier in superstrate CdTe configuration is not

solely due to the large difference in metal work function and the ionization energy of the CdTe. A contribution to such barrier also comes from the intrinsic defects on a bare CdTe surface. This work has put forward various metal oxides like MgO, NiO, TeO_x that are fit to meet the demands of a passivating buffer layer, demonstrating their ability to passivate such defects, assistance in the extraction of holes, band alignment with the CdTe energy bands, can be easily integrated to the present day device architecture and compatible to the device processing.

Transparent back contact, tandems and bifacials

The Se/ITO, TeO_x, MgO and NiO work present in chapter 5 have shown promise with a transparent back contact. A transparent back contact of a top cell would allow the sub bandgap photons to pass through and get absorbed in the low band-gap bottom cell. A transparent back contact is valuable to a tandem formation for both a two point monolithic structure and a four point mechanically stacked structure. The oxides are fairly robust to the typical semiconductor fabrication process and are ideal candidates for transparent contacts. CdTe-based absorbers of different optical band-gaps can be used as top and bottom absorbers with a transparent contact between them. Tandem architectures will improve the absorption range of the AM 1.5G spectrum and yield an added voltage. Another benefit of transparent contact is the possibility for bifacial solar cells which will improve the current collection due to the absorption of the diffused and reflected lights entering the device from the transparent back contact.

Mitigation of defects

The defects in CdTe-based solar cells are either inherently present or introduced during the device fabrication process primarily during the Cu treatment. Such defects can lead to issues with stability. The TeO_x as a back contact has discounted the need for the traditional copper treatment of the absorber. The TeO_x incorporated devices without the Cu treatment

have demonstrated efficiency on par with the conventional Cu treated absorbers which is important to reduce the defect density in the absorber and improves the stability

Passivation of the CdTe surface

The polycrystalline nature of CdTe makes the grain boundaries a potential source of the recombination. A $CdCl_2$ treatment is needed to passivate the surfaces of the grain boundaries that leads to a dramatic improvement in the photovoltaic performance. Similarly, the surface of the CdTe is inherently defective and a proper strategy to make these defects benign is key to improve the conversion efficiency to further the technology. MgZnO has served as an excellent front electron contact that is robust to the post deposition processes and treatments demanded due to the device architecture. Embracing various depostition methods like plasma enhanced chemical vapor deposition, atomic layer deposition, molecular beam epitaxy, sputtering etc to deposit oxides on these bare CdTe surface to reduce the effects of defects. Such deposition methods are relatively slow and provide an excellent control of the deposition parameters, control for the alteration of stoichiometry of the oxides to serve the needs for a passivated surface.

Proposed total cell

A proposed passivated emitter and rear contact device architecture for a CdTe-based solar cell is presented in Fig. 6.1 using a front and a back passivating oxide that sandwich the CdTe-based absorber.

Adjacent to these oxides, an electron selective n^+ emitter and a hole selective p^+ buffer layer are proposed to facilitate the extraction of the photogenerated electron and hole pairs form the absorber. A highly doped n^+ emitter layer with a proper band alignment, preferably with a positive fixed charge would make an ideal electron contact. The MgZnO:Ga work presented in chapter 4 with a proper elemental ratio of Mg:(Mg + Zn) in the MgZnO alloy has shown significant promise. The recovery of open circuit voltage with use of a thin intrinsic MgZnO between the MgZnO:Ga and the absorber in Fig. 4.24 is in agreement with the

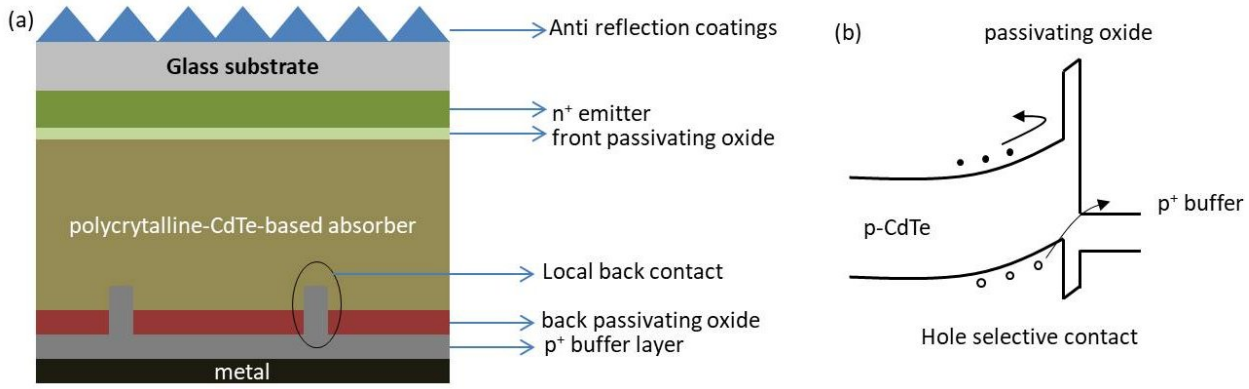

Figure 6.1: (a) A passivated emitter and rear contact structure for a polycrystalline CdTe. (b) A hole selective back contact with a passivating oxide and proper band bending.

proposed device architecture where a spatial separation at MgZnO:Ga/absorber interface would further reduce the recombination. Similarly, at the back, a passivating oxide layer with preferably negative fixed charge such as Al_2O_3 can be used [128]. A rear passivation with TeO_x, MgO and NiO have all shown promise to be a good rear passivation oxide for the CdTe-based solar cells [129, 130]. The work presented here show the TeO_x deposited with RF-sputtering has shown promising sign, and a thermally grown native TeO_x on a CdTe surface would be ideal for the surface passivation [59].

The choice of the p^+ buffer layer behind the passivating oxide is equally important to make a hole selective layer. Currently the use of Te has served the best but an appropriate band bending and hole selectivity by inducing a band bending by proper work function of the material is key. An alloy of $Se_{1-x}Te_x$ has shown that the optical band-gap and the relative energy band positions can be tuned [122]. A proper choice of 'x' in the $Se_{1-x}Te_x$ can help find the right band offset in the E_V for the extraction of holes similar to the $Mg_xZn_{1-x}O$ in the front electron contact discussed in chapter 4. To overcome the inhibition of hole extraction across the passivating oxides with high dielectric values, that makes them insulating to the p^+ buffer, small local point contacts between the absorber and the back p^+ buffer layer can be made by micro-patterning. An aspect ratio that measures the ratio of the width and thickness of these point contacts, and the weighted average of the local back contact area

and the back passivated area play significant role in the efficient extraction of holes from the absorber side across the insulating rear passivating oxide layer [131].

The present day superstrate device architecture of the CdTe-based thin-film solar cells has room to mature. A transition to a more matured form is inspired to attain high power conversion efficiency and in large part will be dictated by the technology's commercial, and economical success. The methods presented in this work provide a framework for the CdTe industry and research community to embrace the changes that are necessary to make such a transition in future.

Bibliography

[1] https://www.census.gov/popclock/world. (Acessed on May 01, 2021).

[2] https://www.un.org/development/desa/en/news/population/world-population-prospects-2017.html. (Acessed on May 01, 2021).

[3] https://ourworldindata.org/energy-production-consumption. (Acessed on May 01, 2021).

[4] Jean-Robert Petit, Jean Jouzel, Dominique Raynaud, Narcisse I Barkov, J-M Barnola, Isabelle Basile, Michael Bender, Jérôme Chappellaz, M Davis, Gilles Delaygue, et al. Climate and atmospheric history of the past 420,000 years from the vostok ice core, antarctica. *Nature*, 399(6735):429–436, 1999.

[5] Dieter Lüthi, Martine Le Floch, Bernhard Bereiter, Thomas Blunier, Jean-Marc Barnola, Urs Siegenthaler, Dominique Raynaud, Jean Jouzel, Hubertus Fischer, Kenji Kawamura, et al. High-resolution carbon dioxide concentration record 650,000–800,000 years before present. *Nature*, 453(7193):379–382, 2008.

[6] Chris D Thomas, Alison Cameron, Rhys E Green, Michel Bakkenes, Linda J Beaumont, Yvonne C Collingham, Barend FN Erasmus, Marinez Ferreira De Siqueira, Alan Grainger, Lee Hannah, et al. Extinction risk from climate change. *Nature*, 427(6970):145–148, 2004.

[7] https://climate.nasa.gov/evidence/. (Acessed on May 01, 2021).

[8] https://www.eia.gov/todayinenergy. U. S energy information administration (Acessed on May 01, 2021).

[9] MJ Mariska de Wild-Scholten. Energy payback time and carbon footprint of commercial photovoltaic systems. *Solar Energy Materials and Solar Cells*, 119:296–305, 2013.

[10] Martin A Green, Yoshihiro Hishikawa, Ewan D Dunlop, Dean H Levi, Jochen Hohl-Ebinger, and Anita WY Ho-Baillie. Solar cell efficiency tables (version 51). *Progress in photovoltaics: research and applications*, 26(1):3–12, 2018.

[11] Sven Rühle. Tabulated values of the Shockley–Queisser limit for single junction solar cells. *Solar Energy*, 130:139–147, 2016.

[12] Simon M Sze, Yiming Li, and Kwok K Ng. *Physics of semiconductor devices*. John wiley & sons, 4$^{\text{th}}$ edition, 2021.

[13] Chih-Tang Sah, Robert N Noyce, and William Shockley. Carrier generation and recombination in pn junctions and pn junction characteristics. *Proceedings of the IRE*, 45(9):1228–1243, 1957.

[14] Re N Hall. Electron-hole recombination in germanium. *Physical review*, 87(2):387, 1952.

[15] WTRW Shockley and WT Read Jr. Statistics of the recombinations of holes and electrons. *Physical review*, 87(5):835, 1952.

[16] Drew E Swanson, Jason M Kephart, Pavel S Kobyakov, Kevin Walters, Kevan C Cameron, Kurt L Barth, Walajabad S Sampath, Jennifer Drayton, and James R Sites. Single vacuum chamber with multiple close space sublimation sources to fabricate CdTe solar cells. *Journal of Vacuum Science & Technology A: Vacuum, Surfaces, and Films*, 34(2):021202, 2016.

[17] Amit H Munshi, Jason M Kephart, Ali Abbas, Adam Danielson, Guillaume Gelinas, Jean-Nicolas Beaudry, Kurt L Barth, John M Walls, and Walajabad S Sampath. Effect of $CdCl_2$ passivation treatment on microstructure and performance of CdSeTe/CdTe thin-film photovoltaic devices. *Solar Energy Materials and Solar Cells*, 186:259–265, 2018.

[18] Chen Li, Yelong Wu, Jonathan Poplawsky, Timothy J Pennycook, Naba Paudel, Wanjian Yin, Sarah J Haigh, Mark P Oxley, Andrew R Lupini, Mowafak Al-Jassim, et al. Grain boundary enhanced carrier collection in CdTe solar cells. *Physical review letters*, 112(15):156103, 2014.

[19] Akash Shah, Anthony P. Nicholson, Thomas A. M. Fiducia, Ali Abbas, Ramesh Pandey, Junliang Liu, Chris Grovenor, John M. Walls, Walajabad S. Sampath, and Amit H. Munshi. Understanding the copassivation effect of Cl and Se for CdTe grain boundaries. *ACS Applied Materials & Interfaces*, 13(29):35086–35096, 2021.

[20] Ramesh Pandey, Akash Shah, Amit H Munshi, Tushar Shimpi, Pascal Jundt, Jinglong Guo, Robert Klie, Walajabad S Sampath, and James R. Sites. Mitigation of J-V distortion in CdTe solar cells by Ga-doping of MgZnO emitter. *Solar Energy Materials and Solar Cells*, 232:111324, 2021.

[21] Andrew Moore, Tao Song, and James Sites. Improved CdTe solar-cell performance with an evaporated Te layer before the back contact. *MRS Advances*, 2(53):3195–3201, 2017.

[22] Tao Song, Andrew Moore, and James R Sites. Te layer to reduce the CdTe back-contact barrier. *IEEE Journal of Photovoltaics*, 8(1):293–298, 2017.

[23] Steven S Hegedus and William N Shafarman. Thin-film solar cells: device measurements and analysis. *Progress in Photovoltaics: Research and Applications*, 12(2-3):155–176, 2004.

[24] Darius Kuciauskas, Joel N Duenow, Ana Kanevce, Jian V Li, Matthew R Young, Pat Dippo, and Dean H Levi. Optical-fiber-based, time-resolved photoluminescence spectrometer for thin-film absorber characterization and analysis of TRPL data for CdS/CdTe interface. In *2012 38th IEEE Photovoltaic Specialists Conference*, pages 001721–001726. IEEE, 2012.

[25] Marc Burgelman, Johan Verschraegen, Stefaan Degrave, and Peter Nollet. Modeling thin-film PV devices. *Progress in Photovoltaics: Research and Applications*, 12(2-3):143–153, 2004.

[26] Ramesh Pandey, Tushar Shimpi, Amit Munshi, and James R Sites. Impact of carrier concentration and carrier lifetime on MgZnO/CdSeTe/CdTe solar cells. *IEEE Journal of Photovoltaics*, 10(6):1918–1925, 2020.

[27] Richard L Anderson. Experiments on Ge-GaAs heterojunctions. In *Electronic Structure of Semiconductor Heterojunctions*, pages 35–48. Springer, 1988.

[28] WR Frensley and H Kroemer. Theory of the energy-band lineup at an abrupt semiconductor heterojunction. *Physical Review B*, 16(6):2642, 1977.

[29] Walter Schottky. Zur halbleitertheorie der sperrschicht-und spitzengleichrichter. *Zeitschrift für Physik*, 113(5):367–414, 1939.

[30] SH Demtsu and JR Sites. Effect of back-contact barrier on thin-film CdTe solar cells. *Thin Solid Films*, 510(1-2):320–324, 2006.

[31] CR Crowell and SM Sze. Current transport in metal-semiconductor barriers. *Solid-state electronics*, 9(11-12):1035–1048, 1966.

[32] CY Chang and SM Sze. Carrier transport across metal-semiconductor barriers. *Solid-State Electronics*, 13(6):727–740, 1970.

[33] Ellis T Roe, Kira E Egelhofer, and Mark C Lonergan. Exchange current density model for the contact-determined current-voltage behavior of solar cells. *Journal of Applied Physics*, 125(22):225302, 2019.

[34] Alex Niemegeers and Marc Burgelman. Effects of the Au/CdTe back contact on IV and CV characteristics of Au/CdTe/CdS/TCO solar cells. *Journal of applied physics*, 81(6):2881–2886, 1997.

[35] Jun Pan, Markus Gloeckler, and James R Sites. Hole current impedance and electron current enhancement by back-contact barriers in CdTe thin film solar cells. *Journal of applied physics*, 100(12):124505, 2006.

[36] DL Bätzner, A Romeo, H Zogg, R Wendt, and AN Tiwari. Development of efficient and stable back contacts onCdTe/CdS solar cells. *Thin Solid Films*, 387(1-2):151–154, 2001.

[37] Jun Liang, Hui Bi, Dongyun Wan, and Fuqiang Huang. Novel Cu nanowires/graphene as the back contact for CdTe solar cells. *Advanced Functional Materials*, 22(6):1267–1271, 2012.

[38] TM Barnes, X Wu, J Zhou, A Duda, J Van de Lagemaat, TJ Coutts, CL Weeks, DA Britz, and P Glatkowski. Single-wall carbon nanotube networks as a transparent back contact in CdTe solar cells. *Applied Physics Letters*, 90(24):243503, 2007.

[39] CR Corwine, AO Pudov, M Gloeckler, SH Demtsu, and JR Sites. Copper inclusion and migration from the back contact in CdTe solar cells. *Solar Energy Materials and Solar Cells*, 82(4):481–489, 2004.

[40] Jae Ho Yun, Ki Hwan Kim, Doo Youl Lee, and Byung Tae Ahn. Back contact formation using Cu_2Te as a Cu-doping source and as an electrode in CdTe solar cells. *Solar Energy Materials and Solar Cells*, 75(1-2):203–210, 2003.

[41] Lukas Kranz, Christina Gretener, Julian Perrenoud, Rafael Schmitt, Fabian Pianezzi, Fabio La Mattina, Patrick Blösch, Erik Cheah, Adrian Chirilă, Carolin M Fella, et al. Doping of polycrystalline CdTe for high-efficiency solar cells on flexible metal foil. *Nature communications*, 4(1):1–7, 2013.

[42] Martin A Green. The Passivated Emitter and Rear Cell (PERC): From conception to mass production. *Solar Energy Materials and Solar Cells*, 143:190–197, 2015.

[43] Gijs Dingemans and WMM Kessels. Status and prospects of Al_2O3-based surface passivation schemes for silicon solar cells. *Journal of Vacuum Science & Technology A: Vacuum, Surfaces, and Films*, 30(4):040802, 2012.

[44] Frank Feldmann, Martin Bivour, Christian Reichel, Martin Hermle, and Stefan W Glunz. Passivated rear contacts for high-efficiency n-type Si solar cells providing high interface passivation quality and excellent transport characteristics. *Solar energy materials and solar cells*, 120:270–274, 2014.

[45] Frank Feldmann, Martin Bivour, Christian Reichel, Heiko Steinkemper, Martin Hermle, and Stefan W Glunz. Tunnel oxide passivated contacts as an alternative to partial rear contacts. *Solar Energy Materials and Solar Cells*, 131:46–50, 2014.

[46] Ramesh Pandey, Amit Munshi, Tushar Shimpi, Akash Shah, Alexandra Bothwell, Darius Kuciauskas, and James R Sites. Cdte-based solar cells with variations in Mg concentration in the MgZnO emitter. *Solar RRL*, page 2100126, 2021.

[47] https://www.nrel.gov/pv/cell-efficiency.html. (Accessed on May 01, 2021).

[48] Naba R Paudel and Yanfa Yan. Enhancing the photo-currents of CdTe thin-film solar cells in both short and long wavelength regions. *Applied Physics Letters*, 105(18):183510, 2014.

[49] Drew E Swanson, James R Sites, and Walajabad S Sampath. Co-sublimation of $CdSe_xTe_{1-x}$ layers for CdTe solar cells. *Solar Energy Materials and Solar Cells*, 159:389–394, 2017.

[50] Amit H Munshi, Jason Kephart, Ali Abbas, John Raguse, Jean-Nicolas Beaudry, Kurt Barth, James Sites, John Walls, and Walajabad Sampath. Polycrystalline CdSeTe/CdTe absorber cells with 28 mA/cm^2 short-circuit current. *IEEE Journal of Photovoltaics*, 8(1):310–314, 2017.

[51] Martina Lingg, Annina Spescha, Stefan G Haass, Romain Carron, Stephan Buecheler, and Ayodhya N Tiwari. Structural and electronic properties of $CdTe_{1-x}Se_x$ films and their application in solar cells. *Science and technology of advanced materials*, 19(1):683–692, 2018.

[52] Tursun Ablekim, Joel N Duenow, Xin Zheng, Helio Moutinho, John Moseley, Craig L Perkins, Steven W Johnston, Patrick O'Keefe, Eric Colegrove, David S Albin, et al. Thin film solar cells with 19% efficiency by thermal evaporation of CdSe and CdTe. *ACS Energy Letters*, 5(3):892–896, 2020.

[53] Jonathan D Poplawsky, Wei Guo, Naba Paudel, Amy Ng, Karren More, Donovan Leonard, and Yanfa Yan. Structural and compositional dependence of the $CdTe_xSe_{1-x}$ alloy layer photoactivity in CdTe-based solar cells. *Nature communications*, 7(1):1–10, 2016.

[54] Thomas AM Fiducia, Budhika G Mendis, Kexue Li, Chris RM Grovenor, Amit H Munshi, Kurt Barth, Walajabad S Sampath, Lewis D Wright, Ali Abbas, Jake W Bowers, et al. Understanding the role of selenium in defect passivation for highly efficient selenium-alloyed cadmium telluride solar cells. *Nature Energy*, 4(6):504–511, 2019.

[55] Mahisha Amarasinghe, Eric Colegrove, John Moseley, Helio Moutinho, David Albin, Joel Duenow, Soren Jensen, Jason Kephart, Walajabad Sampath, Siva Sivananthan, et al. Obtaining large columnar CdTe grains and long lifetime on nanocrystalline CdSe, MgZnO, or CdS layers. *Advanced Energy Materials*, 8(11):1702666, 2018.

[56] Akash Shah, Amit H Munshi, Anthony P Nicholson, Aanand Thiyagarajan, Umberto M Pozzoni, and Walajabad S Sampath. Atomistic modeling of energy band alignment in CdSeTe surfaces. *Applied Surface Science*, 544:148762, 2021.

[57] Darius Kuciauskas, David Albin, John Moseley, Siming Li, Patrik Ščajev, Carey Reich, Amit H Munshi, Adam Danielson, Walajabad Sampath, and Chungho Lee. Microsecond carrier lifetimes in polycrystalline CdSeTe heterostructures and in CdSeTe thin film solar cells. In *2020 47th IEEE Photovoltaic Specialists Conference (PVSC)*, pages 0082–0084. IEEE, 2020.

[58] Darius Kuciauskas, John Moseley, Patrik Ščajev, and David Albin. Radiative efficiency and charge-carrier lifetimes and diffusion length in polycrystalline CdSeTe heterostructures. *physica status solidi (RRL)–Rapid Research Letters*, 14(3):1900606, 2020.

[59] Tursun Ablekim, Joel N Duenow, Craig L Perkins, John Moseley, Xin Zheng, Thomas Bidaud, Berengere Frouin, Stephane Collin, Matthew O Reese, Mahisha Amarasinghe, et al. Exceeding 200-ns lifetimes in polycrystalline CdTe solar cells. *Solar RRL*, 2021.

[60] Darius Kuciauskas, John Moseley, and Chungho Lee. Identification of recombination losses in CdSe/CdTe solar cells from spectroscopic and microscopic time-resolved photoluminescence. *Solar RRL*, 5(4):2000775, 2021.

[61] Takashi Minemoto, Akira Okamoto, and Hideyuki Takakura. Sputtered ZnO-based buffer layer for band offset control in Cu (In, Ga) Se_2 solar cells. *Thin Solid Films*, 519(21):7568–7571, 2011.

[62] IL Eisgruber, JE Granata, JR Sites, J Hou, and J Kessler. Blue-photon modification of nonstandard diode barrier in $CuInSe_2$ solar cells. *Solar Energy Materials and Solar Cells*, 53(3-4):367–377, 1998.

[63] AO Pudov, JR Sites, MA Contreras, T Nakada, and H-W Schock. CIGS J–V distortion in the absence of blue photons. *Thin Solid Films*, 480:273–278, 2005.

[64] JM Kephart, JW McCamy, Z Ma, A Ganjoo, FM Alamgir, and WS Sampath. Band alignment of front contact layers for high-efficiency CdTe solar cells. *Solar Energy Materials and Solar Cells*, 157:266–275, 2016.

[65] Tursun Ablekim, Craig Perkins, Xin Zheng, Carey Reich, Drew Swanson, Eric Colegrove, Joel N Duenow, David Albin, Sanjini Nanayakkara, Matthew O Reese, et al. Tailoring MgZnO/CdSeTe interfaces for photovoltaics. *IEEE Journal of Photovoltaics*, 9(3):888–892, 2019.

[66] Deng-Bing Li, Zhaoning Song, Rasha A Awni, Sandip S Bista, Niraj Shrestha, Corey R Grice, Lei Chen, Geethika K Liyanage, Mohammed A Razooqi, Adam B Phillips, et al. Eliminating S-kink to maximize the performance of MgZnO/CdTe solar cells. *ACS Applied Energy Materials*, 2(4):2896–2903, 2019.

[67] Yegor Samoilenko, Gavin Yeung, Amit H Munshi, Ali Abbas, Carey L Reich, Michael Walker, Matthew O Reese, Andriy Zakutayev, J Michael Walls, Walajabad S Sampath, et al. Stable magnesium zinc oxide by reactive co-sputtering for CdTe-based solar cells. *Solar Energy Materials and Solar Cells*, 210:110521, 2020.

[68] J Tauc, Radu Grigorovici, and Anina Vancu. Optical properties and electronic structure of amorphous germanium. *physica status solidi (b)*, 15(2):627–637, 1966.

[69] Takashi Minemoto, Takayuki Negami, Shiro Nishiwaki, Hideyuki Takakura, and Yoshihiro Hamakawa. Preparation of $Zn_{1-x}Mg_xO$ films by radio frequency magnetron sputtering. *Thin solid films*, 372(1-2):173–176, 2000.

[70] Vinodkumar Etacheri, Roshith Roshan, and Vishwanathan Kumar. Mg-doped ZnO nanoparticles for efficient sunlight driven photocatalysis. *ACS applied materials & interfaces*, 4(5):2717–2725, 2012.

[71] Dinesh Thapa, Jesse Huso, Jeffrey Lapp, Negar Rajabi, John L Morrison, Matthew D McCluskey, and Leah Bergman. Thermal stability of ultra-wide-bandgap MgZnO alloys with wurtzite structure. *Journal of Materials Science: Materials in Electronics*, 29(19):16782–16790, 2018.

[72] S Choopun, RD Vispute, W Yang, RP Sharma, T Venkatesan, and vH Shen. Realization of band gap above 5.0 eV in metastable cubic-phase $Mg_xZn_{1-x}O$ alloy films. *Applied Physics Letters*, 80(9):1529–1531, 2002.

[73] Z Vashaei, T Minegishi, H Suzuki, T Hanada, MW Cho, T Yao, and A Setiawan. Structural variation of cubic and hexagonal $Mg_xZn_{1-x}O$ layers grown on MgO (111)/ c-sapphire. *Journal of applied physics*, 98(5):054911, 2005.

[74] A Ohtomo, M Kawasaki, T Koida, K Masubuchi, H Koinuma, Y Sakurai, Yasuda Yoshida, T Yasuda, and Y Segawa. $Mg_xZn_{1-x}O$ as a II–VI widegap semiconductor alloy. *Applied Physics Letters*, 72(19):2466–2468, 1998.

[75] AK Sharma, J Narayan, JF Muth, CW Teng, C Jin, A Kvit, R Mi Kolbas, and OW Holland. Optical and structural properties of epitaxial $Mg_xZn_{1-x}O$ alloys. *Applied Physics Letters*, 75(21):3327–3329, 1999.

[76] Takashi Minemoto, Takuya Matsui, Hideyuki Takakura, Yoshihiro Hamakawa, Takayuki Negami, Yasuhiro Hashimoto, Takeshi Uenoyama, and Masatoshi Kitagawa. Theoretical analysis of the effect of conduction band offset of window/CIS layers on performance of CIS solar cells using device simulation. *Solar Energy Materials and Solar Cells*, 67(1-4):83–88, 2001.

[77] M Gloeckler and JR Sites. Efficiency limitations for wide-band-gap chalcopyrite solar cells. *Thin Solid Films*, 480:241–245, 2005.

[78] Takashi Minemoto, Yasuhiro Hashimoto, Takuya Satoh, Takayuki Negami, Hideyuki Takakura, and Yoshihiro Hamakawa. $Cu(In,Ga)Se_2$ solar cells with controlled conduction band offset of window/$Cu(In,Ga)Se_2$ layers. *Journal of applied physics*, 89(12):8327–8330, 2001.

[79] Takashi Minemoto, Yasuhiro Hashimoto, Wahid Shams-Kolahi, Takuya Satoh, Takayuki Negami, Hideyuki Takakura, and Yoshihiro Hamakawa. Control of conduction band offset in wide-gap $Cu(In,Ga)Se_2$ solar cells. *Solar energy materials and solar cells*, 75(1-2):121–126, 2003.

[80] Tao Song, Ana Kanevce, and James R Sites. Emitter/absorber interface of CdTe solar cells. *Journal of Applied Physics*, 119(23):233104, 2016.

[81] Tursun Ablekim, Eric Colegrove, and Wyatt K Metzger. Interface engineering for 25% CdTe solar cells. *ACS Applied Energy Materials*, 1(10):5135–5139, 2018.

[82] Ana Kanevce, Matthew O Reese, TM Barnes, SA Jensen, and WK Metzger. The roles of carrier concentration and interface, bulk, and grain-boundary recombination for 25% efficient cdte solar cells. *Journal of Applied Physics*, 121(21):214506, 2017.

[83] A Kanevce, M Gloeckler, AO Pudov, and JR Sites. Conduction-band-offset rule governing JV distortion in CdS/CIGS solar cells. *MRS Online Proceedings Library (OPL)*, 865, 2005.

[84] Haitao Yin, Junli Chen, Yin Wang, Jian Wang, and Hong Guo. Composition dependent band offsets of ZnO and its ternary alloys. *Scientific reports*, 7(1):1–7, 2017.

[85] Chao Ding, Yaohong Zhang, Feng Liu, Yukiko Kitabatake, Shuzi Hayase, Taro Toyoda, Ruixiang Wang, Kenji Yoshino, Takashi Minemoto, and Qing Shen. Understanding charge transfer and recombination by interface engineering for improving the efficiency of PbSs quantum dot solar cells. *Nanoscale Horizons*, 3(4):417–429, 2018.

[86] Zhigang Yin, Qingdong Zheng, Shan-Ci Chen, Dongdong Cai, Lingyu Zhou, and Jian Zhang. Bandgap tunable $Zn_{1-x}Mg_xO$ thin films as highly transparent cathode buffer layers for high-performance inverted polymer solar cells. *Advanced Energy Materials*, 4(7):1301404, 2014.

[87] HH Zhang, XH Pan, B Lu, JY Huang, P Ding, W Chen, HP He, JG Lu, SS Chen, and ZZ Ye. Mg composition dependent band offsets of $Zn_{1-x}Mg_xO$/ZnO heterojunctions. *Physical Chemistry Chemical Physics*, 15(27):11231–11235, 2013.

[88] EA Kraut, RW Grant, JR Waldrop, and SP Kowalczyk. Precise determination of the valence-band edge in X-ray photoemission spectra: Application to measurement of semiconductor interface potentials. *Physical Review Letters*, 44(24):1620, 1980.

[89] Douglas A Duncan, Rueben Mendelsberg, Michelle Mezher, Kimberly Horsley, Samantha G Rosenberg, Monika Blum, Gang Xiong, Lothar Weinhardt, Markus Gloeckler, and Clemens Heske. A new look at the electronic structure of transparent conductive oxides— A case study of the interface between zinc magnesium oxide and cadmium telluride. *Advanced Materials Interfaces*, 3(22):1600418, 2016.

[90] Markus Gloeckler, Caroline R Jenkins, and James R Sites. Explanation of light/dark superposition failure in CIGS solar cells. *MRS Online Proceedings Library (OPL)*, 763, 2003.

[91] Marc Köntges, Rolf Reineke-Koch, Peter Nollet, Jutta Beier, Raymund Schäffler, and Jürgen Parisi. Light induced changes in the electrical behavior of CdTe and Cu(In,Ga)Se_2 solar cells. *Thin Solid Films*, 403:280–286, 2002.

[92] Woo-Jung Lee, Hye-Jung Yu, Jae-Hyung Wi, Dae-Hyung Cho, Won Seok Han, Jisu Yoo, Yeonjin Yi, Jung-Hoon Song, and Yong-Duck Chung. Behavior of photocarriers in the light-induced metastable state in the p-n heterojunction of a Cu(In,Ga)Se_2 solar cell with CBD-ZnS buffer layer. *ACS applied materials & interfaces*, 8(34):22151–22158, 2016.

[93] Anderson Janotti and Chris G Van de Walle. Native point defects in ZnO. *Physical Review B*, 76(16):165202, 2007.

[94] Matthew D McCluskey and SJ Jokela. Defects in ZnO. *Journal of Applied Physics*, 106(7):10, 2009.

[95] SM Evans, NC Giles, LE Halliburton, and LA Kappers. Further characterization of oxygen vacancies and zinc vacancies in electron-irradiated ZnO. *Journal of Applied Physics*, 103(4):043710, 2008.

[96] Jason M Kephart and WS Sampath. Gallium-doped magnesium zinc oxide (GMZO) transparent conducting oxide layers for CdTe thin-film photovoltaics. In *2015 IEEE 42nd Photovoltaic Specialist Conference (PVSC)*, pages 1–4. IEEE, 2015.

[97] Pravakar P Rajbhandari, Andre Bikowski, John D Perkins, Tara P Dhakal, and Andriy Zakutayev. Combinatorial sputtering of Ga-doped (Zn, Mg) O for contact applications in solar cells. *Solar Energy Materials and Solar Cells*, 159:219–226, 2017.

[98] Brian Good, Tursun Ablekim, Imran S Khan, Matthew O Reese, Andriy Zakutayev, and Wyatt K Metzger. Tailoring SnO_2,(Mg, Zn) O, and Ga:(Mg, Zn) O electro-optical properties and stability for solar cells. *Journal of Physics D: Applied Physics*, 54(3):034002, 2020.

[99] Gavin Yeung and Colin A Wolden. Controlling conduction band alignment and carrier concentration in gallium-doped magnesium zinc oxide by reactive cosputtering. *Journal of Vacuum Science & Technology A: Vacuum, Surfaces, and Films*, 39(2):022802, 2021.

[100] James Sites and Jun Pan. Strategies to increase CdTe solar-cell voltage. *Thin Solid Films*, 515(15):6099–6102, 2007.

[101] WK Metzger and M Gloeckler. The impact of charged grain boundaries on thin-film solar cells and characterization. *Journal of Applied Physics*, 98(6):063701, 2005.

[102] Wyatt K Metzger, S Grover, D Lu, E Colegrove, John Moseley, CL Perkins, X Li, R Mallick, W Zhang, R Malik, et al. Exceeding 20% efficiency with in situ group V doping in polycrystalline CdTe solar cells. *Nature Energy*, 4(10):837–845, 2019.

[103] Tursun Ablekim, Santosh K Swain, Wan-Jian Yin, Katherine Zaunbrecher, James Burst, Teresa M Barnes, Darius Kuciauskas, Su-Huai Wei, and Kelvin G Lynn. Self-compensation in arsenic doping of CdTe. *Scientific reports*, 7(1):1–9, 2017.

[104] Brian E McCandless, Wayne A Buchanan, Christopher P Thompson, Gowri Sriramagiri, Robert J Lovelett, Joel Duenow, David Albin, Søren Jensen, Eric Colegrove, John Moseley, et al. Overcoming carrier concentration limits in polycrystalline CdTe thin films with in situ doping. *Scientific reports*, 8(1):1–13, 2018.

[105] Akira Nagaoka, Darius Kuciauskas, Jedidiah McCoy, and Michael A Scarpulla. High p-type doping, mobility, and photocarrier lifetime in arsenic-doped CdTe single crystals. *Applied Physics Letters*, 112(19):192101, 2018.

[106] CS Ferekides, V Viswanathan, and DL Morel. RF sputtered back contacts for CdTe/CdS thin film solar cells. In *Conference Record of the Twenty Sixth IEEE Photovoltaic Specialists Conference-1997*, pages 423–426. IEEE, 1997.

[107] Elisa Artegiani, Daniele Menossi, Huw Shiel, Vin Dhanak, Jonathan D Major, Andrea Gasparotto, Kai Sun, and Alessandro Romeo. Analysis of a novel $CuCl_2$ back contact process for improved stability in CdTe solar cells. *Progress in Photovoltaics: Research and Applications*, 27(8):706–715, 2019.

[108] SH Demtsu, DS Albin, JR Sites, WK Metzger, and A Duda. Cu-related recombination in CdS/CdTe solar cells. *Thin Solid Films*, 516(8):2251–2254, 2008.

[109] 1J Perrenoud, L Kranz, C Gretener, F Pianezzi, S Nishiwaki, S Buecheler, and AN Tiwari. A comprehensive picture of Cu doping in CdTe solar cells. *Journal of Applied Physics*, 114(17):174505, 2013.

[110] Elisa Artegiani, Jonathan D Major, Huw Shiel, Vin Dhanak, Claudio Ferrari, and Alessandro Romeo. How the amount of copper influences the formation and stability of defects in CdTe solar cells. *Solar Energy Materials and Solar Cells*, 204:110228, 2020.

[111] Dmitry Krasikov, Da Guo, Samuel Demtsu, and Igor Sankin. Comparative study of As and Cu doping stability in CdSeTe absorbers. *Solar Energy Materials and Solar Cells*, 224:111012, 2021.

[112] https://www.firstsolar.com/en/modules/series-6-cure. (Acessed on May 01, 2021).

[113] S Uličná, PJM Isherwood, Piotr M Kaminski, JM Walls, Jiaojiao Li, and Colin A Wolden. Development of ZnTe as a back contact material for thin film cadmium telluride solar cells. *Vacuum*, 139:159–163, 2017.

[114] TA Gessert, AR Mason, P Sheldon, AB Swartzlander, D Niles, and TJ Coutts. Development of Cu-doped ZnTe as a back-contact interface layer for thin-film CdS/CdTe solar cells. *Journal of Vacuum Science & Technology A: Vacuum, Surfaces, and Films*, 14(3):806–812, 1996.

[115] Jian V Li, Joel N Duenow, Darius Kuciauskas, Ana Kanevce, Ramesh G Dhere, Matthew R Young, and Dean H Levi. Electrical characterization of Cu composition effects in CdS/CdTe thin-film solar cells with a ZnTe:Cu back contact. In *2012 IEEE 38th Photovoltaic Specialists Conference (PVSC) Part 2*, pages 1–5. IEEE, 2012.

[116] Fadhil K Alfadhili, Adam B Phillips, Manoj K Jamarkattel, Austin J Snyder, Jacob M Gibbs, Geethika K Liyanage, and Michael J Heben. Potential of CdZnTe thin film back buffer layer for CdTe solar cells. In *2019 IEEE 46th Photovoltaic Specialists Conference (PVSC)*, pages 0140–0143. IEEE, 2019.

[117] Alexandra M Bothwell, Jennifer A Drayton, and James R Sites. Efficiency advances in thin CdSeTe/CdTe solar cells with CdMgTe at the back. In *2020 47th IEEE Photovoltaic Specialists Conference (PVSC)*, pages 1248–1253. IEEE, 2020.

[118] Suneth C Watthage, Adam B Phillips, Geethika K Liyanage, Zhaoning Song, Jacob M Gibbs, Fadhil K Alfadhili, Rabee B Alkhayat, Ramez H Ahangharnejhad, Zahrah S Almutawah, Khagendra P Bhandari, et al. Selective Cd removal from CdTe for high-efficiency Te back-contact formation. *IEEE Journal of Photovoltaics*, 8(4):1125–1131, 2018.

[119] Matthew O Reese, Craig L Perkins, James M Burst, Stuart Farrell, Teresa M Barnes, Steve W Johnston, Darius Kuciauskas, Timothy A Gessert, and Wyatt K Metzger. Intrinsic surface passivation of CdTe. *Journal of Applied Physics*, 118(15):155305, 2015.

[120] Geethika K Liyanage, Adam B Phillips, Fadhil K Alfadhili, Randy J Ellingson, and Michael J Heben. The role of back buffer layers and absorber properties for $> 25\%$ efficient CdTe solar cells. *ACS Applied Energy Materials*, 2(8):5419–5426, 2019.

[121] Joel N Duenow and Wyatt K Metzger. Back-surface recombination, electron reflectors, and paths to 28% efficiency for thin-film photovoltaics: A CdTe case study. *Journal of Applied Physics*, 125(5):053101, 2019.

[122] Ido Hadar, Xiaobing Hu, Zhong-Zhen Luo, Vinayak P Dravid, and Mercouri G Kanatzidis. Nonlinear band gap tunability in selenium-Tellurium alloys and its utilization in solar cells. *ACS Energy Letters*, 4(9):2137–2143, 2019.

[123] Anthony P Nicholson, Umberto Martinez, Akash Shah, Aanand Thiyagarajan, and Walajabad S Sampath. Atomistic modeling of energy band alignment in CdTe (100) and CdTe (111) surfaces. *Applied Surface Science*, 528:146832, 2020.

[124] James Bullock, Andres Cuevas, Thomas Allen, and Corsin Battaglia. Molybdenum oxide MoO_x: A versatile hole contact for silicon solar cells. *Applied Physics Letters*, 105(23):232109, 2014.

[125] Kamala Khanal Subedi, Adam B Phillips, Niraj Shrestha, Fadhil K Alfadhili, Anna Osella, Indra Subedi, Rasha A Awni, Ebin Bastola, Zhaoning Song, Deng-Bing Li, et al. Enabling bifacial thin film devices by developing a back surface field using Cu_xAlO_y. *Nano Energy*, 83:105827, 2021.

[126] Yong Jung Kwon, Sun-Woo Choi, Sung Yong Kang, Myung Sik Choi, Jae Hoon Bang, Sang Sub Kim, and Hyoun Woo Kim. Enhancement of the benzene-sensing performance of Si nanowires through the incorporation of TeO_2 heterointerfaces and Pd-sensitization. *Sensors and Actuators B: Chemical*, 244:1085–1097, 2017.

[127] Myung Sik Choi, Jae Hoon Bang, Ali Mirzaei, Han Gil Na, Changhyun Jin, Wansik Oum, Sang Sub Kim, and Hyoun Woo Kim. Exploration of the use of p-TeO_2-branch/n-SnO_2 core nanowires nanocomposites for gas sensing. *Applied Surface Science*, 484:1102–1110, 2019.

[128] Jason M Kephart, Anna Kindvall, Desiree Williams, Darius Kuciauskas, Pat Dippo, Amit Munshi, and WS Sampath. Sputter-deposited oxides for interface passivation of CdTe photovoltaics. *IEEE Journal of Photovoltaics*, 8(2):587–593, 2018.

[129] Ramesh Pandey, Akash Shah, Amit Munshi, Pascal Jundt, Tushar Shimpi, Darius Kuciauskas, and James Sites. Transparent MgO for back-contact passivation of CdTe-based solar cells. In *2021 IEEE 48th Photovoltaic Specialists Conference (PVSC)*, pages 1163–1165, 2021.

[130] Di Xiao, Xun Li, Dongming Wang, Qiang Li, Kai Shen, and Deliang Wang. CdTe thin film solar cell with NiO as a back contact buffer layer. *Solar Energy Materials and Solar Cells*, 169:61–67, 2017.

[131] Pietro P Altermatt and Keith R McIntosh. A roadmap for PERC cell efficiency towards 22%, focused on technology-related constraints. *Energy Procedia*, 55:17–21, 2014.

LIST OF PUBLICATIONS

- **Ramesh Pandey,** Tushar Shimpi, Amit Munshi, and James R. Sites. "Impact of Carrier Concentration and Carrier Lifetime on MgZnO/CdSeTe/CdTe Solar Cells." IEEE Journal of Photovoltaics 10, no. 6 (2020): 1918-1925.

- **Ramesh Pandey,** Amit Munshi, Tushar Shimpi, Akash Shah, Alexandra Bothwell, Darius Kuciauskas, and James R. Sites. "CdTe-Based Solar Cells with Variations in Mg Concentration in the MgZnO Emitter." Solar RRL (2021): 2100126.

- **Ramesh Pandey,** Akash Shah, Amit H Munshi, Tushar Shimpi, Pascal Jundt, Jinglong Guo, Robert Klie, Walajabad S Sampath, and James R. Sites. "Mitigation of J-V distortion in CdTe solar cells by Ga-doping of MgZnO emitter." Solar Energy Materials and Solar Cells, 232:111324, 2021.

- Akash Shah, **Ramesh Pandey,** Anthony Nicholson, Zach Lustig, Ali Abbas, Adam Danielson, James Sites, John Walls, Amit Munshi, and Walajabad Sampath. "Understanding the Role of CdTe in Polycrystalline $CdSe_xTe_{1-x}$/CdTe Graded Bilayer Photovoltaic Device." Solar RRL, 2021. (Accepted for Publication, In press).

- Akash Shah, Anthony P. Nicholson, Thomas A. M. Fiducia, Ali Abbas, **Ramesh Pandey,** Junliang Liu, Chris Grovenor, John M. Walls, Walajabad S. Sampath, and Amit H. Munshi. "Understanding the Copassivation Effect of Cl and Se for CdTe Grain Boundaries." ACS Applied Materials & Interfaces 2021 13 (29), 35086-35096

- Tyler, Kevin D., Madhan K. Arulanandam, **Ramesh Pandey,** Niranjana Mohan Kumar, Jennifer Drayton, James R. Sites, and Richard R. King. "Silicon degradation in monolithic II–VI/Si tandem solar cells." IEEE Journal of Photovoltaics 10, no. 2 (2020): 690-695.

- Schwartz, Dakota, Rubaiya Murshed, Harry Larson, Benedikt Usprung, Sina Soltanmohamad, **Ramesh Pandey,** Edward S. Barnard, Angus Rockett, Thomas Hartmann, Ivano E Castelli, Shubhra Bansal. "Air Stable, High-Efficiency, Pt-Based Halide Perovskite Solar Cells with Long Carrier Lifetimes." physica status solidi (RRL)–Rapid Research Letters 14, no. 8 (2020): 2000182.

- **Ramesh Pandey,** Jennifer Drayton, Christopher Gregory, Niranjana Mohan Kumar, Kevin Tyler, Richard King, and James Sites. "Cadmium Telluride Cells on Silicon as Precursors for Two-Junction Tandem Cells." In 2020 47th IEEE Photovoltaic Specialists Conference (PVSC), pp. 1326-1329. IEEE, 2020.

- **Ramesh Pandey,** Akash Shah, Amit H Munshi, Pascal Jundt, Darius Kuciauskas, and James R. Sites. "Transparent MgO for back-contact passivation of CdTe-based solar cells." In 48th IEEE Photovoltaic Specialists Conference (PVSC), pp. 1163-1165. IEEE, 2021.

- Amit H. Munshi, Carey L. Reich, Adam H. Danielson, **Ramesh Pandey,** Darius Kuciauskas, Siming Li, Akash Shah, Santosh Swain, Tushar M. Shimpi, Tawfeeq K. Al-Hamdi, Kelvin G. Lynn, Walajabad S. Sampath. "Arsenic Doping of Polycrystalline CdSeTe Devices for Microsecond Life-times with High Carrier Concentrations." In 2020 47th IEEE Photovoltaic Specialists Conference (PVSC), pp. 1824-1828. IEEE, 2020.

- Akash Shah, **Ramesh Pandey,** Anthony P. Nicholson, Tushar Shimpi, Walajabad S. Sampath, and Amit H. Munshi. "First principles guided device fabrication of arsenic-doped CdTe photovoltaics." In 48th IEEE Photovoltaic Specialists Conference (PVSC), pp. 1527-1529. IEEE, 2021.

- Pascal Jundt, **Ramesh Pandey,** Amit Munshi, and James Sites. "Transparent Buffer Layer for Back Surface Passivation in CdTe Photovoltaics." In 48th IEEE Photovoltaic Specialists Conference (PVSC), pp. 1614-1618. IEEE, 2021.

- Shimpi, Tushar, Drew Swanson, Carey Reich, Jason Kephart, Anna Kindvall, **Ramesh Pandey,** Zachary Holman, Kurt Barth, and Walajabad Sampath. "Co-Sublimated Polycrystalline $Cd_{1-x}Zn_xTe$ Films for Multi-junction Solar Cells." In 2018 IEEE 7th World Conference on Photovoltaic Energy Conversion (WCPEC)(A Joint Conference of 45th IEEE PVSC, 28th PVSEC & 34th EU PVSEC), pp. 2638-2641. IEEE, 2018.

- Tyler, Kevin D., Madhan K. Arulanandam, **Ramesh Pandey,** Niranjana Mohan Kumar, Jennifer Drayton, James Sites, and Richard R. King. "Controlling Silicon Bottom Cell Lifetime Variance in II-VI/Si Tandems." In 2019 IEEE 46th Photovoltaic Specialists Conference (PVSC), pp. 2188-2191. IEEE, 2019.

- Shimpi, Tushar, Carey Reich, Adam Danielson, Amit Munshi, Anna Kindvall, **Ramesh Pandey,** Kurt Barth, and Walajabad Sampath. "Influence of Process Parameters and Absorber Thickness on Efficiency of Polycrystalline CdSeTe/CdTe Thin Film Solar Cells." In 2020 47th IEEE Photovoltaic Specialists Conference (PVSC), pp. 1933-1935. IEEE, 2020.

- Guo, Jinglong, **Ramesh Pandey,** Munshi, A., Sampath, W., and Klie, R. (2021). Electric field mapping in CdSeTe solar cell using 4D-STEM. Microscopy and Microanalysis, 27(S1), 2196-2198.

LIST OF ABBREVIATIONS

AM 1.5G	Air Mass 1.5 Solar Spectrum
CBM	Conduction Band Minima
CBO	Conduction Band Offset
$CdCl_2$	Cadmium Chloride
CdTe	Cadmium Telluride
CdMgTe	Cadmium Magnesium Telluride
CdSeTe	Cadmium Selenium Telluride
CdZnTe	Cadmium Zinc Telluride
CSU	Colorado State University
CV	Capacitance Voltage
DFT	Density Functional Theory
FF	Fill Factor
GXRD	Glancing Angle X-ray Diffraction
ITO	Indium Tin Oxide
JV	Current Voltage
MIS	Metal Insulator Semiconductor
MOS	Metal Oxide Silicon
MPP	Maximum Power Point
PERC	Passivated Emitter Rear Contact
PL	Photoluminescence
PV	Photovoltaic
QE	Quantum Efficiency
RF	Radio Frequency
SCAPS	Solar Cell Capacitance Simulation in 1-Dimension
SCR	Space Charge Region
STEM	Scanning Transmission Electron Microscope
TEM	Transmission Electron Microscope
TFSC	Thin-Film Solar Cell
TOPCon	Transparent Oxide Passivated Contact
TRPL	Time Resolved Photoluminescence
UIC	University of Chicago
VBM	Valence Band Maxima
VBO	Valence Band Offset
XEDS	Energy Dispersive X-ray Spectroscopy
ZnTe	Zinc Telluride